Endothelial-driven TGFβ signaling supports lung interstitial macrophage development from monocytes.

W. Peng[1,2], D. Vanneste[1,2], D. Bejarano[3], J. Abinet[1,2], M. Meunier[1,2], C. Radermecker[1,2], F. Perin[4], D. Cataldo[4], F. Bureau[2,5], A. Schlitzer[3], Q. Bai[1,6,*] & T. Marichal[1,2,7,*]

Affiliations:

[1] Laboratory of Immunophysiology, GIGA Institute, University of Liège; Liège, Belgium
[2] Faculty of Veterinary Medicine, University of Liège; Liège, Belgium
[3] Quantitative Systems Biology, Life and Medical Sciences (LIMES) Institute, University of Bonn, Bonn, Germany
[4] Laboratory of Tumor and Development Biology, GIGA Institute, University of Liège; Liège, Belgium
[5] Laboratory of Cellular and Molecular Immunology, GIGA Institute, University of Liège; Liège, Belgium
[6] PhyMedExp INSERM 1046, University of Montpellier, Montpellier, France
[7] Walloon Excellence in Life Sciences and Biotechnology (WELBIO) Department, WEL Research Institute; Wavre, Belgium
[*] These authors contributed equally to this work and are co–last authors.

*Corresponding authors: t.marichal@uliege.be; qiang.bai@inserm.fr

Abstract

Lung interstitial macrophages (IMs) are monocyte-derived parenchymal macrophages whose tissue-supportive functions remain unclear. Despite progress in lung IM diversity and transcriptional regulation, the signals driving their development from monocytes and their functional specification remain unknown. Here we found that lung endothelial-derived Tgfβ1 triggered a core Tgfβ receptor-dependent IM signature in mouse bone marrow-derived monocytes. *In vivo*, myeloid-specific impairment of Tgfβ receptor signaling severely disrupted monocyte-to-IM development, leading to the accumulation of perivascular immature monocytes, reduced IM numbers, and a loss of IM-intrinsic identity - a phenomenon similarly observed in the absence of endothelial-specific Tgfβ1. Mice lacking Tgfβ receptor in monocytes and IMs exhibited altered monocyte and IM niche occupancy, impaired immunoregulation, hyperinflation and fibrosis – hallmarks of aging. Our work reveals a Tgfβ signaling-dependent endothelial – IM axis that shapes IM development and sustains lung integrity, providing foundations for IM-targeted interventions in aging and chronic inflammation.

One-Sentence Summary

Endothelial Tgfβ1 shapes the development and functional identity of lung interstitial macrophages.

Introduction

In the lung, resident tissue macrophages (RTM) represent the major immune compartment at steady-state and are thought to exert important tissue-supportive, homeostatic and immune functions. Depending on their localization, two main RTM populations exist, with alveolar macrophages (AMs) residing in the alveolar lumen while interstitial macrophage (IMs) populating the lung parenchyma (*1–3*). AMs have been extensively studied and are known to be long-lived, self-maintaining RTM whose development and maintenance require type 2 alveolar epithelial cell (AT2)-derived granulocyte monocyte colony-stimulating factor (GM-CSF, also called Csf2) and AM-intrinsic transforming growth factor β1 (Tgfβ1). Such microenvironmental signals trigger sustained expression of peroxisome proliferator-activated receptor (PPAR)-γ and imprint a niche-specific functional specification important for host defense and surfactant homeostasis (*4–7*).

Conversely, IMs are less numerous, less accessible and more enigmatic cells (*2*, *8*). Our understanding of IM development and diversity has benefited from the analysis of their transcriptomic profile at the single cell level and the development of transgenic tools allowing their specific depletion (*9–14*). While up to 10 different IM subsets have been recently proposed (*12*), a consensus seems to have emerged that IMs can be primarily categorized into two main subsets, namely CD206$^+$ IMs and CD206$^-$ IMs, which occupy distinct niches (*9*, *10*, *12*, *14*). Parabiosis, bone marrow (BM) chimeras and fate-mapping studies have shown that both IM subsets are slowly replenished by classical monocytes in adult mice (*9–11*, *15*). IM development from monocytes requires the activity of the transcription factor MafB and relies on Csf1 receptor signaling when the IM niche is in need of replenishment (*11*). Moreover, mature IMs share a core signature characterized by elevated expression of MafB, the fractalkine receptor Cx3cr1, the transmembrane protein 119 (Tmem119) and the complement component 1q (C1q) (*10–12*). According to the macrophage niche model, these findings are consistent with the idea that as-yet-unknown signals released from the lung microenvironment are able to imprint a core developmental program and identity of IMs that precedes their subsequent specification into distinct subsets (*9*, *10*, *12*, *13*, *16*).

Functionally, IMs have been attributed distinct roles upon exposure to allergens (*12*, *15*, *17–19*), bleomycin (*9*), influenza virus (*14*) or bacteria (*12*) and are thought to exert immunoregulatory functions in the context of allergic asthma (*15*, *17–19*), to dampen inflammatory responses (*9*, *12*, *16*) and to organize tertiary lymphoid tissues (*12*). However, in these non-homeostatic contexts, monocytes can also be recruited to the lung and contribute to a pool of recruited macrophages that often overlap phenotypically with IMs (*1*, *3*, *20*). Such convoluted landscape can complicate conclusions regarding the precise contributions of resident IMs vs. recruited macrophages in various lung disorders. Hence, the potential tissue-supportive and homeostatic functions of IMs at steady-state are still unclear.

Here, we found that Tgfβ1, produced by lung vWF$^+$ blood vessel endothelial cells, shapes IM differentiation and imprints a core IM identity in the lung. In the absence of Tgfβ receptor in myeloid cells and of Tgfβ1 in endothelial cells, monocytes accumulating in lung tissue could not fully differentiate into functional IMs. Moreover, disruption of IM-intrinsic Tgfβ receptor signaling triggered development of age-related mechanical abnormalities, hyperinflation and collagen deposition. Our findings identify an endothelial-IM axis that contributes to IM development and can prevent the premature development of age-related defects, demonstrating a Tgfβ receptor-dependent homeostatic function of resident IMs.

Results

Lung endothelial Tgfβ1 – interstitial macrophage Tgfβ receptor interactions are inferred from single cell transcriptomics

IM development and function are thought to be shaped by microenvironmental cues, yet the ligand-receptor interactions involved remain poorly defined. To address this, we aimed to predict putative ligand-receptor interactions originating from lung structural cells and acting on IMs. Using NicheNet analyses (*21*), we analyzed single cell RNA-sequencing (scRNA-seq) data of lung IMs, Ly6C$^+$ classical monocytes (cMo) and non-hematopoietic lung niche cells including endothelial, epithelial and stromal cells captured at steady-state (*10*) (fig. S1). The top interactions between ligands expressed by niche cells and the corresponding receptors on IMs were visualized using a Circos plot (*22*) (Fig. 1A). *Csf1*, coding for Csf1 or macrophage colony-stimulating factor (M-CSF), was expressed by the three niche cell populations and was predicted to be involved in IM development via Csf1r signaling, consistent with previous findings (*11*, *14*). Of note, an interaction between endothelial cell-derived *Tgfb1* and IMs was also predicted (Fig. 1A). Analysis of predicted target genes triggered by Tgfβ1 signaling within receiver IMs revealed a high regulatory potential for the receptors *Tgfbr1* and *Tgfbr2*, as well as for various migration-related genes associated with integrin binding (i.e., *Itgb1*, *Itga4*, *Itgb5*, *Icam2*, *Itgax*, *Fn1*, *Igf1*, *Itga5*, *Calr*, *Thbs1*, *Icam1*) (Fig. 1B). Moreover, *Tgfb1* expression was higher in endothelial cells as compared to epithelial or stromal cells (Fig 1C).

Tgfβ1 can bind to membrane Tgfβ receptor II (TgfβRII) subunit, allowing cooperative binding to TgfβRI and downstream signaling (*23*). We assessed *Tgfbr1* and *Tgfbr2* expression in lung cMo, AMs, CD206$^-$ IMs and CD206$^+$ IMs in previously published bulk RNA-seq data (*11*). AMs and IMs expressed higher levels of *Tgfbr1* and *Tgfbr2* as compared to cMo (Fig. 1D). We next evaluated the protein expression of TgfβRI and TgfβRII on lung myeloid cells from WT mice by flow cytometry (fig. S2A). Lung monocytes, AMs and IMs expressed TgfβRI, whose levels were lower in both IM subsets as compared to AMs or cMo (fig. S2, B and C). While lung cMo and Ly6C$^-$ patrolling monocytes (pMo) expressed low levels of TgfβRII, its expression was elevated in AMs and in IMs, especially in the CD206$^+$ IM subset (Fig. 1, E and F). Lung neutrophils (Neu), conventional dendritic cells (cDCs) and blood myeloid cells also expressed lower levels of TgfβRII as compared to lung IMs (fig. S2, D and E). Together, our results indicate that IMs could be effective responders to Tgfβ through TgfβRII signaling, and that endothelial cells may represent an important source of Tgfβ1.

Lung endothelial Tgfβ1 triggers a core lung IM identity on Csf1-grown monocytes and macrophages *ex vivo*

We sought to investigate the potential impact of soluble factors including Tgfβ released from primary lung endothelial, epithelial, and stromal cells on monocyte differentiation and the acquisition of a distinct lung IM profile. To this end, bone marrow-derived monocytes (BM Mo) were isolated from the BM of WT mice, cultured for 48 hours in basal medium (Ctrl) or conditioned medium (CM) from FACS-sorted endothelial cells (CM-Endo), epithelial cells (CM-Epi) or stromal cells (CM-Stro) (fig. S2F) and subjected to bulk RNA sequencing (Fig. 2A). Principal component analysis (PCA) showed distinct clustering patterns for BM Mo exposed to distinct CM, indicating unique gene expression profiles induced by each CM (Fig. 2B). We generated gene set signatures of lung CD206$^+$ IMs, CD206$^-$ IMs and AMs based on our previously published scRNA-seq data (*10*) and mapped these signatures to CM-stimulated BM Mo using

Gene Set Enrichment Analysis (GSEA) (*24*). Of note, CM-Endo and CM-Stro triggered an enrichment in an IM signature regardless of the IM subset, but CM-Endo was the only treatment that stimulated a specific IM signature while not inducing an AM signature (Fig. 2C). These data suggest that lung endothelial cells release soluble signals that can imprint a specific IM signature.

Next, we investigated whether recombinant Tgfβ1 was sufficient to shift Csf1-grown BM Mo towards a lung IM gene expression profile. As opposed to AMs, bulk IMs can be specifically defined by elevated expression of Cx3cr1, Tmem119, MafB and C1q (*10–12*). Hence, BM Mo from WT (i.e., *Tgfbr2*$^{fl/fl}$) mice were cultured with Csf1 in the presence or absence of Tgfβ1 for 48 hours and assessed for expression of IM identity genes and proteins (Fig. 2D). Tgfβ1 significantly upregulated the transcript levels of *Mafb*, *C1qc*, *Cx3cr1*, *Tmem119* and *Csf1r* in Csf1-treated BM Mo, while it had no effect on *Tgfbr2* expression and downregulated the expression of the AM-specific transcription factor *Pparg* (Fig. 2E). At the protein level, MafB, C1qa, Cx3cr1 and Tmem119 were also significantly increased in Tgfβ1-treated Csf1-grown WT BM Mo as compared to untreated controls (Fig. 2, F and G).

To evaluate the impact of Tgfβ signaling through TgfβRII in this model, we used myeloid-specific *Tgfbr2*-deficient mice (*Lyz2*^{Cre} *Tgfbr2*$^{fl/fl}$ mice). A decrease in *Tgfbr2* expression and partial excision of the floxed allele were observed in BM Mo from *Lyz2*^{Cre} *Tgfbr2*$^{fl/fl}$ mice as compared to *Tgfbr2*$^{fl/fl}$ littermate controls (fig. S3). Of note, induction of IM identity marker genes and proteins were all decreased in Tgfβ1-treated *Tgfbr2*-deficient Csf1-grown BM Mo as compared to the WT counterparts, while Tgfβ1-triggered downregulation of *Pparg* was no longer observed in the absence of *Tgfbr2* (Fig. 2E-G). We also generated WT or *Tgfbr2*-deficient BM-derived macrophages (BMDMs) and treated them from day 7 till day 9 of culture with Tgfβ1 (fig. S4A-C). Tgfβ1-triggered and TgfβRII-mediated increases in the expression of IM-specific markers on differentiated BMDMs were also observed, as seen in BM Mo (fig. S4, D and E). Treatment of BM Mo with Csf2 and Tgfβ1, two cytokines required for AM development and identity (*5–7*), triggered an AM-associated signature independently of the concomitant presence of Csf1 (fig. S5, A and B) and did not induce expression of IM signature genes. Of note, the addition of Csf2 to Csf1- or Tgfβ1- and Csf1-grown BM Mo exerted an inhibitory effect on the expression of IM signature genes and *Tgfbr2* (fig. S5, C and D). Altogether, these results show that, in the presence of Csf1, Tgfβ1 can signal through TgfβRII to imprint a core IM signature in BM Mo or in BMDMs.

Finally, we asked whether co-culture of Csf1-grown BM Mo with lung primary endothelial cells (Endo) would trigger a similar TgfβRII-dependent IM signature (Fig. 2D). Co-culture of BM Mo with Endo induced an increase in the expression of the IM markers Cx3cr1, Tmem119, MafB and C1qa (Fig. 2, H and I). Of note, such induction of IM identity was abolished in the presence of LY364947, a TGFβ receptor inhibitor, and was decreased in BM Mo from *Lyz2*^{Cre} *Tgfbr2*$^{fl/fl}$ mice as compared to BM Mo from *Tgfbr2*$^{fl/fl}$ controls (Fig. 2, H and I). Our *ex vivo* results demonstrate that in the presence of Tgfβ1 and Csf1 or lung primary endothelial cells, BM Mo can acquire a Tgfβ receptor-dependent lung IM-specific phenotypic profile during macrophage differentiation.

Myeloid Tgfβ receptor signaling mediates lung IM development and identity *in vivo*

Next, we employed *Tmem119*^{Cre} *Cx3cr1*$^{LSL\text{-}DTR}$ mice (i.e., IM^{DTR} mice) (*11*), in which diphteria toxin (DT) treatment causes a bolus depletion of the IM niche that is rapidly refilled by cMo-derived *de novo* IMs. In order to evaluate the contribution of Tgfβ receptor signaling to IM development, we combined IM depletion in IM^{DTR} mice with intraperitoneal (i.p.) injections of the

Tgfβ receptor inhibitor LY363947 at days 2, 4 and 6 post-DT (Fig. 3A). At day 7 post-DT, the numbers of lung cMo and IMs were lower in LY363947-treated IM^{DTR} mice as compared to PBS-treated controls, while numbers of pMo and AMs remained unchanged (Fig. 3B). Of note, Tgfβ receptor inhibition was associated with a decrease in the numbers of both CD206^{-} IMs and CD206^{+} IMs (fig. S6A). Interestingly, this was associated with an increase in the proportion of apoptotic Annexin V^{+} lung cMo and IMs in LY364947-treated mice as compared to vehicle-treated counterparts (fig. S6B), while the proportion of blood Ly6C^{+} cMo was higher in LY363947-treated IM^{DTR} mice as compared to PBS-treated counterparts (fig; S6C) and the viability of BM and blood cMo were not affected by LY363947 (fig. S6D). These results suggested that Tgfβ receptor signaling impacted lung cMo and IM survival capacity, and was important for lung cMo recruitment or lung IM differentiation.

To assess whether myeloid-intrinsic Tgfβ receptor signaling played a role in either lung cMo recruitment or IM differentiation from cMo *in vivo*, we generated BM competitive chimeras in thorax-protected CD45.1/CD45.2 IM^{DTR} mice engrafted with a 1:1 BM cell mix from CD45.1 WT and CD45.2 *Lyz2^{Cre} Tgfbr2$^{fl/fl}$* mice (Fig. 3C). At week 4 post-transfer, donor chimerism of blood cMo exceeded 80 %, while AM donor chimerism was below 5%, indicating efficient BM donor reconstitution and thorax protection, respectively (Fig. 3, D and E). Seven days post-DT, we found that more than 85 % of IMs were of donor origin, confirming efficient depletion and BM reconstitution (Fig. 3, D and E). Lung cMo of donor origin arose equally from CD45.1 WT and CD45.2 *Lyz2^{Cre} Tgfbr2$^{fl/fl}$* cells, indicating that lung cMo recruitment was independent of Tgfβ receptor (Fig. 3, D-F). However, CD45.1 WT BM cells had a competitive advantage over CD45.2 *Lyz2^{Cre} Tgfbr2$^{fl/fl}$* cells to become IMs, regardless of the IM subset, suggesting that TgfβRII-deficient monocytes, once in the lung, failed to fully differentiate into IMs and reconstitute the IM pool (Fig. 3, D-F).

To further characterize lung monocytes and macrophages in the absence of myeloid-intrinsic TgfβRII, we compared their numbers, localization and identity by flow cytometry between myeloid-restricted *Tgfbr2*-deficient mice and littermate controls. First, IMs from *Lyz2^{Cre} Tgfbr2$^{fl/fl}$* mice exhibited a 60% reduction in *Tgfbr2* expression as compared to those from littermate controls (fig. S7A). Second, no abnormalities were found in the blood leukocyte composition of such transgenic mice (fig. S7B). As expected (*7*), AM numbers exhibited a 2-fold reduction in *Lyz2^{Cre} Tgfbr2$^{fl/fl}$* mice as compared to controls (Fig. 3G). Of note, IM numbers were also lower in *Lyz2^{Cre} Tgfbr2$^{fl/fl}$* mice as compared to controls (Fig. 3G) and the remaining IMs in *Lyz2^{Cre} Tgfbr2$^{fl/fl}$* mice exhibited a higher percentage of Annexin V^{+} cells as compared to control IMs, supporting that IMs are more sensitive to apoptosis in the absence of TgfβRII signaling (fig. S7C). The percentage of Ki-67^{+} cells was also higher in IMs from *Lyz2^{Cre} Tgfbr2$^{fl/fl}$* mice as compared to control IMs, suggesting that reduced cell proliferation does not account for the lower IM numbers in these mice (fig. S7D).

Flow-cytometry-based UMAP plot representation of monocytes and macrophages highlighted the appearance of a distinct cell population in *Lyz2^{Cre} Tgfbr2$^{fl/fl}$* mice (Fig. 3H). Back-gating analysis identified this population as Ly6C^{+}CD64^{+} monocytes (called CD64^{+} Mo) (Fig 3I), whose numbers were significantly increased in *Lyz2^{Cre} Tgfbr2$^{fl/fl}$* mice as compared to littermate controls (Fig. 3G). The phenotype of CD64^{+} Mo was reminiscent to that of transitioning CD64^{+} monocytes that appear during IM development in IM^{DTR} mice (*11*), but could also correspond to inflammatory monocytes or macrophages recruited when inflammation is present (*10*, *15*). Hence, we evaluated the expression of pro-inflammatory genes on lung extracts of *Lyz2^{Cre} Tgfbr2$^{fl/fl}$* and littermate control mice and found no evidence of inflammation in the absence of myeloid *Tgfbr2* in 8-12-

week-old mice (fig. S7E). Next, we assessed the localization of CD64$^+$ Mo. To this end, we labeled intravascular cells by intravenous (i.v.) injection of anti-CD45-FITC antibodies 10 minutes before sacrifice, and airway cells by intratracheal (i.t.) injection of anti-CD45-APC antibodies 5 minutes before sacrifice. As expected, most cMo and pMo were intravascular, most AMs were in the airway lumen and most IMs were parenchymal, regardless of the mouse genotype (fig. S7, F and G). While the few lung CD64$^+$ Mo present in control mice were mostly intravascular, 70% of lung CD64$^+$ Mo from *Lyz2*^{Cre} *Tgfbr2*$^{fl/fl}$ mice were parenchymal (Fig. 3, J and K). These data further support the idea that, while monocyte entry in the tissue is not affected in the absence of intrinsic *Tgfbr2,* monocyte-to-IM differentiation is impaired and blocked at an early differentiation stage in the tissue. Finally, we found that both CD64$^+$ Mo and IMs from *Lyz2*^{Cre} *Tgfbr2*$^{fl/fl}$ mice exhibited a decrease in the expression of Cx3cr1 and Tmem119 as compared to CD64$^+$ Mo and IMs from littermate control mice (Fig. 3, L and M), supporting a loss of IM identity in the absence of myeloid *Tgfbr2*. Numbers of heart and skin macrophages were, however, similar between *Lyz2*^{Cre}*Tgfbr2*$^{fl/fl}$ and control mice (fig. S7H-J), suggesting that myeloid-intrinsic Tgfβ receptor signaling may play a more dominant role in the lung compared to other organs. Together, these results demonstrate that intrinsic TgfβR signaling plays an important role in imprinting a core IM identity during lung IM development *in vivo*.

Tgfβ1 acts in synergy with Csf1 to trigger a MafB-dependent IM identity

Next, we asked whether Tgfβ1 could trigger MafB expression, a transcription factor involved in IM development (*11*), in BM Mo (Fig. 4A). We observed that, while Tgfβ1 or Csf1 alone could trigger *Mafb*, the combination of both treatments was the most potent in upregulating *Mafb* expression, which correlated with the strongest induction of the IM identity genes *C1qc*, *Cx3cr1*, *Tmem119* and *Csf1r* (Fig. 4B). Of note, Csf1 treatment increased *Tgfbr2* expression, while Tgfβ1 treatment alone did not trigger expression of *Csf1r* nor *Tgfbr2* (Fig. 4B), suggesting that engagement of Csf1 signaling primes IM responsiveness to Tgfβ1. Supporting this hypothesis, Csf1 target gene activation preceded that of Tgfβ1 along monocyte-to-IM trajectory (*11*) (Fig. 4C).

Next, we asked whether Tgfβ1-mediated induction of IM identity on BM Mo was dependent on MafB by analyzing BM Mo from *Lyz2*^{Cre} *Mafb*$^{fl/fl}$ mice (*11*) (Fig. 4D), which did not express *Mafb* (Fig. 4E). In the absence of MafB, Tgfβ1 treatment was no longer able to trigger an IM identity gene expression profile in BM Mo (Fig. 4E). Moreover, *Tgfbr2* expression itself was decreased in the absence of MafB, suggesting that MafB could also directly or indirectly regulate *Tgfbr2* expression (Fig. 4E). This was further evidenced by the differential expression of *Mafb*, *Tgfbr2* and TgfβRII target genes along monocyte-to-IM trajectory (*11*). Indeed, *Mafb* and *Tgfbr2* showed similar upregulation patterns, and Tgfβ1 target gene activation progressively increased in both CD206$^-$ IM and CD206$^+$ IM differentiation pathways, supporting Tgfβ signaling engagement in both subsets (Fig. 4F). Moreover, many predicted target genes downstream of TgfβRII signaling with the highest regulatory potential (Fig. 1B) were upregulated during monocyte-to-IM development (Fig. 4G) but showed reduced expression in *Mafb*-deficient IMs from *Lyz2*^{Cre} *Mafb*$^{fl/fl}$ mice (*11*) as compared to the WT counterparts (Fig. 4H).

Finally, we quantified TgfβRII expression on IMs from *Lyz2*^{Cre} *Mafb*$^{fl/fl}$ and control mice and, while IMs from *Lyz2*^{Cre} *Mafb*$^{fl/fl}$ mice expressed detectable levels TgfβRII, TgfβRII expression was lower on IMs from *Lyz2*^{Cre} *Mafb*$^{fl/fl}$ mice as compared to the WT counterparts (Fig. 4, I and J), indicating that MafB could regulate TgfβRII expression in IMs. Altogether, these data support that Tgfβ1-Tgfβ receptor interactions can activate MafB-dependent pathways, which then regulates

IM-intrinsic TgfβRII expression and TgfβRII-dependent signaling events to mediate full development of mature IMs, in concert with Csf1.

vWF$^+$ blood vessel endothelial cells release Tgfβ1 to shape IM development and identity

Next, we sought to identify the cellular source of Tgfβ1 necessary for IM development *in vivo*. We assessed intracellular expression of latent Tgfβ1 in lung structural cells at steady-state by flow cytometry (fig. S2F). No Tgfβ1$^+$ cells were found in CD45$^-$EpCam$^+$CD31$^-$ epithelial cells nor in CD45$^-$EpCam$^-$CD31$^-$ stromal cells (Fig. 5, A and B). However, we found a substantial proportion of Tgfβ1$^+$ cells within CD45$^-$EpCam$^-$CD31$^+$ endothelial cells, which was restricted to the vWF$^+$ blood vessel compartment but not the CD90.2$^+$ lymphatic nor the vWF$^-$CD90.2$^-$ capillary compartment (*25*) (Fig. 5, A and B). We reasoned that latent Tgfβ1 would be released more readily in the lung microenvironment during replenishment of the IM niche. Thus, we depleted IMs by DT treatment in IM^{DTR} mice and tracked Tgfβ1$^+$ vWF$^+$ endothelial cells during IM niche replenishment. We found a decrease in the percentage of Tgfβ1$^+$ cells among vWF$^+$ endothelial cells at days 3, 5 and 7 post-DT, while levels had returned to baseline at day 14 post-DT (Fig. 5, C and D), consistent with the idea that vWF$^+$ endothelial cells release more latent Tgfβ1 when IM development from monocytes is accelerated. Accordingly, the levels of latent Tgfβ1 found in lungs of DT-treated IM^{DTR} mice at day 4 post-DT were higher as compared to those found in lungs of PBS-treated IM^{DTR} mice (Fig. 5E). We also found that CD68$^+$ myeloid cells were present in the vicinity of Erg1$^+$Tgfβ1$^+$ endothelial cells in lungs from IM^{DTR} mice that were treated with DT 4 days before (Fig. 5F), and we observed an increase in pairs of CD68$^+$ myeloid cells and Erg1$^+$Tgfβ1$^+$ endothelial cells that were less than 10 μm apart in such lungs as compared to PBS-treated controls (Fig. 5G). These data suggest that vWF$^+$ blood vessel endothelial cells could release Tgfβ1 and interact with tissue monocytes differentiating into IMs.

Lastly, we sought to formally address the contribution of endothelial Tgfβ1 to IM development and identity. We generated *Cdh5*^{CreERT2} *Tgfb1*$^{fl/fl}$ mice that would be conditionally deficient in *Tgfb1* in endothelial cells upon tamoxifen treatment. After weaning, *Cdh5*^{CreERT2} *Tgfb1*$^{fl/fl}$ and *Tgfb1*$^{fl/fl}$ littermate controls were fed tamoxifen for 28 days, followed by a normal diet. At day 49 post-weaning, we confirmed a decrease in *Tgfb1* mRNA levels within lung CD45$^-$EpCam$^-$CD31$^+$ endothelial cells from tamoxifen-fed *Cdh5*^{CreERT2} *Tgfb1*$^{fl/fl}$ compared to controls (Fig. 5, H and I). Similarly, the percentage of Tgfβ1$^+$ cells within vWF$^+$ endothelial cells and the levels of latent Tgfβ1 were lower in lungs from tamoxifen-fed *Cdh5*^{CreERT2} *Tgfb1*$^{fl/fl}$ mice as compared to controls (Fig. 5, H and I). Following co-culture of BM Mo with Csf1 and FACS-sorted endothelial cells from tamoxifen-fed *Cdh5*^{CreERT2} *Tgfb1*$^{fl/fl}$ mice or control counterparts, we found that endothelial cell-triggered induction of the IM markers Cx3cr1, Tmem119, MafB and C1qa was lower when Tgfβ1 was knocked down (Fig. 5J-L). In a separate cohort of mice, we lethally irradiated mice at day 35 post-weaning to deplete hematopoietic cells and IMs, and reconstituted them with donor CD45.1/CD45.2 BM cells (Fig. 5H). At day 14 post-reconstitution, the majority of blood cells and 50% of CD45$^+$ lung cells were of donor origin, regardless of the host genotype (fig. S8). *In vivo*, both the numbers and the percentage of donor IMs within CD45$^+$ cells were decreased in *Cdh5*^{CreERT2} *Tgfb1*$^{fl/fl}$ mice as compared to littermate controls (Fig. 5M), demonstrating that IM development was impaired when endothelial Tgfβ1 expression was decreased. In addition, expression levels of Cx3cr1 and Tmem119 were decreased in IMs from *Cdh5*^{CreERT2} *Tgfb1*$^{fl/fl}$ mice as compared to those from control mice (Fig. 5, N and O), indicating that endothelial Tgfβ1 can shape IM identity. Altogether, these data provide evidence that vWF$^+$ blood vessel endothelial cells represent an important source of Tgfβ1 to support IM development.

Myeloid *Tgfbr2* deficiency is associated with a proliferative and dysfunctional IM profile

Next, we explored the potential functional consequences of IM-specific *Tgfbr2* deficiency. To this end, we generated a mouse strain in which AMs would retain TgfβRII expression while IMs would be deficient. CD45.1/CD45.2 IM^{DTR} mice were lethally irradiated with thorax protection and were fully reconstituted with BM cells either from CD45.2 *Tgfbr2*$^{fl/fl}$ mice or CD45.2 *Lyz2*^{Cre} *Tgfbr2*$^{fl/fl}$ mice (Fig. 6A). Four weeks later, chimeric IM^{DTR} mice were treated with DT to specifically empty the IM niche and trigger IM niche refilling from either control or *Tgfbr2*-deficient monocytes. We confirmed that AMs and IMs were of host and donor origin, respectively (Fig. 6B). Bulk RNA-seq was performed on donor CD64$^+$ cells encompassing CD64$^+$ Mo and IMs at day 10 post-DT (fig. S9A) and knock-down of *Tgfbr2* exon 2 was confirmed (fig. S9B). PCA and unsupervised hierarchical clustering showed that control IMs clustered separately from *Tgfbr2*-deficient IMs (Fig. 6, C and D). Differential expression (DE) analyses showed 79 upregulated genes in WT IMs and 152 upregulated genes in *Tgfbr2*-deficient IMs (adjusted P value < 0.05 and $\log_2$ fold change $>$ or $<$ 1, respectively) (Fig. 6E). We confirmed the downregulation of the IM identity genes *Cx3cr1* and *Tmem119* in the absence of *Tgfbr2* (Fig. 6F). Further, using Gene Set Enrichment Analyses (GSEA), genes known to be upregulated or downregulated upon Tgfβ1 stimulation were enriched in *Tgfbr2*-sufficient or deficient IMs, respectively, validating the model (Fig. 6G). Of note, *Tgfbr2*-deficient IMs were enriched in responses related to cell cycling and proliferation, further supporting that, in the absence of *Tgfbr2*, IMs are blocked in a premature proliferative stage that precedes IM differentiation (*11*). Moreover, responses related to cell-cell adhesion were enriched in *Tgfbr2*-deficient IMs. Conversely, a range of responses associated with homeostatic and immunoregulatory functions of macrophages were enriched in *Tgfbr2*-sufficient IMs, such as activation of mTORC1 signaling (*26*), antigen processing and presentation (*19*), and a signature of tolerogenic macrophages (Fig. 6G).

ScRNA-seq analysis of lung CD45.1$^-$CD45.2$^+$Ly6G$^-$SiglecF$^-$CD11b$^+$SSC^{lo}CD64$^+$ cells isolated at day 90 post-DT from myeloid-intrinsic *Tgfbr2*-deficient chimeric IM^{DTR} mice indicated an accumulation of monocytes (*Ly6c2, Ccr2, Irf8*) expressing *Fcgr4*, reminiscent of tissue monocytes (*10*), at the expense of CD206$^-$ IMs (*Cd72, Cd74, H2-Eb1*) and CD206$^+$ IMs (*Mrc1, Folr2*), compared to controls (Fig. 6H-J). DE and gene Ontology (GO) analyses highlighted an enrichment in monocytes from *Tgfbr2*-deficient chimeric IM^{DTR} mice in the response to type II interferons (*Irf1, Cxcl9, Stat1*), cell-cell adhesion (*Vasp, Sdc4, Ccl5*), cell proliferation (*Mif, Cd38*) and apoptotic signaling as compared to those from *Tgfbr2*-sufficient controls (Fig. 6, K and L), supporting that tissue monocytes substantially contribute to the transcriptional changes observed by bulk RNA-seq. Our data thus support that TGFβ receptor signaling is essential for the differentiation and homeostatic functions of IMs, preventing their accumulation in an immature, proliferative state.

Myeloid Tgfβ receptor signaling drives monocyte and IM spatial organization in the lung microenvironment

Next, we used codetection by indexing (CODEX)-enabled multiplex imaging to investigate how monocyte and IM spatial niche occupancies were affected by the loss of Tgfβ receptor signaling (*27*, *28*). Using a 28-parameter staining panel, we identified donor monocytes and IMs (fig. S10) as well as other lung immune and structural cell types using established markers (Table S2). Within the donor CD45.1$^-$CD45.2$^+$ population, we observed a higher proportion of monocytes in lungs from myeloid-intrinsic *Tgfbr2*-deficient chimeric IM^{DTR} mice compared to *Tgfbr2*-sufficient controls (Fig. 7A), confirming our flow cytometry and scRNA-seq data. Monocytes in myeloid-intrinsic *Tgfbr2*-deficient chimeric IM^{DTR} mice predominantly accumulated in the adventitial cuffs surrounding larger blood vessels (Fig. 7, B and C), which are composed of vWF^{+} endothelial cells (*25*). We next examined how cell interactions between monocytes, IMs and their microenvironment were influenced by the loss of IM-intrinsic TGFβ receptor signaling. Interaction scores of monocytes with endothelial cells and fibroblasts, and to a lesser with epithelial cells, were reduced in lungs from myeloid-intrinsic *Tgfbr2*-deficient chimeric IM^{DTR} mice as compared to the *Tgfbr2*-sufficient controls (Fig. 7D). A similar reduction in interaction score with endothelial cells was observed for *Tgfbr2*-deficient IMs (Fig. 7D), consistent with a role for Tgfβ receptor signaling in the positioning of monocytes and IMs in dedicated niches. We also found that the interaction score of monocytes with IMs was higher in the absence of myeloid TgfβRII (Fig. 7D), suggesting that IMs were retained in close proximity to monocytes and failed to migrate properly towards their specific niches. While in control lungs, monocytes were closer to Tgfβ^{+} endothelial cells than to Tgfβ^{-} endothelial cells, supporting a preferential interaction, the distance between monocytes and Tgfβ^{+} endothelial cells was markedly increased in the absence of myeloid TgfbRII (Fig. 7, E and F). These data suggested that TGFβ receptor signaling is crucial for guiding monocytes and IMs to their dedicated niches and facilitating interactions with lung structural cells.

Loss of myeloid Tgfβ receptor signaling leads to premature development of lung age-associated abnormalities

To assess the consequences of IM-intrinsic *Tgfbr2* deficiency on lung homeostasis, we performed lung function measurements, histopathological analyses and protein quantification in chimeric IM^{DTR} mice whose IMs were sufficient or deficient in *Tgfbr2,* at 4 months post-DT (Fig. 6A). Of note, blood myeloid cells, lung neutrophils and lung DCs expressed lower levels of TgfβRII as compared to IMs (fig. S2, D and E), indicating that they are unlikely to represent major confounding factors in the model. We noticed a substantial death of chimeric IM^{DTR} mice in the absence of myeloid *Tgfbr2* from 2 months post-DT (fig. S11A), in line with previous reports suggesting that myeloid *Tgfbr2* deficiency can trigger stroke (*29*). Importantly, we only analyzed mice that were healthy without weight loss or other signs of morbidity. Lungs from myeloid-intrinsic *Tgfbr2*-deficient mice displayed higher inspiratory capacity, higher compliance and lower elastance as compared to control lungs (Fig. 8A; fig. S11B), a phenotype that was similarly observed in 18-month-old WT mice as compared to 2-month-old WT mice (Fig. 8A; fig. S11B). These data are consistent with the hypothesis that, in the absence of *Tgfbr2* on IMs, lungs develop age-related functional abnormalities. A higher degree of alveolar dilatation was observed in lungs of donor *Lyz2*^{Cre} *Tgfbr2*$^{fl/fl}$ mice as compared to donor *Tgfbr2*$^{fl/fl}$ mice (Fig. 8, B and C), a phenotype similar to senile hyperinflation (*30*). Perivascular accumulation of leukocytes, among which CD68^{+} monocytic cells close to vWF^{+} endothelial cells, was observed in lungs of donor *Lyz2*^{Cre} *Tgfbr2*$^{fl/fl}$ mice (Fig. 8, B, D and E). At the protein level, lungs of donor *Lyz2*^{Cre} *Tgfbr2*$^{fl/fl}$ mice contained lower levels of many cytokines, chemokines and growth factors as compared to those of donor *Tgfbr2*$^{fl/fl}$ mice (Fig. 8E), supporting an impairment of lung immune surveillance when IMs cannot engage Tgfβ receptor pathways. Moreover, lungs of donor *Lyz2*^{Cre} *Tgfbr2*$^{fl/fl}$ chimeric mice displayed lower levels of IL-10, an immunosuppressive cytokine produced by IMs (*9*, *10*, *15*, *17*) (Fig. 8F), lower levels of elastin (Fig. 8G) and higher levels of soluble collagen (Fig. 8H) as compared to those of donor *Tgfbr2*$^{fl/fl}$ mice. Altogether, these data supported that disruption of IM-specific TgfβRII signaling has a profound impact on the lung immunoregulatory environment and triggers age-related changes.

Discussion

Here, we found that blood vessel-associated vWF$^+$ endothelial cells provide Tgfβ1 to monocytes entering the lung tissue in order to allow their transition towards functional lung IMs. Disruption of myeloid-intrinsic Tgfβ receptor signaling resulted in the accumulation of monocytes and immature IMs in adventitial cuffs and an impairment of IM development, identity and niche occupancy, which was associated with changes in the lung immunoregulatory environment and age-related abnormalities. These observations highlight a previously undescribed endothelial-IM axis involved in lung homeostasis and the preservation of lung integrity at steady-state.

Tgfβ signaling plays an important role in RTM biology and tissue adaptation. In the gut, neuron-associated muscularis macrophages are instructed by Tgfβ from the enteric nervous system (*31*) and colonic macrophage differentiation also requires Tgfβ receptor signaling (*32*). In the lung, AMs rely on both Csf2 and autocrine Tgfβ for their development, maintenance and homeostatic functions (*7*). Notably, Csf2-cultured fetal monocytes can differentiate into AM-like cells when treated with Tgfβ (*7*). Similarly, BM Mo cultured with Csf2 and Tgfβ1 upregulated AM signature genes. However, in Csf1-treated BM Mo, Tgfβ1 induced MafB expression, thus promoting IM-like differentiation while repressing PPAR-γ. Adding Csf2 to Csf1- and Tgfβ1-containing cultures suppressed IM-specific genes and *Tgfbr2*, suggesting that Csf2 dominates over Csf1 by favoring AM fate. Thus, Tgfβ1 appears to act as a context-dependent co-factor, synergizing with Csf1 to drive MafB-dependent IM-associated pathways, but enhancing AM-specific programs in the presence of Csf2. The substantial downregulation of *Tgfbr2* in Csf2-treated cultures might limit the ability of Tgfβ1 to drive IM-like differentiation, although it could also paradoxically constrain its ability to promote full AM development. *In vivo*, these dynamics are likely influenced by the spatial and temporal availabilities of Csf1, Csf2 and Tgfβ1. In the brain, microglia rely on Tgfβ1 for their development and identity, and disruption of Tgfβ receptor signaling in adult microglia results in an aberrant activation phenotype and neurological disorders (*33–36*). While lung IMs and microglia differ in origin and other aspects, they share a common gene signature characterized by elevated *Cx3cr1*, *Tmem119*, *MafB* and *C1q* expression (*11*, *33*, *37*), a signature that is induced by Tgfβ1. The source of Tgfβ1 is, however, different, as microglia produce Tgfβ1 autonomously (*38*, *39*), while lung IMs receive it from endothelial cells. Our observations suggest that a combination of signals can act in concert to imprint a functional specification of RTMs in tissues. In the lung, besides Csf1 and Tgfβ1 contributing to global IM development (*11*, *14*, *40*, *41*), the identification of IM subset-specific microenvironmental signals that act within tissular niches to functionally imprint distinct IM subpopulations will require further investigation.

In the IM^{DTR} mouse model, previously developed to investigate monocyte-to-IM differentiation (*11*), we observed a decrease in intracellular Tgfβ1 within vWF$^+$ blood vessel endothelial cells during IM differentiation and niche refilling. This was accompanied by a concomitant increase in lung Tgfβ1 level and decreased distance between Tgfβ1$^+$ endothelial cells and CD68$^+$ monocytes, suggesting a direct interaction during IM development. Furthermore, inhibiting Tgfβ receptor signaling during IM niche refilling led to a reduction in both CD206$^+$ and CD206$^-$ IM subsets, supporting a role for Tgfβ1-Tgfβ receptor interactions in IM development before subset-specific differentiation occurs. BM mixed chimeras experiments in thorax-protected, DT-treated IM^{DTR} mice further supported that myeloid-intrinsic *Tgfbr2* expression conferred a competitive advantage to differentiate into both IM subsets. Of note, we found that Tgfβ1 could synergistically act with Csf1 to trigger MafB, a regulator of IM development (*11*), the expression of IM signature genes (i.e., *Cx3cr1*, *Tmem119*, *C1q*), as well as the upregulation of TgfβRII expression. In microglia, Tgfβ1 has been shown to promote *Cx3cr1* (*42*) and *Tmem119* (*43*) expression, possibly via Smad activation downstream of Tgfβ receptor signaling and the presence of Smad binding elements in their promoter sequences (*42*, *43*). Although CD206^{-} IMs express lower levels of TGFβRII compared to CD206^{+} IMs**,** our findings suggest that TGFβ signaling plays a role in the differentiation of both IM subsets from monocytes, likely at an early stage of monocyte-to-IM transition. This is consistent with the early requirement for MafB in IM differentiation, despite its higher expression in CD206^{+} IMs (11). Hence, our data are consistent with the idea that monocytes, once extravasated in the tissue, first require activation of Csf1 signaling to upregulate TgfβRII. Such process primes IM precursors for Tgfβ responsiveness and allows sensing of endothelial Tgfβ1 and Tgfβ signaling engagement to trigger MafB, induce expression of migration-associated genes downstream of TgfβRII and pursue their migration and differentiation trajectory in the lung. Further supporting this idea, myeloid *Tgfbr2* deficiency was associated with the accumulation of parenchymal CD64^{+} monocytes held in a proliferative state, i.e., the precursors of IMs (*11*) and a reduction in IM numbers, as well as a loss of their identity markers Cx3cr1 and Tmem119. While the decrease in IM numbers in *Lyz2*^{Cre} *Tgfbr2*$^{fl/fl}$ mice was modest, we speculate that some remaining IMs may still express TgfβRII, given that LysM-Cre-driven *Tgfbr2* depletion is not complete in myeloid cells.

In the last part of the study, we uncovered a role for endothelial Tgfβ1-IM TgfβRII interactions in the prevention of age-related lung abnormalities. To this end, we generated a chimeric mouse strain in which IMs, but not AMs, did not express *Tgfbr2*, overcoming previous limitations due to the lack of tools specifically targeting IMs. Bulk and single-cell RNA-seq analyses of monocytes and IMs in these chimeric mice revealed an immature, proliferative and dysfunctional IM profile in the absence of *Tgfbr2*. Multiplex imaging further supported that Tgfβ-signaling mediated endothelial-IM interactions guide IM precursors towards specific niches in the lung. Without TgfβRII signaling, monocytes and immature IMs accumulated in adventitial cuffs, suggesting that they failed to activate intrinsic migration programs or sense extrinsic positional cues, such as chemokines from lung structural niche cells. Such reduced interaction with their microenvironment likely impaired IM imprinting, survival and functional specification. Consequently, niche cells might lack the necessary IM support to sustain their homeostatic functions. Additionally, the perivascular accumulation of immature monocytes could itself contribute to the development of age-related abnormalities developing when IM-intrinsic TgfβRII is disrupted. By 6 months of age, the lungs of those mice exhibited increased compliance and decreased elastance, resembling the phenotype of 18-month-old WT mice. Alveolar enlargements, increased collagen and decreased elastin contents were also observed as compared to control lungs, processes known to occur with age and predispose to lung diseases (*30*, *44*). Moreover, the levels of many cytokines and growth factors, including IL-10, were reduced in the absence of IM-intrinsic *Tgfbr2*, potentially compromising immune surveillance and tissue integrity. IMs may directly or indirectly regulate the extracellular matrix (ECM) by modulating ECM-degrading enzymes such as matrix metalloproteinases, which were decreased in lungs containing *Tgfbr2*-deficient IMs, or by producing IL-10, know to regulate ECM deposition (*45*, *46*). While their cellular source remains to be identified, other factors found to be decreased in lungs with *Tgfbr2*-deficient IMs are potential suppressors of fibroblast-driven collagen deposition, such as adiponectin (*47*)**,** HGF (*48*) or pentraxin-2 (*49*). Excessive collagen deposition and elastin degradation could then contribute to lung stiffening and alveolar enlargements, both hallmarks of aging lungs (*50–52*). Finally, IMs may also play a role in preserving the integrity of the alveolar-capillary barrier by interacting with epithelial and endothelial cells. Loss of TGFβRII signaling in IMs may disrupt their ability to occupy dedicated niches and to promote the production of growth factors and cytokines that maintain endothelial and epithelial integrity and functions, including adiponectin (*53*), angiopoietin-1 (*54*), amphiregulin (*55*) and lipocalin-2 (*56*). Identifying the precise IM-driven mechanisms involved, and whether specific IM subsets preferentially carry out such homeostatic functions, represent interesting avenues for future research.

In conclusion, our work identifies an endothelial-myeloid crosstalk involving Tgfβ1-Tgfβ receptor interactions, which constantly takes place during IM transition from monocytes in adult mice. Disruption of such pathway critically impacts lung homeostasis and triggers the premature development of age-related changes, highlighting an essential role for lung IMs in supporting tissue integrity and immune homeostasis at steady-state via Tgfβ receptor-dependent mechanisms.

Materials and Methods

Study design

In this study, we investigated the niche-derived signals instructing lung IM development and identity and the functional consequences for lung homeostasis. To this end, we employed *ex vivo* and *in vivo* approaches combined with transcriptional profiling, flow cytometry, multiplex imaging, bone marrow (BM) chimeras, IM^{DTR} mice, gene targeting and lung functional and histopathological analyses. For most mouse experiments, group sizes ranged from 3 to 6 mice to ensure sufficient statistical power (≥80%) with a significance threshold of 5%. In some experiments, sample sizes were not predetermined using statistical methods; however, they were consistent with those reported in previous studies (*10*, *11*, *57*, *58*). Unless specified otherwise, data from independent experiments were pooled for analysis with each panel. No data were excluded, and all replication attempts were successful, yielding comparable results. Lung section histopathological were assessed in a blinded manner. Detailed information on sample sizes, experimental replicates, and the statistical analyses can be found in the corresponding figure legends.

Mice

All experiments, unless otherwise specified, were performed on age-matched 8–12-wk-old male and female mice on the C57BL/6 background. In this study, the following mice were used on the C57BL/6 background: CD45.2 WT (The Jackson Laboratory), CD45.1 WT (The Jackson Laboratory, 002014), *Lyz2*^{Cre} (The Jackson Laboratory, 004781), *Mafb*$^{fl/fl}$ (*11*), *Tgfbr2*$^{fl/fl}$ (The Jackson Laboratory, 012603), *Cdh5*^{CreERT2} (Taconic Biosciences, 13073), *Tgfb1*$^{fl/fl}$ (The Jackson Laboratory, 065809), and *Tmem119*^{Cre} *Cx3cr1*$^{LSL\text{-}DTR/+}$ mice, called IM^{DTR} mice (*11*). Myeloid-restricted *Tgfbr2* or *Mafb* depletion was achieved by crossing *Tgfbr2*$^{fl/fl}$ or *Mafb*$^{fl/fl}$ mice with *Lyz2*^{Cre} mice. *CD45.1/CD45.2 IM*^{DTR} mice were generated by crossing CD45.1 *Tmem119*^{Cre} with *CD45.2 Cx3cr1*$^{LSL\text{-}DTR}$ mice. *Cdh5*^{CreERT2} and *Tgfb1*$^{fl/fl}$ mice were crossed to produce *Cdh5*^{CreERT2} *Tgfb1*$^{fl/fl}$ mice.

Mice were housed under specific pathogen-free conditions and maintained in a 12-h light–dark cycle with food and water ad libitum. Experiments were reviewed and approved by the Institutional Animal Care and Use Committee of the University of Liège (ethical approval #1956). The 'Guide for the Care and Use of Laboratory Animals', prepared by the Institute of Laboratory Animal Resources, National Research Council, and published by the National Academy Press, as well as European and local legislations, was followed carefully. Accordingly, the temperature and relative humidity were 21°C and 45-60%, respectively.

In vivo treatments with chemicals and antibodies

For DT-induced depletion of IMs, IM^{DTR} mice were administered a single i.p. injection of 50 ng DT (List Biological Labs, 150), while control mice were injected with PBS. In TgfβR inhibitor experiments, IM^{DTR} mice received three i.p. injection of 1 mg/kg body weight LY364947 (Selleckchem, S2805) in 200 µl PBS at days 2, 4 and 6 post-DT. Control mice were injected with 200 µl PBS i.p..

For assessment of cell localization in the lung, 1 µg of FITC-conjugated anti-mouse CD45.2 (clone 104, BD Biosciences, 564616) was injected i.v. 10 minutes before, and 1 µg of APC-conjugated anti-mouse CD45.2 (clone 104, BD Biosciences, 558702) was injected i.t. 5 min before sacrifice to distinguish intravascular (CD45-FITC$^+$ CD45-APC$^-$), parenchymal (CD45-FITC$^-$ CD45-APC$^-$) and airway (CD45-FITC$^-$ CD45-APC$^+$) cells.

To achieve endothelial-specific *Tgfb1* deletion, four-week-old *Cdh5^{CreERT2} Tgfb1$^{fl/fl}$* mice or *Tgfb1$^{fl/fl}$* control were fed tamoxifen diet (0.25g/kg, SAFE, E8404A01R 00008) for 4 weeks, then were fed with normal diet afterwards.

Reagents and antibodies

A complete list of the reagents and antibodies used in this manuscript can be found in Table S1.

Flow cytometry

Cells (0.5 - 5 × 10^6) were pre-incubated with Mouse Fc Block (BD Biosciences, 553142) to avoid nonspecific binding to Fc receptors and then stained with appropriate antibodies at 4 °C in the dark for 10 mins. Unless otherwise instructed, all antibodies are diluted 1:100 for staining at 4 °C for 30 mins. Cell viability was assessed using LIVE/DEAD Fixable Near-IR (775) stain (Thermo Fisher, L34976), and cell apoptosis was detected by Annexin V after surface staining, according to the manufacturer's instructions. TgfβRII (R&D Systems, FAB532P), Cx3cr1 (R&D systems, FAB5825G) and Tmem119 (ThermoFisher, 12-6119-82) stainings were performed at 37 °C for 30 mins with a 1:50 dilution. Intracellular cytokine staining was performed using an intracellular staining set (ThermoFisher, 00-5523-00). For Ki-67 staining, cells were permeabilized and stained extracellularly using FITC Mouse Anti-Ki67 Set (BD Biosciences, 556026). Annexin V/PI stainings were performed at room temperature for 15 min. The cell suspensions were analyzed with an LSRFortessa (BD Biosciences). FlowJo software (BD Biosciences) was used for data analysis. For the bulk and scRNA-seq experiments, lung CD45.1$^-$CD45.2$^+$Ly6G$^-$SiglecF$^-$CD11b$^+$SSC^{lo}CD64$^+$ Macs (CD64$^+$ Mo and IMs) were sorted using a Sony MA900. To generate conditioned medium (CM), endothelial cells (CD45$^-$CD31$^+$Epcam$^-$), epithelial cells (CD45$^-$CD31$^-$Epcam$^+$) and stromal cells (CD45$^-$CD31$^-$Epcam$^-$) were sorted using a FACSAria III (BD Biosciences). The list of antibodies used can be found in the Table S1.

Generation of BM (competitive) chimeras

Eight-week-old CD45.1$^+$CD45.2$^+$ IM^{DTR} mice were anesthesized via i.p. injection of xylazine (10 mg/kg; Bayer, 0076901) and ketamine (75 mg/kg; Dechra, 804132) in 200 µl PBS. A 0.6-cm-thick lead shield was used to protect the thoracic cavity, and the mice underwent lethal irradiation in two 6 Gy doses, spaced 15 min apart. After regaining consciousness, they were i.v. administrated with 10^7 BM cells from either CD45.2$^+$ *Tgfbr2$^{fl/fl}$* or CD45.2$^+$ *Lyz2^{Cre}Tgfbr2$^{fl/fl}$* donors. For generating mixed BM chimeras, mice received 10^7 BM cells comprising an equal mixture of CD45.1$^+$ WT cells and CD45.2$^+$ *Lyz2^{Cre}Tgfbr2$^{fl/fl}$* cells via i.v injection. Nine-week-old *Cdh5^{CreERT2} Tgfb1$^{fl/fl}$* mice were lethally irradiated with two doses of 4 Gy, 15 mins apart. The mice were injected i.v. with 10^7 BM cells from CD45.1.2 wild-type mice after 2 h irradiation and were treated with 0.05 mg/ml of enrofloxacin (Baytril, Bayer) in drinking water for 4 weeks from the day of irradiation.

Ex vivo BM Mo and BMDM experiments

To generate conditioned medium (CM), FACS-sorted lung endothelial cells, epithelial cells and stromal cells were cultured in RPMI medium (ThemoFisher, 21875-034) containing 10% vol/vol FBS, 50 U/ml Penicillin-Streptomycin (ThemoFisher, 15070-063), 1 mM sodium pyruvate (ThemoFisher, 11360-070), 1 × MEM NEAA (ThemoFisher, 11140-035) and 50 µM 2-

Mercaptoethanol (ThemoFisher, 31350-010) at 37 °C. After 12 h, the conditioned medium was collected by centrifugation to obtain the supernatant. BM Ly6C$^+$ monocytes were isolated from mice using the Monocyte Isolation Kit (Miltenyi Biotec, 130-100-629). These monocytes were then treated with CM, while the control monocytes were cultured in the medium at 37 °C for 48 h. BM Mo were then collected and RNA was extracted by Trizol.

BM Ly6C$^+$ monocytes were isolated from *Tgfbr2*$^{fl/fl}$, *Lyz2*^{Cre} *Tgfbr2*$^{fl/fl}$, *Mafb*$^{fl/fl}$, *Lyz2*^{Cre} *Mafb*$^{fl/fl}$ mice and treated with or without 20 ng/ml Tgfβ1 together with 40 ng/ml Csf1 or Csf2 at 37 °C for 48h. All samples were analyzed by flow cytometry or RT-qPCR.

For co-culture experiments, endothelial cells were isolated from mouse lung single cell suspensions using the CD31 MicroBeads Kit (Miltenyi Biotec, 130-097-418) and co-cultured with BM Mo from *Tgfbr2*$^{fl/fl}$ or *Lyz2*^{Cre} *Tgfbr2*$^{fl/fl}$ mice with 40 ng/ml Csf1 at 37 °C for 48h. One co-culture group from *Tgfbr2*$^{fl/fl}$ mice were treated with 5 µM TgfβR inhibitor LY-364947(Selleckchem, S2805). The ratio of endothelial cells and BM Mo was 2:1 in Fig. 2 H-I and 1:2 in Fig. 5 J-L.

For the generation of BMDM, BM Mo were treated with 40 ng/ml Csf1 on first day, and the medium containing 40 ng/ml Csf1 was changed twice at day 3 and day 5 day. At day 7, 95% cells were F4/80$^+$CD11b$^+$ as confirmed by flow cytometry.

CODEX stainings, imaging, processing and analysis

Frozen lung sections from chimeric IM^{DTR} mice were prepared for CODEX staining using a 28-plex antibody panel. Following fixation, photobleaching, and blocking, samples were stained overnight and processed for imaging. CODEX imaging was performed using a widefield fluorescence microscope, capturing multiple channels with z-spacing of 1.5 µm. Raw files were processed for background subtraction, stitching, and cell segmentation.

Cell populations were identified and classified using fluorescence markers and a strategy akin to flow cytometry (Table S2), and downstream analyses were performed. Additional details can be found in the Supplementary Materials.

Statistical analysis

Graphs were generated using GraphPad Prism 10 (GraphPad software) or R Bioconductor (version 3.5.1). As indicated in the figure legends, parametric tests were conducted under the assumption of normal data distribution. No data were excluded from the analyses. Statistical tests were conducted using Prism 9 (GraphPad Software) and R Bioconductor (3.5.1) with the Seurat package utilized for scRNA-seq data analysis. The specific statistical methods used for each experiment are detailed in the corresponding figure legends. Statistical significance was defined as $P < 0.05$, with significance levels indicated as follows: *, $P < 0.05$; **, $P < 0.01$; ***, $P < 0.001$; ****, $P < 0.0001$; ns, not significant).

Additional sections and details about Materials and Methods can be found in the Supplemental Materials.

Supplementary Materials

Materials and Methods
Fig. S1. Transcriptional identity of lung structural and myeloid cells analyzed by NicheNet analyses.
Fig. S2. Flow cytometry gating strategies and expression of Tgfβ receptors by blood and lung myeloid cells.
Fig. S3. Efficiency of *Tgfbr2* deletion in BM Mo from *Lyz2*^{Cre} *Tgfbr2*$^{fl/fl}$ mice.
Fig. S4. Stimulation of Csf1-grown BM-derived Macs (BMDMs) with Tgfβ1 triggers a core IM identity.
Fig. S5. Csf2 and Tgfβ1 drive AM-associated gene expression while suppressing IM-specific signature in BM Mo.
Fig. S6. Numbers of IM subsets and viability of Ly6C^{+} cMo, Ly6C^{-} pMo, AMs and IMs in LY363947-treated IM-depleted IM^{DTR} mice at day 7 post-DT.
Fig. S7. Analysis of 2-month-old myeloid-restricted *Tgfbr2*-deficient mice.
Fig. S8. Donor CD45.1/CD45.2 chimerism in the blood and lung of chimeric *Cdh5*^{CreERT2} *Tgfb1*$^{fl/fl}$ mice.
Fig. S9. *Tgfbr2* depletion in donor IMs from donor *Tgfbr2*$^{fl/fl}$ or donor *Lyz2*^{Cre} *Tgfbr2*$^{fl/fl}$ chimeric IM^{DTR} mice.
Fig. S10. Identification of donor CD45.1^{-}CD45.2^{+} monocytes and IMs in lungs of donor *Tgfbr2*$^{fl/fl}$ and donor *Lyz2*^{Cre} *Tgfbr2*$^{fl/fl}$ chimeric IM^{DTR} mice.
Fig. S11. Survival and lung function of donor *Tgfbr2*$^{fl/fl}$ or donor *Lyz2*^{Cre} *Tgfbr2*$^{fl/fl}$ chimeric IM^{DTR} mice.
Table S1. List of reagents, antibodies, commercial assays, primers and softwares used in this study.
Table S2. CODEX phenotypes.
Data file S1. Raw data file
Reproducibility checklist

References and notes

1. H. Aegerter, B. N. Lambrecht, C. V. Jakubzick, Biology of lung macrophages in health and disease. *Immunity* **55**, 1564–1580 (2022).
2. J. Schyns, F. Bureau, T. Marichal, Lung Interstitial Macrophages: Past, Present, and Future. *J Immunol Res* **2018**, 5160794 (2018).
3. M. Guilliams, F. R. Svedberg, Does tissue imprinting restrict macrophage plasticity? *Nat Immunol* **22**, 118–127 (2021).
4. C. Schneider, S. P. Nobs, M. Kurrer, H. Rehrauer, C. Thiele, M. Kopf, Induction of the nuclear receptor PPAR-gamma by the cytokine GM-CSF is critical for the differentiation of fetal monocytes into alveolar macrophages. *Nat Immunol* **15**, 1026–37 (2014).
5. J. Gschwend, S. P. M. Sherman, F. Ridder, X. Feng, H.-E. Liang, R. M. Locksley, B. Becher, C. Schneider, Alveolar macrophages rely on GM-CSF from alveolar epithelial type 2 cells before and after birth. *J Exp Med* **218**, e20210745 (2021).
6. M. Guilliams, I. De Kleer, S. Henri, S. Post, L. Vanhoutte, S. De Prijck, K. Deswarte, B. Malissen, H. Hammad, B. N. Lambrecht, Alveolar macrophages develop from fetal monocytes that differentiate into long-lived cells in the first week of life via GM-CSF. *The J Exp Med* **210**, 1977–92 (2013).
7. X. Yu, A. Buttgereit, I. Lelios, S. G. Utz, D. Cansever, B. Becher, M. Greter, The Cytokine TGF-β Promotes the Development and Homeostasis of Alveolar Macrophages. *Immunity* **47**, 903-912.e4 (2017).
8. M. Liegeois, C. Legrand, C. J. Desmet, T. Marichal, F. Bureau, The interstitial macrophage: A long-neglected piece in the puzzle of lung immunity. *Cell Immunol* **330**, 91–96 (2018).
9. S. Chakarov, H. Y. Lim, L. Tan, S. Y. Lim, P. See, J. Lum, X.-M. Zhang, S. Foo, S. Nakamizo, K. Duan, W. T. Kong, R. Gentek, A. Balachander, D. Carbajo, C. Bleriot, B. Malleret, J. K. C. Tam, S. Baig, M. Shabeer, S.-A. E. S. Toh, A. Schlitzer, A. Larbi, T. Marichal, B. Malissen, J. Chen, M. Poidinger, K. Kabashima, M. Bajenoff, L. G. Ng, V. Angeli, F. Ginhoux, Two distinct interstitial macrophage populations coexist across tissues in specific subtissular niches. *Science* **363**, eaau0964 (2019).
10. J. Schyns, Q. Bai, C. Ruscitti, C. Radermecker, S. De Schepper, S. Chakarov, F. Farnir, D. Pirottin, F. Ginhoux, G. Boeckxstaens, F. Bureau, T. Marichal, Non-classical tissue monocytes and two functionally distinct populations of interstitial macrophages populate the mouse lung. *Nat Commun* **10**, 3964 (2019).
11. D. Vanneste, Q. Bai, S. Hasan, W. Peng, D. Pirottin, J. Schyns, P. Maréchal, C. Ruscitti, M. Meunier, Z. Liu, C. Legrand, L. Fievez, F. Ginhoux, C. Radermecker, F. Bureau, T. Marichal, MafB-restricted local monocyte proliferation precedes lung interstitial macrophage differentiation. *Nat Immunol* **24**, 827–840 (2023).

12. X. Li, A. B. Mara, S. C. Musial, F. W. Kolling, S. L. Gibbings, N. Gerebtsov, C. V. Jakubzick, Coordinated chemokine expression defines macrophage subsets across tissues. *Nat Immunol* **25**, 1110–1122 (2024).

13. S. A. Dick, A. Wong, H. Hamidzada, S. Nejat, R. Nechanitzky, S. Vohra, B. Mueller, R. Zaman, C. Kantores, L. Aronoff, A. Momen, D. Nechanitzky, W. Y. Li, P. Ramachandran, S. Q. Crome, B. Becher, M. I. Cybulsky, F. Billia, S. Keshavjee, S. Mital, C. S. Robbins, T. W. Mak, S. Epelman, Three tissue resident macrophage subsets coexist across organs with conserved origins and life cycles. *Sci Immunol* **7**, eabf7777 (2022).

14. B. B. Ural, S. T. Yeung, P. Damani-Yokota, J. C. Devlin, M. de Vries, P. Vera-Licona, T. Samji, C. M. Sawai, G. Jang, O. A. Perez, Q. Pham, L. Maher, P. Loke, M. Dittmann, B. Reizis, K. M. Khanna, Identification of a nerve-associated, lung-resident interstitial macrophage subset with distinct localization and immunoregulatory properties. *Sci Immunol* **5**, eaax8756 (2020).

15. C. Sabatel, C. Radermecker, L. Fievez, G. Paulissen, S. Chakarov, C. Fernandes, S. Olivier, M. Toussaint, D. Pirottin, X. Xiao, P. Quatresooz, J. C. Sirard, D. Cataldo, L. Gillet, H. Bouabe, C. J. Desmet, F. Ginhoux, T. Marichal, F. Bureau, Exposure to Bacterial CpG DNA Protects from Airway Allergic Inflammation by Expanding Regulatory Lung Interstitial Macrophages. *Immunity* **46**, 457–473 (2017).

16. B. B. Ural, S. T. Yeung, P. Damani-Yokota, J. C. Devlin, M. de Vries, P. Vera-Licona, T. Samji, C. M. Sawai, G. Jang, O. A. Perez, Q. Pham, L. Maher, P. Loke, M. Dittmann, B. Reizis, K. M. Khanna, Identification of a nerve-associated, lung-resident interstitial macrophage subset with distinct localization and immunoregulatory properties. *Sci Immunol* **5** (2020).

17. D. Bedoret, H. Wallemacq, T. Marichal, C. Desmet, F. Quesada Calvo, E. Henry, R. Closset, B. Dewals, C. Thielen, P. Gustin, L. de Leval, N. Van Rooijen, A. Le Moine, A. Vanderplasschen, D. Cataldo, P. V. Drion, M. Moser, P. Lekeux, F. Bureau, Lung interstitial macrophages alter dendritic cell functions to prevent airway allergy in mice. *J Clin Invest* **119**, 3723–38 (2009).

18. X.-Z. Tang, L. S. M. Kreuk, C. Cho, R. J. Metzger, C. D. C. Allen, Bronchus-associated macrophages efficiently capture and present soluble inhaled antigens and are capable of local Th2 cell activation. *Elife* **11**, e63296 (2022).

19. C. Legrand, D. Vanneste, A. Hego, C. Sabatel, K. Mollers, J. Schyns, P. Maréchal, J. Abinet, A. Tytgat, M. Liégeois, B. Polese, M. Meunier, C. Radermecker, L. Fiévez, F. Bureau, T. Marichal, Lung Interstitial Macrophages Can Present Soluble Antigens and Induce Foxp3+ Regulatory T Cells. *Am J Respir Cell Mol Biol* **70**, 446-456 (2024).

20. C. Ruscitti, C. Radermecker, T. Marichal, Journey of monocytes and macrophages upon influenza A virus infection. *Curr Opin Virol* **66**, 101409 (2024).

21. R. Browaeys, W. Saelens, Y. Saeys, NicheNet: modeling intercellular communication by linking ligands to target genes. *Nat Methods* **17**, 159–162 (2020).

22. M. Krzywinski, J. Schein, İ. Birol, J. Connors, R. Gascoyne, D. Horsman, S. J. Jones, M. A. Marra, Circos: An information aesthetic for comparative genomics. *Genome Res* **19**, 1639–1645 (2009).

23. J. L. Wrana, L. Attisano, R. Wieser, F. Ventura, J. Massagué, Mechanism of activation of the TGF-beta receptor. *Nature* **370**, 341–347 (1994).

24. A. Subramanian, P. Tamayo, V. K. Mootha, S. Mukherjee, B. L. Ebert, M. A. Gillette, A. Paulovich, S. L. Pomeroy, T. R. Golub, E. S. Lander, J. P. Mesirov, Gene set enrichment analysis: a knowledge-based approach for interpreting genome-wide expression profiles. *Proc Natl Acad Sci U S A* **102**, 15545–50 (2005).

25. D. Grant, N. Wanner, M. Frimel, S. Erzurum, K. Asosingh, Comprehensive phenotyping of endothelial cells using flow cytometry 1: Murine. *Cytometry A* **99**, 251–256 (2021).

26. Q. Li, H. Cheng, Y. Liu, X. Wang, F. He, L. Tang, Activation of mTORC1 by LSECtin in macrophages directs intestinal repair in inflammatory bowel disease. *Cell Death Dis* **11**, 918 (2020).

27. S. Black, D. Phillips, J. W. Hickey, J. Kennedy-Darling, V. G. Venkataraaman, N. Samusik, Y. Goltsev, C. M. Schürch, G. P. Nolan, CODEX multiplexed tissue imaging with DNA-conjugated antibodies. *Nat Protoc* **16**, 3802–3835 (2021).

28. Y. Goltsev, N. Samusik, J. Kennedy-Darling, S. Bhate, M. Hale, G. Vazquez, S. Black, G. P. Nolan, Deep Profiling of Mouse Splenic Architecture with CODEX Multiplexed Imaging. *Cell* **174**, 968-981.e15 (2018).

29. M. C. Hollander, L. L. Latour, D. Yang, H. Ishii, Z. Xiao, Y. Min, A. Ray-Choudhury, J. Munasinghe, A. S. Merchant, P. C. Lin, J. Hallenbeck, M. Boehm, L. Yang, Attenuation of Myeloid-Specific TGFβ Signaling Induces Inflammatory Cerebrovascular Disease and Stroke. *Circ Res* **121**, 1360–1369 (2017).

30. G. Sharma, J. Goodwin, Effect of aging on respiratory system physiology and immunology. *Clin Interv Aging* **1**, 253–260 (2006).

31. M. F. Viola, M. Chavero-Pieres, E. Modave, M. Delfini, N. Stakenborg, M. C. Estévez, N. Fabre, I. Appeltans, T. Martens, K. Vandereyken, H. Theobald, J. Van Herck, P. Petry, S. Verheijden, S. De Schepper, A. Sifrim, Z. Liu, F. Ginhoux, M. Azhar, A. Schlitzer, G. Matteoli, K. Kierdorf, M. Prinz, P. Vanden Berghe, T. Voet, G. Boeckxstaens, Dedicated macrophages organize and maintain the enteric nervous system. *Nature* **618**, 818–826 (2023).

32. A. Schridde, C. C. Bain, J. U. Mayer, J. Montgomery, E. Pollet, B. Denecke, S. W. F. Milling, S. J. Jenkins, M. Dalod, S. Henri, B. Malissen, O. Pabst, A. Mcl Mowat, Tissue-specific differentiation of colonic macrophages requires TGFβ receptor-mediated signaling. *Mucosal Immunol* **10**, 1387–1399 (2017).

33. O. Butovsky, M. P. Jedrychowski, C. S. Moore, R. Cialic, A. J. Lanser, G. Gabriely, T. Koeglsperger, B. Dake, P. M. Wu, C. E. Doykan, Z. Fanek, L. Liu, Z. Chen, J. D. Rothstein, R. M. Ransohoff, S. P. Gygi, J. P. Antel, H. L. Weiner, Identification of a unique TGF-β-

dependent molecular and functional signature in microglia. *Nat Neurosci* **17**, 131–143 (2014).

34. H. Lund, M. Pieber, R. Parsa, D. Grommisch, E. Ewing, L. Kular, J. Han, K. Zhu, J. Nijssen, E. Hedlund, M. Needhamsen, S. Ruhrmann, A. O. Guerreiro-Cacais, R. Berglund, M. J. Forteza, D. F. J. Ketelhuth, O. Butovsky, M. Jagodic, X.-M. Zhang, R. A. Harris, Fatal demyelinating disease is induced by monocyte-derived macrophages in the absence of TGF-β signaling. *Nat Immunol* **19**, 1–7 (2018).

35. T. Zöller, A. Schneider, C. Kleimeyer, T. Masuda, P. S. Potru, D. Pfeifer, T. Blank, M. Prinz, B. Spittau, Silencing of TGFβ signalling in microglia results in impaired homeostasis. *Nat Commun* **9**, 4011 (2018).

36. S. G. Utz, P. See, W. Mildenberger, M. S. Thion, A. Silvin, M. Lutz, F. Ingelfinger, N. A. Rayan, I. Lelios, A. Buttgereit, K. Asano, S. Prabhakar, S. Garel, B. Becher, F. Ginhoux, M. Greter, Early Fate Defines Microglia and Non-parenchymal Brain Macrophage Development. *Cell* **181**, 557-573.e18 (2020).

37. O. Matcovitch-Natan, D. R. Winter, A. Giladi, S. Vargas Aguilar, A. Spinrad, S. Sarrazin, H. Ben-Yehuda, E. David, F. Zelada González, P. Perrin, H. Keren-Shaul, M. Gury, D. Lara-Astaiso, C. A. Thaiss, M. Cohen, K. Bahar Halpern, K. Baruch, A. Deczkowska, E. Lorenzo-Vivas, S. Itzkovitz, E. Elinav, M. H. Sieweke, M. Schwartz, I. Amit, Microglia development follows a stepwise program to regulate brain homeostasis. *Science* **353**, aad8670 (2016).

38. A. Bedolla, E. Wegman, M. Weed, M. K. Stevens, K. Ware, A. Paranjpe, A. Alkhimovitch, I. Ifergan, A. Taranov, J. D. Peter, R. M. S. Gonzalez, J. E. Robinson, L. McClain, K. M. Roskin, N. H. Greig, Y. Luo, Adult microglial TGFβ1 is required for microglia homeostasis via an autocrine mechanism to maintain cognitive function in mice. *Nat Commun* **15**, 5306 (2024).

39. G. L. McKinsey, N. Santander, X. Zhang, K. Kleemann, L. Tran, A. Katewa, K. Conant, M. Barraza, K. Waddell, C. Lizama, M. La Russa, H. J. Koo, H. Lee, D. Mukherjee, H. Paidassi, E. S. Anton, K. Atabai, D. Sheppard, O. Butovsky, T. D. Arnold, Radial glia promote microglial development through integrin αVβ8 -TGFβ1 signaling. *bioRxiv*, 2023.07.13.548459 (2023).

40. M. Greter, I. Lelios, P. Pelczar, G. Hoeffel, J. Price, M. Leboeuf, T. M. Kündig, K. Frei, F. Ginhoux, M. Merad, B. Becher, Stroma-derived interleukin-34 controls the development and maintenance of langerhans cells and the maintenance of microglia. *Immunity* **37**, 1050–1060 (2012).

41. Y. Wang, K. J. Szretter, W. Vermi, S. Gilfillan, C. Rossini, M. Cella, A. D. Barrow, M. S. Diamond, M. Colonna, IL-34 is a tissue-restricted ligand of CSF1R required for the development of Langerhans cells and microglia. *Nat Immunol* **13**, 753–760 (2012).

42. S. Chen, D. Luo, W. J. Streit, J. K. Harrison, TGF-beta1 upregulates CX3CR1 expression and inhibits fractalkine-stimulated signaling in rat microglia. *J Neuroimmunol* **133**, 46–55 (2002).

43. A. Attaai, N. Neidert, A. von Ehr, P. S. Potru, T. Zöller, B. Spittau, Postnatal maturation of microglia is associated with alternative activation and activated TGFβ signaling. *Glia* **66**, 1695–1708 (2018).

44. S. J. Cho, H. W. Stout-Delgado, Aging and Lung Disease. *Annu Rev Physiol* **82**, 433–459 (2020).

45. A. Moroguchi, K. Ishimura, K. Okano, H. Wakabayashi, T. Maeba, H. Maeta, Interleukin-10 Suppresses Proliferation and Remodeling of Extracellular Matrix of Cultured Human Skin Fibroblasts. *Eur Surg Res* **36**, 39–44 (2004).

46. S. Reitamo, A. Remitz, K. Tamai, J. Uitto, Interleukin-10 modulates type I collagen and matrix metalloprotease gene expression in cultured human skin fibroblasts. *J Clin Invest* **94**, 2489–2492 (1994).

47. R. G. Marangoni, Y. Masui, F. Fang, B. Korman, G. Lord, J. Lee, K. Lakota, J. Wei, P. E. Scherer, L. Otvos, T. Yamauchi, N. Kubota, T. Kadowaki, Y. Asano, S. Sato, W. G. Tourtellotte, J. Varga, Adiponectin is an endogenous anti-fibrotic mediator and therapeutic target. *Sci Rep* **7**, 4397 (2017).

48. B. Crestani, S. Marchand-Adam, C. Quesnel, L. Plantier, K. Borensztajn, J. Marchal, A. Mailleux, P. Soler, M. Dehoux, Hepatocyte Growth Factor and Lung Fibrosis. *Proc Am Thorac Soc* **9**, 158–163 (2012).

49. D. Pilling, R. H. Gomer, Persistent Lung Inflammation and Fibrosis in Serum Amyloid P Component (Apcs-/-) Knockout Mice. *PLoS ONE* **9**, e93730 (2014).

50. D. Sicard, A. J. Haak, K. M. Choi, A. R. Craig, L. E. Fredenburgh, D. J. Tschumperlin, Aging and anatomical variations in lung tissue stiffness. *Am J Physiol Lung Cell Mol Physiol* **314**, L946–L955 (2018).

51. S. Kononov, K. Brewer, H. Sakai, F. S. A. Cavalcante, C. R. Sabayanagam, E. P. Ingenito, B. Suki, Roles of Mechanical Forces and Collagen Failure in the Development of Elastase-induced Emphysema. *Am J Respir Crit Care Med* **164**, 1920–1926 (2001).

52. S. Meiners, O. Eickelberg, M. Königshoff, Hallmarks of the ageing lung. *Eur Respir J* **45**, 807–827 (2015).

53. K. Nakanishi, Y. Takeda, S. Tetsumoto, T. Iwasaki, K. Tsujino, H. Kuhara, Y. Jin, I. Nagatomo, H. Kida, S. Goya, T. Kijima, N. Maeda, T. Funahashi, I. Shimomura, I. Tachibana, I. Kawase, Involvement of Endothelial Apoptosis Underlying Chronic Obstructive Pulmonary Disease–like Phenotype in Adiponectin-null Mice: Implications for Therapy. *Am J Respir Crit Care Med* **183**, 1164–1175 (2011).

54. M. Jeansson, A. Gawlik, G. Anderson, C. Li, D. Kerjaschki, M. Henkelman, S. E. Quaggin, Angiopoietin-1 is essential in mouse vasculature during development and in response to injury. *J Clin Invest* **121**, 2278–2289 (2011).

55. L. A. Monticelli, G. F. Sonnenberg, M. C. Abt, T. Alenghat, C. G. K. Ziegler, T. A. Doering, J. M. Angelosanto, B. J. Laidlaw, C. Y. Yang, T. Sathaliyawala, M. Kubota, D. Turner, J. M. Diamond, A. W. Goldrath, D. L. Farber, R. G. Collman, E. J. Wherry, D. Artis, Innate lymphoid cells promote lung-tissue homeostasis after infection with influenza virus. *Nat Immunol* **12**, 1045–1054 (2011).

56. H. Saiga, J. Nishimura, H. Kuwata, M. Okuyama, S. Matsumoto, S. Sato, M. Matsumoto, S. Akira, Y. Yoshikai, K. Honda, M. Yamamoto, K. Takeda, Lipocalin 2-Dependent Inhibition of Mycobacterial Growth in Alveolar Epithelium. *J Immunol* **181**, 8521–8527 (2008).

57. C. Radermecker, C. Sabatel, C. Vanwinge, C. Ruscitti, P. Maréchal, F. Perin, J. Schyns, N. Rocks, M. Toussaint, D. Cataldo, S. L. Johnston, F. Bureau, T. Marichal, Locally instructed CXCR4hi neutrophils trigger environment-driven allergic asthma through the release of neutrophil extracellular traps. *Nat Immunol* **20**, 1444–1455 (2019).

58. C. Ruscitti, J. Abinet, P. Maréchal, M. Meunier, C. de Meeûs, D. Vanneste, P. Janssen, M. Dourcy, M. Thiry, F. Bureau, C. Schneider, B. Machiels, A. Hidalgo, F. Ginhoux, B. G. Dewals, J. Guiot, F. Schleich, M.-M. Garigliany, A. Bellahcène, C. Radermecker, T. Marichal, Recruited atypical Ly6G+ macrophages license alveolar regeneration after lung injury. *Sci Immunol* **9**, eado1227 (2024).

59. F. Bayerl, D. A. Bejarano, G. Bertacchi, A.-C. Doffin, E. Gobbini, M. Hubert, L. Li, P. Meiser, A.-M. Pedde, W. Posch, L. Rupp, A. Schlitzer, M. Schmitz, B. U. Schraml, S. Uderhardt, J. Valladeau-Guilemond, D. Wilflingseder, V. Zaderer, J. P. Böttcher, Guidelines for visualization and analysis of DC in tissues using multiparameter fluorescence microscopy imaging methods. *Eur J Immunol* **53**, e2249923 (2023).

60. C. R. Stoltzfus, J. Filipek, B. H. Gern, B. E. Olin, J. M. Leal, Y. Wu, M. R. Lyons-Cohen, J. Y. Huang, C. L. Paz-Stoltzfus, C. R. Plumlee, T. Pöschinger, K. B. Urdahl, M. Perro, M. Y. Gerner, CytoMAP: A Spatial Analysis Toolbox Reveals Features of Myeloid Cell Organization in Lymphoid Tissues. *Cell Rep* **31**, 107523 (2020).

61. G. Crowley, S. Kwon, E. J. Caraher, S. H. Haider, R. Lam, P. Batra, D. Melles, M. Liu, A. Nolan, Quantitative lung morphology: semi-automated measurement of mean linear intercept. *BMC Pulm Med* **19**, 206 (2019).

62. P.-E. Grillet, E. Desplanche, Q. Wynands, F. Gouzi, P. Bideaux, A. Fort, V. Scheuermann, A. Lacampagne, A. Virsolvy, J. Thireau, P. De Tombe, A. Bourdin, O. Cazorla, Diastolic Cardiomyopathy Secondary to Experimentally Induced Exacerbated Emphysema. *Am J Respir Cell Mol Biol* **69**, 230–241 (2023).

63. B. Singh, K. Shinagawa, C. Taube, E. W. Gelfand, R. Pabst, Strain-specific differences in perivascular inflammation in lungs in two murine models of allergic airway inflammation. *Clin Exp Immunol* **141**, 223–229 (2005).

64. P. M. Wang, D. L. Kachel, M. F. Cesta, W. J. Martin, Direct Leukocyte Migration across Pulmonary Arterioles and Venules into the Perivascular Interstitium of Murine Lungs during Bleomycin Injury and Repair. *Am J Pathol* **178**, 2560–2572 (2011).

Acknowledgments

We thank all members of the Immunophysiology laboratory (GIGA Institute, Liège, Belgium) for discussions; S. Ormenese, R. Stefan, A. Hego, G. Lefevre, C. Vanwinge and J.-M. Collard from the GIGA *In Vitro* Imaging Platform; P. Drion, G. Lambert, L., B. Remy and all staff members from the GIGA Mouse facility and Transgenics Platform; W. Coppieters, L. Karim, M. Deckers, A. Mayer, A. Lavergne and members from the GIGA Genomics Platform; P. Maréchal, M. Di Cesare, M. Sarlet, R. Fares, I. Sbai and A. Lio for their excellent technical and administrative support.

Funding

FRFS-Welbio Advanced Grant WELBIO-CR-2022A-10 (TM); ERC Starting Grant ERC StG 2018 IM-ID: 801823 (TM); ERC Consolidator Grant ERC CoG 2023 MoMacTrajectALI: 101124390 (TM); Baillet Latour Biomedical Fund (TM); Research Project of the F.R.S.-FNRS T015021F (TM); Research Concerted Action of the Fédération Wallonie-Bruxelles (TM); Deutsche Forschungsgemeinschaft (DFG, German Research Foundation) under Germany's Excellence Strategy – EXC2151 – 390873048 (AS); SFB 1454-P05-432325352 (AS).

Author contributions

TM conceived, supervised and secured funding for the project; QB supervised the project and performed bioinformatic analyses; WP, DV, QB and TM designed the experiments; WP did most of the experiments, compiled the data and prepared the figures. DV, MM and CR were implicated in experiments related to the analysis of myeloid-restricted *Tgfbr2*- and endothelial-restricted *Tgfb1*-deficient mice; JA performed bioinformatic analyses; DB and AS performed the Codex multiplex imaging experiment and analyses; FB was involved in experiments involving myeloid-restricted *Mafb*-deficient mice; FP and DC performed the invasive measurements of lung function; TM, QB and WP wrote the manuscript; all authors provided feedback on the manuscript.

Competing interests

Authors declare that they have no competing interests.

Data and materials availability

Bulk and single cell RNA-seq data have been deposited at the Gene Expression Omnibus (GEO) and are available under GEO accession GSE271467 and GSE285104. Previously published scRNA-seq data (*10*, *11*) were deposited at EMBL-EBI under accession number E-MTAB-7678 (*10*) and at GEO under GEO accession GSE194021 (*11*). The bulk RNA-seq data of cMo, AMs and IM subsets in lungs of adult C57BL/6 WT mice used in Fig. 1D were previously published and deposited at GEO under GEO accession GSE194021 (*11*). Original codes have been deposited at Zenodo and are available at: https://zenodo.org/records/14974309. Tabulated data underlying the figures is provided in data file S1. All other data needed to support the conclusions of the paper are present in the paper or the Supplementary Materials.

Fig. 1. Endothelial Tgfβ1 – IM Tgfβ receptor interactions are predicted during IM development. (**A**) Circos plot depicting the putative interactions between structural cell-derived ligands (bottom) and IM-intrinsic receptors (top), evaluated by NicheNet analysis of scRNA-seq data of lung monocytes, IMs and structural cells from naïve C57BL/6 WT mice (*10*). Opacity of the arrows correlates with the interaction score. (**B**) Heatmap depicting predicted ligand activity within lung endothelial cells and IM-intrinsic target gene activation during IM development, based on NicheNet analyses as in (A). (**C**) Expression of *Tgfb1* within lung primary endothelial cells (Endo), epithelial cells (Epi) and stromal cells (Stro), extracted from the scRNA-seq data, as in (A), and depicted by violin plots (height: expression; width: abundance of cells). (**D**) Expression of *Tgfbr1* and *Tgfbr2* within lung cMo, AMs, CD206^{-} IMs and CD206^{+} IMs of naïve C57BL/6 WT mice, extracted by bulk RNA-seq data analyses (*11*). (**E**) Representative histograms and (**F**) bar graph showing normalized MFI of TgfβRII expression in lung cMo, pMo, AMs and IMs from naïve C57BL/6 WT mice. (D,F) Data show mean +/- SEM (D) *n*=3 biological replicates of FACS-sorted cells; (F) Data are representative of 3 independent experiments (*n*=3 mice). *P* values were calculated using (C) a one-way ANOVA with Games-Howell's post hoc tests or (D) a two-way ANOVA with Dunnett's post hoc tests or (F) a one-way ANOVA with Dunnett's post hoc tests. *, $P<0.05$; ***, $P<0.001$; ****, $P<0.0001$. MFI, mean fluorescence intensity.

Fig. 2. Lung endothelial Tgfβ1 triggers a core IM signature on Csf1-grown BM Mo and BMDMs. (**A**) Experimental outline for (B, C). BM Mo from WT mice were cultured in basal medium (Ctrl) or conditioned medium (CM) from lung primary endothelial (CM-Endo), epithelial (CM-Epi) or stromal (CM-Stro) cells and subjected to bulk RNA-seq analyses 48 hours later. (**B**) Principal Component Analysis (PCA) plot of the BM Mo bulk RNA-seq data, as in (A). (**C**) Gene Set Enrichment Analysis (GSEA) comparing the transcriptome of CM-stimulated BM Mo, as in (A), with signature gene sets characteristic of CD206^{+} IMs, CD206$^{−}$ IMs and AMs. **D**) Experimental outline for (E-I). BM Mo from *Tgfbr2$^{fl/fl}$* or *Lyz2^{Cre} Tgfbr2$^{fl/fl}$* mice were (E-G) stimulated with Csf1 or Csf1 + Tgfβ1 or (H,I) co-cultured with or without lung primary endothelial cells (Endo) in the presence or absence of the TgfβR inhibitor LY364947, and analyzed 48 hours later. (**E**) Relative mRNA expression of the indicated genes in BM Mo, as in (D). (**F**) Representative histograms and (**G**) bar graph showing MFI of MafB, C1qa, Cx3cr1 and Tmem119 expression in BM Mo, as in (D). (**H**) Representative histograms and (**I**) bar graph showing MFI of MafB, C1qa, Cx3cr1 and Tmem119 expression in BM Mo, as in (D). (E,G,I) Data show mean +/- SEM and are representative of 3 independent experiments (n=3-6 mice). *P* values were calculated using (E) a two-way ANOVA with Tukey's post hoc tests, (G,I) a one-way ANOVA with Dunnett's post hoc tests. *, $P<0.05$; **, $P<0.01$; ***, $P<0.001$; ****, $P<0.0001$. MFI, mean fluorescence intensity; ns, not significant. FDR, Falso Discovery Rate; NES, Normalized Enrichment Score.

Fig. 3. Loss of Tgfβ receptor signaling impedes monocyte-to-IM development and IM identity *in vivo*. (**A**) Experimental outline for (B, C). (**B**) Absolute numbers of lung cMo, pMo, AMs and IMs in PBS- or LY364947-treated IM^{DTR} mice at day 7 post-DT, as in (A). (**C**) Experimental outline for (D-F). (**D**) Representative CD45.1 and CD45.2 contour plots and (**E**) bar graph showing % of host CD45.1/CD45.2, donor CD45.1 WT and donor CD45.2 *Lyz2^{Cre} Tgfbr2$^{fl/fl}$* chimerism in the indicated cell populations, assessed 7 days post-DT treatment in chimeric IM^{DTR} mice, as in (C). (**F**) Quantification of donor CD45.2 *Lyz2^{Cre} Tgfbr2$^{fl/fl}$* chimerism relative to donor CD45.1 WT chimerism in the indicated cell populations, as in (D). (**G**) Absolute numbers of the indicated lung myeloid cell populations evaluated by flow cytometry in *Lyz2^{Cre} Tgfbr2$^{fl/fl}$* mice and in *Tgfbr2$^{fl/fl}$* littermate controls. (**H**) Representative UMAP plots of lung CD45^{+}CD11b^{+} and/or CD11c^{+} cells analyzed by flow cytometry in *Lyz2^{Cre} Tgfbr2$^{fl/fl}$* mice and in *Tgfbr2$^{fl/fl}$* littermate controls (merged data from 2 mice per group). (**I**) Representative Ly6C and CD64 plots of lung CD45^{+}SSC^{lo}CD11b^{+}F4/80^{+} cells from *Lyz2^{Cre} Tgfbr2$^{fl/fl}$* mice and *Tgfbr2$^{fl/fl}$* littermate controls. (**J**) Representative CD45-i.v. and CD45-i.t. plots of lung CD64^{+} Mo from *Lyz2^{Cre} Tgfbr2$^{fl/fl}$* mice and *Tgfbr2$^{fl/fl}$* littermate controls injected with anti-CD45-FITC Ab i.v. and anti-CD45-APC Ab i.t. before sacrifice. (**K**) Percentages of tissue (CD45-i.v.$^{-}$/CD45-i.t.$^{-}$), airway (CD45-i.v.$^{-}$/CD45-i.t.$^{+}$) and intravascular (CD45-i.v.$^{+}$/CD45-i.t.$^{-}$) CD64^{+} Mo, as in (K). (**L**) Representative histograms and (**M**) bar graph showing MFI of Cx3cr1 and Tmem119 expression in IMs and the indicated lung myeloid cell populations of *Lyz2^{Cre} Tgfbr2$^{fl/fl}$* mice and *Tgfbr2$^{fl/fl}$* littermate controls. (B,E,F,G,K,M) Data show (B,M) mean +/- SEM and are representative of 2-3 independent experiments (n=4-6 mice), and (F) individual mice are representative of 3 independent experiments (n=4 mice), (G,K) mean +/- SEM are pooled from 3-4 replicates (n=4 mice). *P* values were calculated using (B,M) a unpaired Student's *t* test, (F) a paired multiple *t* test, (G) a Wilcoxon rank sum test or (K) a two-way ANOVA with Sidak's post-hoc tests. *, $P<0.05$; **, $P<0.01$; ***, $P<0.001$; ****, $P<0.0001$. Ab, antibody; MFI, mean fluorescence intensity; ns, not significant.

Fig. 4. Reciprocal regulation of MafB- and Tgfβ receptor-dependent pathways in IMs. (**A**) Experimental outline for (B). BM Mo from WT C57BL/6 mice were stimulated with Tgfβ1, Csf1 or Csf1 + Tgfβ1 for 48 hours and were analyzed by RT-qPCR. Freshly isolated BM Mo were used as controls. (**B**) Relative mRNA expression of the indicated genes in BM Mo, as in (A). (**C**) Signature scores of Csf1 and Tgfβ1 target genes along pseudotime during monocyte-to-IM development, based on the scRNA-seq mapping of monocyte-to-IM trajectory (*11*). (**D**) BM Mo from *Mafb*$^{fl/fl}$ or *Lyz2*^{Cre} *Mafb*$^{fl/fl}$ mice were stimulated with Csf1 or Csf1 + Tgfβ1 for 48 hours and were analyzed by RT-qPCR. (**E**) Relative mRNA expression of the indicated genes in BM Mo, as in (D). (**F**) Expression of *Mafb* (left)*, Tgfbr2* (middle), and signature scores of Tgfβ1 target genes (right) along pseudotime evaluated by TradeSeq in monocyte-to-IM trajectories (both CD206^{-} and CD206^{+} IM trajectories) (*11*). (**G**) Heatmap showing expression of the indicated genes along pseudotime during monocyte-to-IM trajectories, as in (F). (**H**) Dot plot showing average expression and % of cells expressing the indicated genes in clusters of classical monocytes (cMo), patrolling monocytes (pMo), WT IMs and MafB-deficient IMs, based on previously published scRNA-seq data (*11*). (**I**) Representative histograms and (**J**) bar graph showing normalized MFI of TgfβRII expression in lung from *Lyz2*^{Cre} *Mafb*$^{fl/fl}$ mice or *Mafb*$^{fl/fl}$ littermate controls. (B,E,J) Data shown mean +/- SEM and are representative of 3 independent experiments (n=3-4 mice). *P* values were calculated using (B) a two-way ANOVA with Dunnett's post hoc tests, (E) a two-way ANOVA with Tukey's post hoc tests or (J) a two-tailed unpaired Student's *t* test. *, *P*<0.05; **, *P*<0.01; ***, *P*<0.001; ****, *P*<0.0001. MFI, mean fluorescence intensity; ns, not significant.

Fig. 5. Lung vWF$^+$ endothelial-derived Tgfβ1 contributes to IM development and identity. (**A**) Representative histogram of latent Tgfβ1 expression in lung epithelial cells (Epi), stromal cells (Stro) and endothelial cells (Endo) from C57BL/6 WT mice. Endo were further divided into CD90.2$^-$vWF$^-$ capillary, CD90.2$^+$ lymphatic and vWF$^+$ blood vessel Endo. (**B**) Percentage of Tgfβ1$^+$ cells in the indicated cell populations, as in (A). (**C**) Representative histogram of latent Tgfβ1 expression in lung vWF$^+$ blood vessel Endo from DT-treated IM^{DTR} mice at the indicated time points post-DT. (**D**) Percentage of Tgfβ1$^+$ cells within lung vWF$^+$ blood vessel Endo, as in (C). (**E**) Levels of latent Tgfβ1, assessed by ELISA on lung extracts from PBS-treated (Ctrl) and DT-treated IM^{DTR} mice at day 4 post-treatment. (**F**) Representative confocal microscopy images of CD68$^+$ mononuclear phagocytes and Tgfβ1$^+$Erg$^+$ Endo in lungs of DT-treated IM^{DTR} mice at day 4 post-DT. (**G**) Percentages of CD68$^+$ mononuclear phagocytes - Tgfβ1$^+$Erg$^+$ Endo pairs according to the distance separating the 2 cell types in lungs from PBS-treated (control) or DT-treated IM^{DTR} mice at day 4 post-DT. (**H**) Experimental outline for (I-O). (**I**) *Tgfb1* expression (left) and percentage of Tgfβ1$^+$ cells (middle) in Endo, and levels of latent Tgfβ1 in lung extracts from chimeric *Cdh5^{CreERT2} Tgfb1$^{fl/fl}$* mice or *Tgfb1$^{fl/fl}$* controls, as in (H). (**J**) Experimental outline for (K, L). (**K**) Representative histograms and (**L**) bar graph showing MFI of MafB, C1qa, Cx3cr1 and Tmem119 expression in BM Mo, as in (J). (**M**) Numbers (left) and percentages (right) of CD45.1 donor IMs from chimeric *Cdh5^{CreERT2} Tgfb1$^{fl/fl}$* mice or *Tgfb1$^{fl/fl}$* controls. (**N**) Representative histograms and (**O**) bar graph showing MFI of Cx3cr1 and Tmem119 expression in IMs from chimeric *Cdh5^{CreERT2} Tgfb1$^{fl/fl}$* mice or *Tgfb1$^{fl/fl}$* controls. (B,D,E,G,I,L,M,O) Data show (B,E,G,I,L,M,O) mean +/- SEM and are representative of 3 independent experiments (n=3-7 mice), (D) mean +/- SEM are pooled from 4 replicates (n=3 mice). *P* values were calculated using (B,D,L) a one-way ANOVA with Dunnett's post-hoc tests, (E,I,M,O) a two-tailed unpaired Student's *t* test or (G) a two-way ANOVA with Sidak's post-hoc tests. *, $P<0.05$; **, $P<0.01$; ****, $P<0.0001$. MFI, mean fluorescence intensity; ns, not significant.

Fig. 6. Disruption of IM-intrinsic TgfβRII signaling is associated with an immature and dysfunctional IM profile. (**A**) Experimental outline. Thorax-protected CD45.1/CD45.2 IM^{DTR} mice were lethally irradiated and reconstituted with BM cells from either CD45.2 *Tgfbr2*$^{fl/fl}$ mice (group "Donor *Tgfbr2*$^{fl/fl}$") or *Lyz2*^{Cre} *Tgfbr2*$^{fl/fl}$ mice (group "Donor *Lyz2*^{Cre} *Tgfbr2*$^{fl/fl}$). Chimeric mice injected 4 weeks later with DT i.p. and analyzed at days 10, 60 and 120 after DT. (**B**) Representative CD45.1 and CD45.2 plots (left) and chimerism (right) of AMs and IMs, assessed at day 10 post-DT, as in (A). (**C**) PCA plot showing the transcriptional identity of IMs, evaluated by bulk RNA-seq at day 10 post-DT, as in (A). *n*= 4 replicates per group, each replicate representing a pool of IMs sorted from 3 mice in 2 independent sorting experiments. (**D**) Unsupervised hierarchical clustering of IMs, as in (C). (**E**) Volcano plot of the differentially expressed (DE) genes between *Tgfbr2*-sufficient and *Tgfbr2*-deficient IMs, as in (C). (**F**) Bar graphs showing expression of genes between *Tgfbr2*-sufficient and *Tgfbr2*-deficient IMs, as in (C). (**G**) GSEA analyses of *Tgfbr2*-sufficient and *Tgfbr2*-deficient IMs, as in (C). The Normalized Enrichment Score (NES) and, False Discovery Rate (FDR) are shown. (**H**) Global and genotype-specific UMAP plots depicting the transcriptional identity of lung $CD64^+$ Mo and IMs isolated from donor *Tgfbr2*$^{fl/fl}$ and donor *Lyz2*^{Cre} *Tgfbr2*$^{fl/fl}$ chimeric IM^{DTR} mice at day 60 post-DT, as in (A) (n=5 pooled mice per group). (**I**) Frequency of each cell cluster from donor *Tgfbr2*$^{fl/fl}$ and donor *Lyz2*^{Cre} *Tgfbr2*$^{fl/fl}$ chimeric IM^{DTR} mice. (**J**) Dot plots showing average expression of the indicated genes and the percentages of cells expressing the genes within each cluster. (**K**) Volcano plot depicting DE genes between the monocyte cluster from donor *Tgfbr2*$^{fl/fl}$ and donor *Lyz2*^{Cre} *Tgfbr2*$^{fl/fl}$ chimeric IM^{DTR} mice. (**L**) Dot plot showing Gene Ontology (GO) enrichment results comparing $CD64^+Ly6C^+$ monocyte coming from donor *Tgfbr2*$^{fl/fl}$ and donor *Lyz2*^{Cre} *Tgfbr2*$^{fl/fl}$ chimeric IM^{DTR} mice. (B,F) Data show mean +/- SEM and (B) are representative of 2 independent experiments (n=5 mice/group); (F) represent 4 biological replicates of FACS-sorted cells. *P* values were calculated using (B) a two-way ANOVA with Tukey's post-hoc tests or (E,F,K) a Wilcoxon rank sum test. (E,K) Significantly expressed genes were defined by $\log_2FC > 0.5$ and adjusted *P* value < 0.05. *, $P<0.05$; ****, $P<0.0001$. MFI, mean fluorescence intensity; ns, not significant.

Fig. 7. Tgfβ receptor signaling in monocytes and IMs regulates niche occupancy and interactions with lung structural cells. (**A**) Bar graphs showing the proportion of monocytes and IM subsets within donor CD45.1$^-$CD45.2$^+$ cells, as in (Fig. 6A). (**B**) Bar graphs showing the cell numbers of CD45.1$^-$CD45.2$^+$ monocytes in the 4 anatomical area, peribronchial space, perivascular space, adventitial cuff and alveolar space, as in (Fig. 6A). (**C**) Representative imaging showing adventitial cuffs in donor *Tgfbr2$^{fl/fl}$* and donor *Lyz2^{Cre} Tgfbr2$^{fl/fl}$* chimeric IM^{DTR} mice lung with presence of CD45.1$^-$CD45.2$^+$ monocytes and IMs, as in (Fig. 6A). (**D**) The interaction score of CD45.1$^-$CD45.2$^+$ monocyte or IM with indicated cell in donor *Tgfbr2$^{fl/fl}$* and donor *Lyz2^{Cre} Tgfbr2$^{fl/fl}$* chimeric IM^{DTR} mice lung, as in (Fig. 6A). (**E**) The proximity between CD45.1$^-$CD45.2$^+$ monocyte and Tgfβ$^+$ CD31$^+$cells in donor *Lyz2^{Cre} Tgfbr2$^{fl/fl}$* chimeric IM^{DTR} mice lung, as in (Fig. 6A). (**F**) Violin plots showing the shortest distance between CD45.1$^-$CD45.2$^+$ monocyte with Tgfβ$^+$ CD31$^+$cells or Tgfβ$^-$ CD31$^+$cells in donor *Tgfbr2$^{fl/fl}$* and donor *Lyz2^{Cre} Tgfbr2$^{fl/fl}$* chimeric IM^{DTR} mice lung, as in (Fig. 6A). (B,F) Data show mean +/- SEM. *P* values were calculated using a Wilcoxon rank sum test. *, *P*<0.05; ****, *P*<0.0001. ns, not significant. Scale bars: (C) 50 µm; (E) 10 µm.

Fig. 8. IM-intrinsic *Tgfbr2* deficiency triggers age-related lung functional, structural and immune abnormalities. (**A**) Invasive measurements of inspiratory capacity, lung compliance and lung elastance in donor *Tgfbr2*$^{fl/fl}$ or donor *Lyz2*^{Cre} *Tgfbr2*$^{fl/fl}$ chimeric IM^{DTR} mice at day 120 after DT, as in Fig. 6A, and in 2-month-old or 18-month-old C57BL/6 WT mice. (**B**) Representative Hematoxylin & Eosin stainings of lung sections of chimeric IM^{DTR}, as in (A). (**C**) Alveolar dilatation assessed through measurements of alveolar MLI in lungs of chimeric IM^{DTR}, as in (B). (**D**) Quantification of perivascular leukocyte infiltration in lungs of chimeric IM^{DTR}, as in (B). (**E**) Representative confocal microscopy pictures of lung sections of chimeric IM^{DTR}, as in (B). Pictures are representative of one of 6 mice, each giving similar results. (**F**) Heatmap depicting the relative abundance of the indicated proteins in lung extracts from chimeric IM^{DTR} mice at day 120 post-DT, as in (A). (**G-I**) Levels of (G) IL-10, (H) elastin and (I) soluble collagen in lung extracts from chimeric IM^{DTR} mice, as in (A). (A,C,D,G,H,I) Data show mean +/- SEM, (A,C,D) are representative of 2 independent experiments (n=5-7 mice/group) or (G,H,I) are pooled from 2 independent experiments (n=11-12 mice/group). (F) Data represent biological replicates of FACS-sorted cells. (A,C,D,G,H,I) *P* values were calculated using a two-tailed unpaired Student's *t* test. *, $P<0.05$; ***, $P<0.001$; **, $P<0.01$; ****, $P<0.0001$. MLI, mean linear intercept; MFI, mean fluorescence intensity.

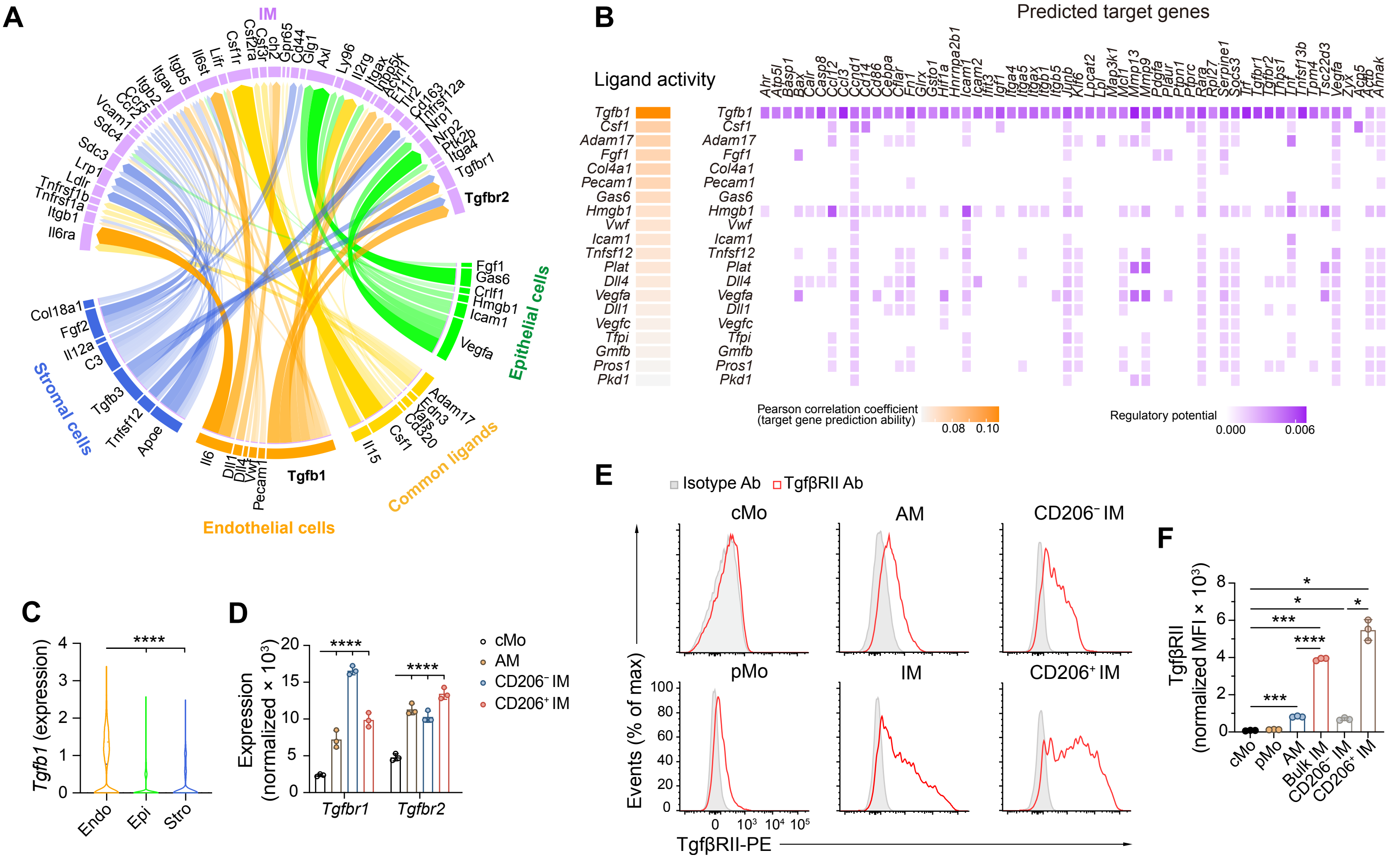
A
IM
Csf1r
Csf2ra
Csf3r
Gpr65
Cd44
Glg1
Axl
Ly96
Il2rg
Itgax
Inpp5k
Acvrl1
F11r
Tlr2
Cd163
Tnfrsf12a
Nrp1
Nrp2
Ptk2b
Itga4
Tgfbr1
Tgfbr2
Lifr
Il6st
Itgb5
Itgav
Itgb2
Ccr5
Ccr2
Vcam1
Sdc4
Sdc3
Lrp1
Ldlr
Tnfrsf1b
Tnfrsf1a
Itgb1
Il6ra
Fgf1
Gas6
Crlf1
Hmgb1
Icam1
Vegfa
Epithelial cells
Adam17
Edn3
Cd320
Csf1
Il15
Common ligands
Tgfb1
Pecam1
Vwf
Dll4
Dll1
Il6
Endothelial cells
Apoe
Tnfsf12
Tgfb3
C3
Il12a
Fgf2
Col18a1
Stromal cells
B
Ligand activity
Predicted target genes
Tgfb1
Csf1
Adam17
Fgf1
Col4a1
Pecam1
Gas6
Hmgb1
Vwf
Icam1
Tnfsf12
Plat
Dll4
Vegfa
Dll1
Vegfc
Tfpi
Gmfb
Pros1
Pkd1
Ahr
Atp5l
Basp1
Bax
Calr
Casp8
Ccl12
Ccl3
Ccnd1
Cd14
Cd86
Cebpa
Cflar
Fn1
Glrx
Gsto1
Hif1a
Hnrnpa2b1
Icam1
Icam2
Ifit3
Igf1
Itga4
Itga5
Itgax
Itgb1
Itgb5
Junb
Klf6
Lpcat2
Lpl
Map3k1
Mcl1
Mmp13
Mmp9
Pdgfa
Plaur
Ptpn1
Ptprc
Rara
Rpl27
Serpine1
Socs3
Trf
Tgfbr1
Tgfbr2
Thbs1
Tnf
Tnfsf13b
Tpm4
Tsc22d3
Vegfa
Zyx
Acp5
Actb
Ahnak
Pearson correlation coefficient (target gene prediction ability)
0.08
0.10
Regulatory potential
0.000
0.006
C
Tgfb1 (expression)
0
1
2
3
4
****
Endo
Epi
Stro
D
Expression (normalized × 10³)
0
5
10
15
20
****
****
Tgfbr1
Tgfbr2
cMo
AM
CD206⁻ IM
CD206⁺ IM
E
Isotype Ab
TgfβRII Ab
cMo
AM
CD206⁻ IM
pMo
IM
CD206⁺ IM
Events (% of max)
0
20
40
60
80
100
0
10³
10⁴
10⁵
TgfβRII-PE
F
TgfβRII (normalized MFI × 10³)
0
2
4
6
8
*
*
*
***
****
***
cMo
pMo
AM
Bulk IM
CD206⁻ IM
CD206⁺ IM

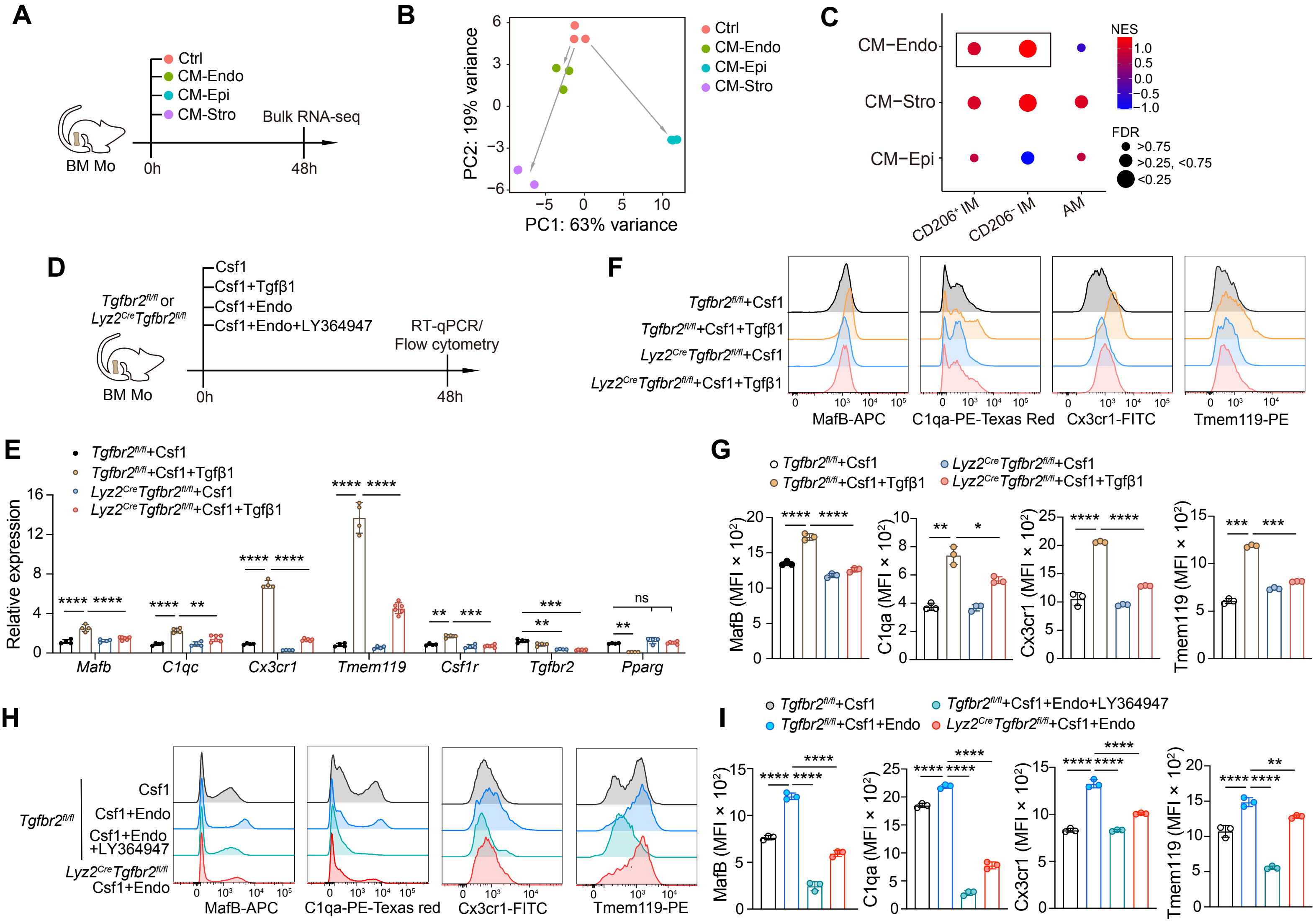
A
Ctrl
CM-Endo
CM-Epi
CM-Stro
BM Mo
0h
Bulk RNA-seq
48h
B
PC2: 19% variance
PC1: 63% variance
6
3
0
-3
-6
-5
0
5
10
Ctrl
CM-Endo
CM-Epi
CM-Stro
C
CM−Endo
CM−Stro
CM−Epi
CD206⁺ IM
CD206⁻ IM
AM
NES
1.0
0.5
0.0
−0.5
−1.0
FDR
>0.75
>0.25, <0.75
<0.25
D
Tgfbr2fl/fl or Lyz2CreTgfbr2fl/fl
BM Mo
Csf1
Csf1+Tgfβ1
Csf1+Endo
Csf1+Endo+LY364947
RT-qPCR/ Flow cytometry
0h
48h
F
Tgfbr2fl/fl+Csf1
Tgfbr2fl/fl+Csf1+Tgfβ1
Lyz2CreTgfbr2fl/fl+Csf1
Lyz2CreTgfbr2fl/fl+Csf1+Tgfβ1
MafB-APC
C1qa-PE-Texas Red
Cx3cr1-FITC
Tmem119-PE
E
Tgfbr2fl/fl+Csf1
Tgfbr2fl/fl+Csf1+Tgfβ1
Lyz2CreTgfbr2fl/fl+Csf1
Lyz2CreTgfbr2fl/fl+Csf1+Tgfβ1
Relative expression
16
12
8
4
0
Mafb
C1qc
Cx3cr1
Tmem119
Csf1r
Tgfbr2
Pparg
ns
G
Tgfbr2fl/fl+Csf1
Tgfbr2fl/fl+Csf1+Tgfβ1
Lyz2CreTgfbr2fl/fl+Csf1
Lyz2CreTgfbr2fl/fl+Csf1+Tgfβ1
MafB (MFI × 10²)
C1qa (MFI × 10²)
Cx3cr1 (MFI × 10²)
Tmem119 (MFI × 10²)
H
Tgfbr2fl/fl
Csf1
Csf1+Endo
Csf1+Endo +LY364947
Lyz2CreTgfbr2fl/fl Csf1+Endo
MafB-APC
C1qa-PE-Texas red
Cx3cr1-FITC
Tmem119-PE
I
Tgfbr2fl/fl+Csf1
Tgfbr2fl/fl+Csf1+Endo
Tgfbr2fl/fl+Csf1+Endo+LY364947
Lyz2CreTgfbr2fl/fl+Csf1+Endo
MafB (MFI × 10²)
C1qa (MFI × 10²)
Cx3cr1 (MFI × 10²)
Tmem119 (MFI × 10²)

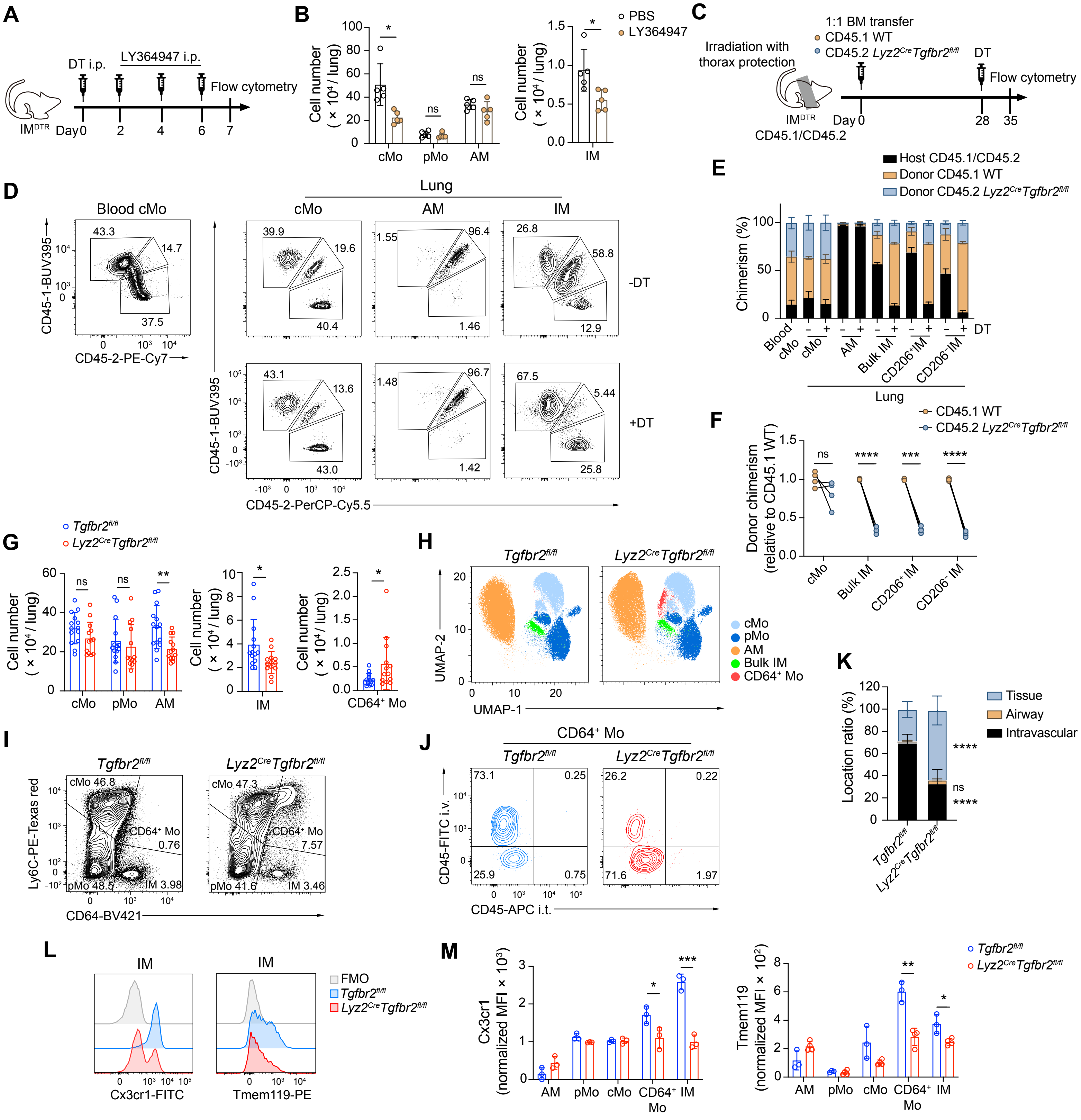
A
DT i.p.
LY364947 i.p.
Flow cytometry
IMDTR Day 0 2 4 6 7
B
* ns ns *
○ PBS
○ LY364947
Cell number (× 10⁴ / lung)
cMo pMo AM
IM
C
Irradiation with thorax protection
1:1 BM transfer
CD45.1 WT
CD45.2 Lyz2Cre Tgfbr2fl/fl
DT
Flow cytometry
IMDTR CD45.1/CD45.2
Day 0 28 35
D
Lung
Blood cMo
cMo AM IM
43.3 14.7 37.5
39.9 19.6 40.4
1.55 96.4 1.46
26.8 58.8 12.9
-DT
43.1 13.6 43.0
1.48 96.7 1.42
67.5 5.44 25.8
+DT
CD45-1-BUV395
CD45-2-PE-Cy7
CD45-2-PerCP-Cy5.5
E
Host CD45.1/CD45.2
Donor CD45.1 WT
Donor CD45.2 Lyz2Cre Tgfbr2fl/fl
Chimerism (%)
Blood cMo
cMo AM Bulk IM CD206+ IM CD206− IM
DT − +
Lung
F
CD45.1 WT
CD45.2 Lyz2Cre Tgfbr2fl/fl
Donor chimerism (relative to CD45.1 WT)
ns **** *** ****
cMo Bulk IM CD206+ IM CD206− IM
G
○ Tgfbr2fl/fl
○ Lyz2Cre Tgfbr2fl/fl
Cell number (× 10⁴ / lung)
ns ns ** * *
cMo pMo AM
IM
CD64+ Mo
H
Tgfbr2fl/fl
Lyz2Cre Tgfbr2fl/fl
UMAP-2
UMAP-1
cMo
pMo
AM
Bulk IM
CD64+ Mo
I
Tgfbr2fl/fl
Lyz2Cre Tgfbr2fl/fl
cMo 46.8 CD64+ Mo 0.76 pMo 48.5 IM 3.98
cMo 47.3 CD64+ Mo 7.57 pMo 41.6 IM 3.46
Ly6C-PE-Texas red
CD64-BV421
J
CD64+ Mo
Tgfbr2fl/fl
Lyz2Cre Tgfbr2fl/fl
73.1 0.25 25.9 0.75
26.2 0.22 71.6 1.97
CD45-FITC i.v.
CD45-APC i.t.
K
Location ratio (%)
Tissue
Airway
Intravascular
****
ns
****
Tgfbr2fl/fl
Lyz2Cre Tgfbr2fl/fl
L
IM
IM
FMO
Tgfbr2fl/fl
Lyz2Cre Tgfbr2fl/fl
Cx3cr1-FITC
Tmem119-PE
M
Cx3cr1 (normalized MFI × 10³)
* ***
AM pMo cMo CD64+ Mo IM
Tmem119 (normalized MFI × 10²)
** *
AM pMo cMo CD64+ Mo IM
○ Tgfbr2fl/fl
○ Lyz2Cre Tgfbr2fl/fl

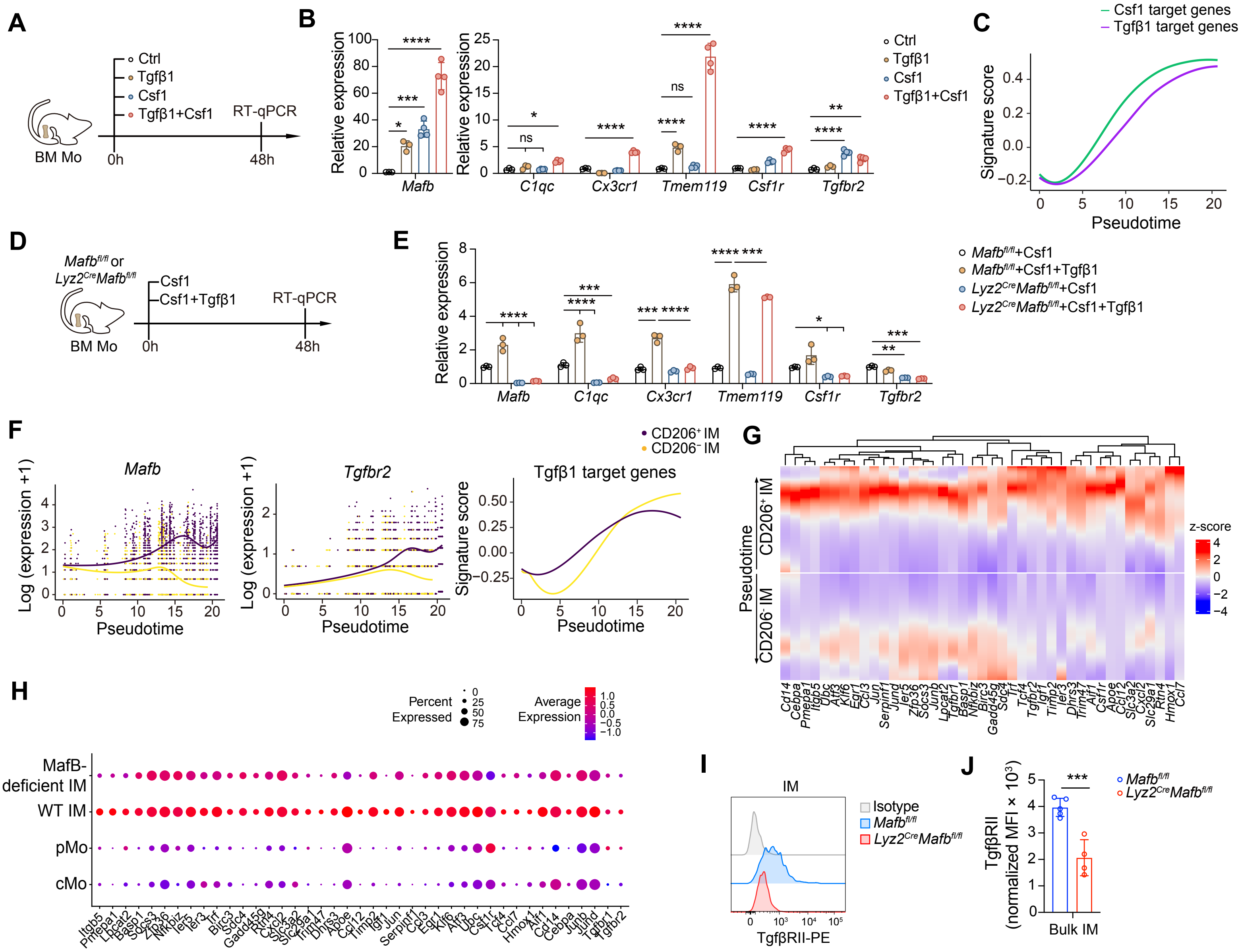
A
Ctrl
Tgfβ1
Csf1
Tgfβ1+Csf1
RT-qPCR
BM Mo
0h
48h
B
Relative expression
Mafb
C1qc
Cx3cr1
Tmem119
Csf1r
Tgfbr2
ns
Ctrl
Tgfβ1
Csf1
Tgfβ1+Csf1
C
Csf1 target genes
Tgfβ1 target genes
Signature score
Pseudotime
D
Mafb^fl/fl or Lyz2^Cre Mafb^fl/fl
Csf1
Csf1+Tgfβ1
RT-qPCR
BM Mo
0h
48h
E
Relative expression
Mafb
C1qc
Cx3cr1
Tmem119
Csf1r
Tgfbr2
Mafb^fl/fl+Csf1
Mafb^fl/fl+Csf1+Tgfβ1
Lyz2^Cre Mafb^fl/fl+Csf1
Lyz2^Cre Mafb^fl/fl+Csf1+Tgfβ1
F
CD206⁺ IM
CD206⁻ IM
Mafb
Tgfbr2
Tgfβ1 target genes
Log (expression +1)
Signature score
Pseudotime
G
z-score
Pseudotime
CD206⁺ IM
CD206⁻ IM
Cd14 Cebpa Pmepa1 Itgb5 Ubc Atf3 Klf6 Egr1 Ccl3 Jun Serpinf1 Jund Zfp36 Socs3 Junb Lpcat2 Tgfbr1 Basp1 Nfkbiz Birc3 Gadd45g Sdc4 Trf Tcf4 Tgfbr2 Igf1 Timp2 Ier3 Dhrs3 Trim47 Aif1 Csf1r Apoe Ccl12 Slc3a2 Cxcl2 Slc29a1 Rtn4 Hmox1 Ccl7
H
Percent Expressed
0
25
50
75
Average Expression
1.0
0.5
0.0
−0.5
−1.0
MafB-deficient IM
WT IM
pMo
cMo
Itgb5 Pmepa1 Lpcat2 Basp1 Socs3 Zfp36 Nfkbiz Ier5 Ier3 Trf Birc3 Sdc4 Gadd45g Rtn4 Cxcl2 Slc3a2 Slc29a1 Trim47 Dhrs3 Apoe Ccl12 Timp2 Igf1 Jun Serpinf1 Ccl3 Egr1 Klf6 Atf3 Ubc Csf1r Tcf4 Ccl7 Hmox1 Aif1 Cd14 Cebpa Junb Jund Tgfbr1 Tgfbr2
I
IM
Isotype
Mafb^fl/fl
Lyz2^Cre Mafb^fl/fl
TgfβRII-PE
J
TgfβRII (normalized MFI × 10³)
Bulk IM
Mafb^fl/fl
Lyz2^Cre Mafb^fl/fl

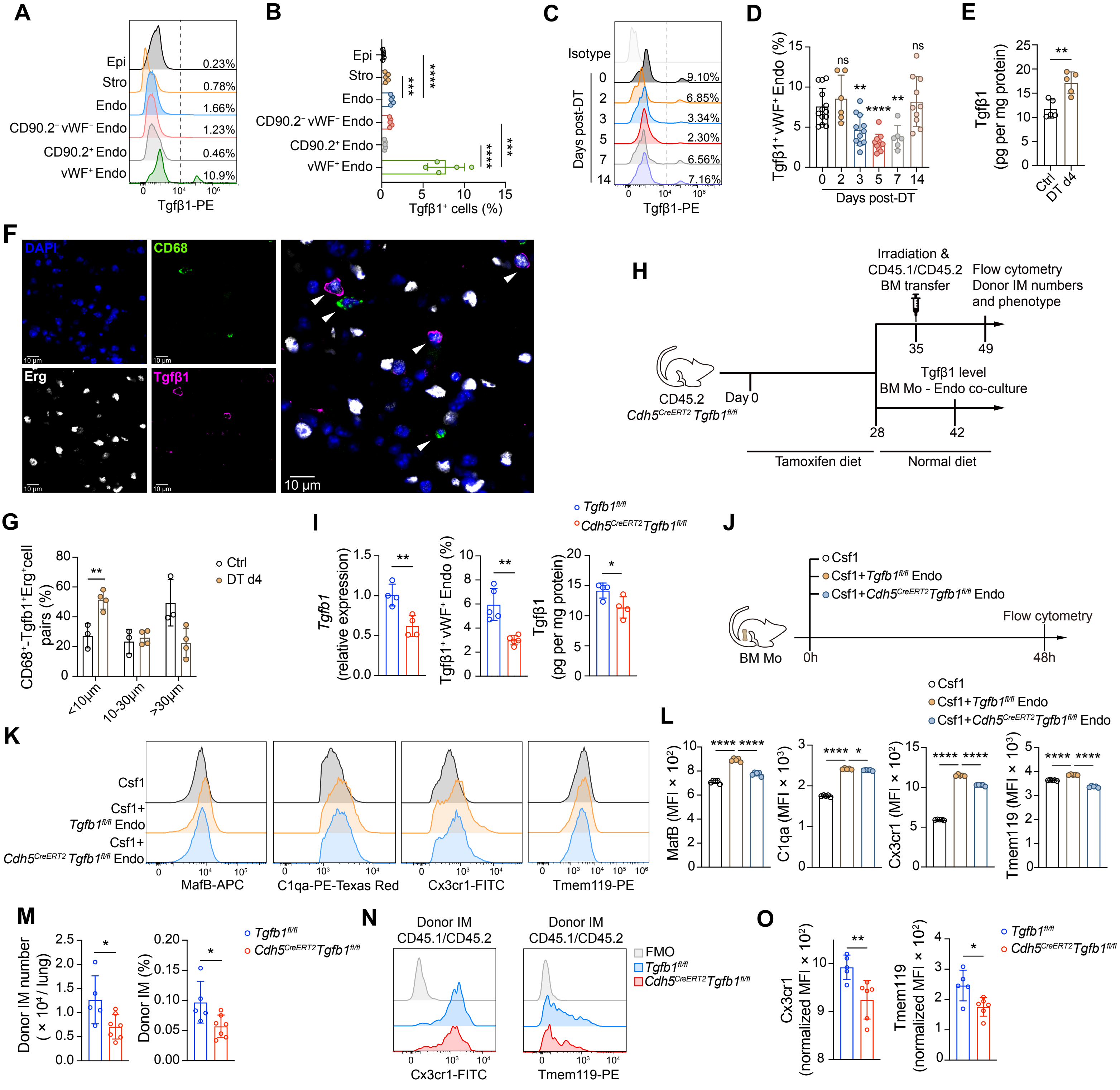
A
Epi
Stro
Endo
CD90.2⁻ vWF⁻ Endo
CD90.2⁺ Endo
vWF⁺ Endo
0.23%
0.78%
1.66%
1.23%
0.46%
10.9%
Tgfβ1-PE
B
Epi
Stro
Endo
CD90.2⁻ vWF⁻ Endo
CD90.2⁺ Endo
vWF⁺ Endo
***
****
****
***
Tgfβ1⁺ cells (%)
C
Isotype
Days post-DT
0
2
3
5
7
14
9.10%
6.85%
3.34%
2.30%
6.56%
7.16%
Tgfβ1-PE
D
Tgfβ1⁺ vWF⁺ Endo (%)
ns
**
****
**
ns
Days post-DT
E
Tgfβ1 (pg per mg protein)
**
Ctrl
DT d4
F
DAPI
CD68
Erg
Tgfβ1
10 μm
G
CD68⁺-Tgfb1⁺Erg⁺cell pairs (%)
**
Ctrl
DT d4
<10μm
10-30μm
>30μm
H
Irradiation & CD45.1/CD45.2 BM transfer
Flow cytometry Donor IM numbers and phenotype
35
49
Tgfβ1 level BM Mo - Endo co-culture
CD45.2
Cdh5^CreERT2 Tgfb1^fl/fl
Day 0
28
42
Tamoxifen diet
Normal diet
I
Tgfb1^fl/fl
Cdh5^CreERT2 Tgfb1^fl/fl
Tgfb1 (relative expression)
**
Tgfβ1⁺ vWF⁺ Endo (%)
**
Tgfβ1 (pg per mg protein)
*
J
Csf1
Csf1+Tgfb1^fl/fl Endo
Csf1+Cdh5^CreERT2 Tgfb1^fl/fl Endo
Flow cytometry
BM Mo
0h
48h
K
Csf1
Csf1+ Tgfb1^fl/fl Endo
Csf1+ Cdh5^CreERT2 Tgfb1^fl/fl Endo
MafB-APC
C1qa-PE-Texas Red
Cx3cr1-FITC
Tmem119-PE
L
Csf1
Csf1+Tgfb1^fl/fl Endo
Csf1+Cdh5^CreERT2 Tgfb1^fl/fl Endo
MafB (MFI × 10²)
C1qa (MFI × 10³)
Cx3cr1 (MFI × 10²)
Tmem119 (MFI × 10³)
**** ****
**** *
**** ****
**** ****
M
Donor IM number (× 10⁴ / lung)
*
Donor IM (%)
*
Tgfb1^fl/fl
Cdh5^CreERT2 Tgfb1^fl/fl
N
Donor IM CD45.1/CD45.2
FMO
Tgfb1^fl/fl
Cdh5^CreERT2 Tgfb1^fl/fl
Cx3cr1-FITC
Tmem119-PE
O
Cx3cr1 (normalized MFI × 10²)
**
Tmem119 (normalized MFI × 10²)
*
Tgfb1^fl/fl
Cdh5^CreERT2 Tgfb1^fl/fl

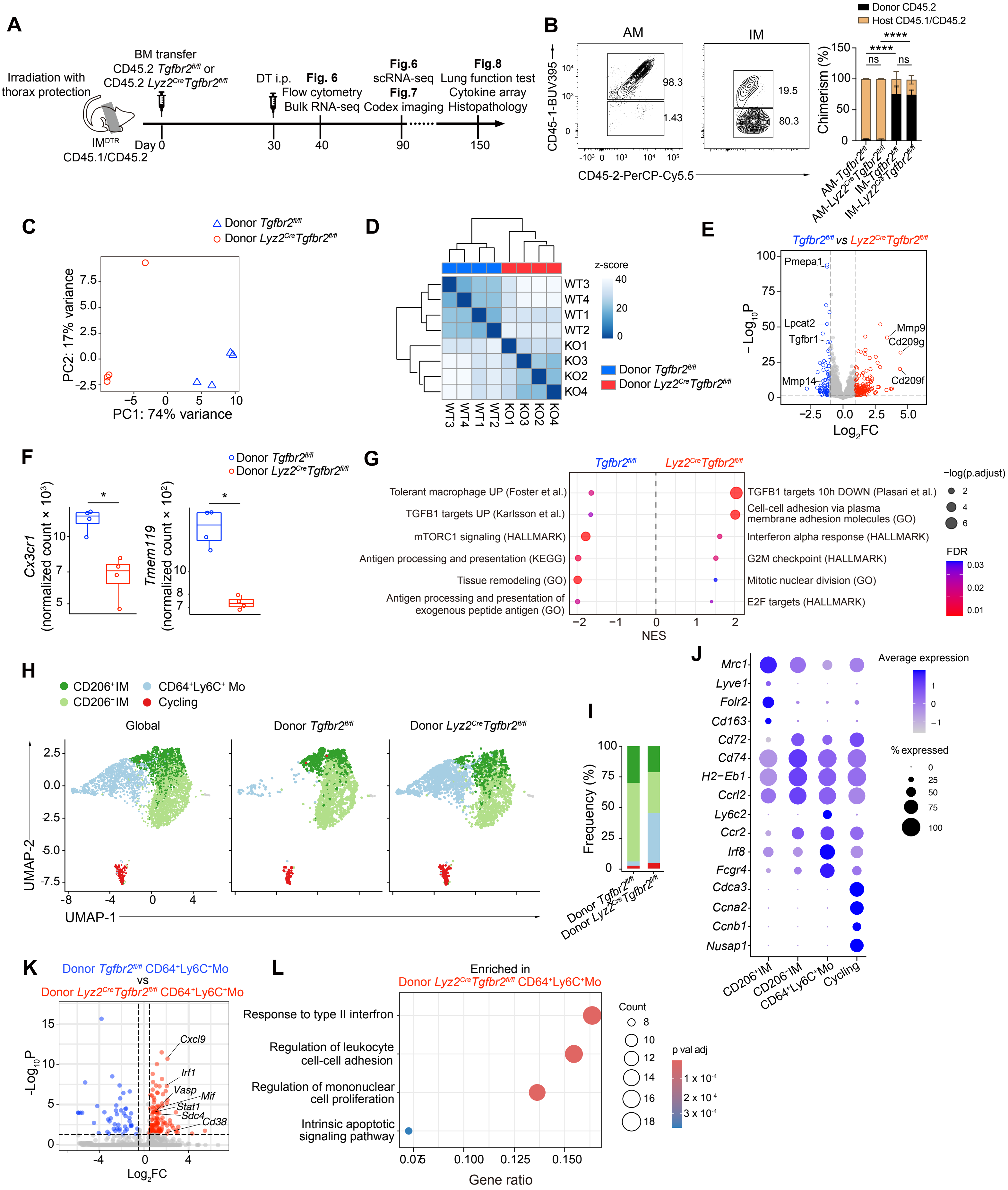
A
Irradiation with thorax protection
IMDTR
CD45.1/CD45.2
BM transfer
CD45.2 Tgfbr2fl/fl or
CD45.2 Lyz2CreTgfbr2fl/fl
Day 0
DT i.p.
30
Fig. 6
Flow cytometry
Bulk RNA-seq
40
Fig.6
scRNA-seq
Fig.7
Codex imaging
90
Fig.8
Lung function test
Cytokine array
Histopathology
150
B
AM
IM
CD45-1-BUV395
CD45-2-PerCP-Cy5.5
98.3
1.43
19.5
80.3
Donor CD45.2
Host CD45.1/CD45.2
Chimerism (%)
ns
ns
****
****
AM-Tgfbr2fl/fl
AM-Lyz2CreTgfbr2fl/fl
IM-Tgfbr2fl/fl
IM-Lyz2CreTgfbr2fl/fl
C
Donor Tgfbr2fl/fl
Donor Lyz2CreTgfbr2fl/fl
PC2: 17% variance
PC1: 74% variance
D
z-score
40
20
0
WT3
WT4
WT1
WT2
KO1
KO3
KO2
KO4
Donor Tgfbr2fl/fl
Donor Lyz2CreTgfbr2fl/fl
E
Tgfbr2fl/fl vs Lyz2CreTgfbr2fl/fl
Pmepa1
Lpcat2
Tgfbr1
Mmp14
Mmp9
Cd209g
Cd209f
– Log10P
Log2FC
F
Donor Tgfbr2fl/fl
Donor Lyz2CreTgfbr2fl/fl
Cx3cr1
(normalized count × 10³)
Tmem119
(normalized count × 10²)
*
*
G
Tgfbr2fl/fl
Lyz2CreTgfbr2fl/fl
Tolerant macrophage UP (Foster et al.)
TGFB1 targets UP (Karlsson et al.)
mTORC1 signaling (HALLMARK)
Antigen processing and presentation (KEGG)
Tissue remodeling (GO)
Antigen processing and presentation of exogenous peptide antigen (GO)
TGFB1 targets 10h DOWN (Plasari et al.)
Cell-cell adhesion via plasma membrane adhesion molecules (GO)
Interferon alpha response (HALLMARK)
G2M checkpoint (HALLMARK)
Mitotic nuclear division (GO)
E2F targets (HALLMARK)
NES
−log(p.adjust)
FDR
H
CD206+IM
CD206−IM
CD64+Ly6C+ Mo
Cycling
Global
Donor Tgfbr2fl/fl
Donor Lyz2CreTgfbr2fl/fl
UMAP-2
UMAP-1
I
Frequency (%)
Donor Tgfbr2fl/fl
Donor Lyz2CreTgfbr2fl/fl
J
Mrc1
Lyve1
Folr2
Cd163
Cd72
Cd74
H2−Eb1
Ccrl2
Ly6c2
Ccr2
Irf8
Fcgr4
Cdca3
Ccna2
Ccnb1
Nusap1
CD206+IM
CD206−IM
CD64+Ly6C+Mo
Cycling
Average expression
% expressed
K
Donor Tgfbr2fl/fl CD64+Ly6C+Mo
vs
Donor Lyz2CreTgfbr2fl/fl CD64+Ly6C+Mo
Cxcl9
Irf1
Vasp
Mif
Stat1
Sdc4
Cd38
-Log10P
Log2FC
L
Enriched in
Donor Lyz2CreTgfbr2fl/fl CD64+Ly6C+Mo
Response to type II interfron
Regulation of leukocyte cell-cell adhesion
Regulation of mononuclear cell proliferation
Intrinsic apoptotic signaling pathway
Gene ratio
Count
p val adj

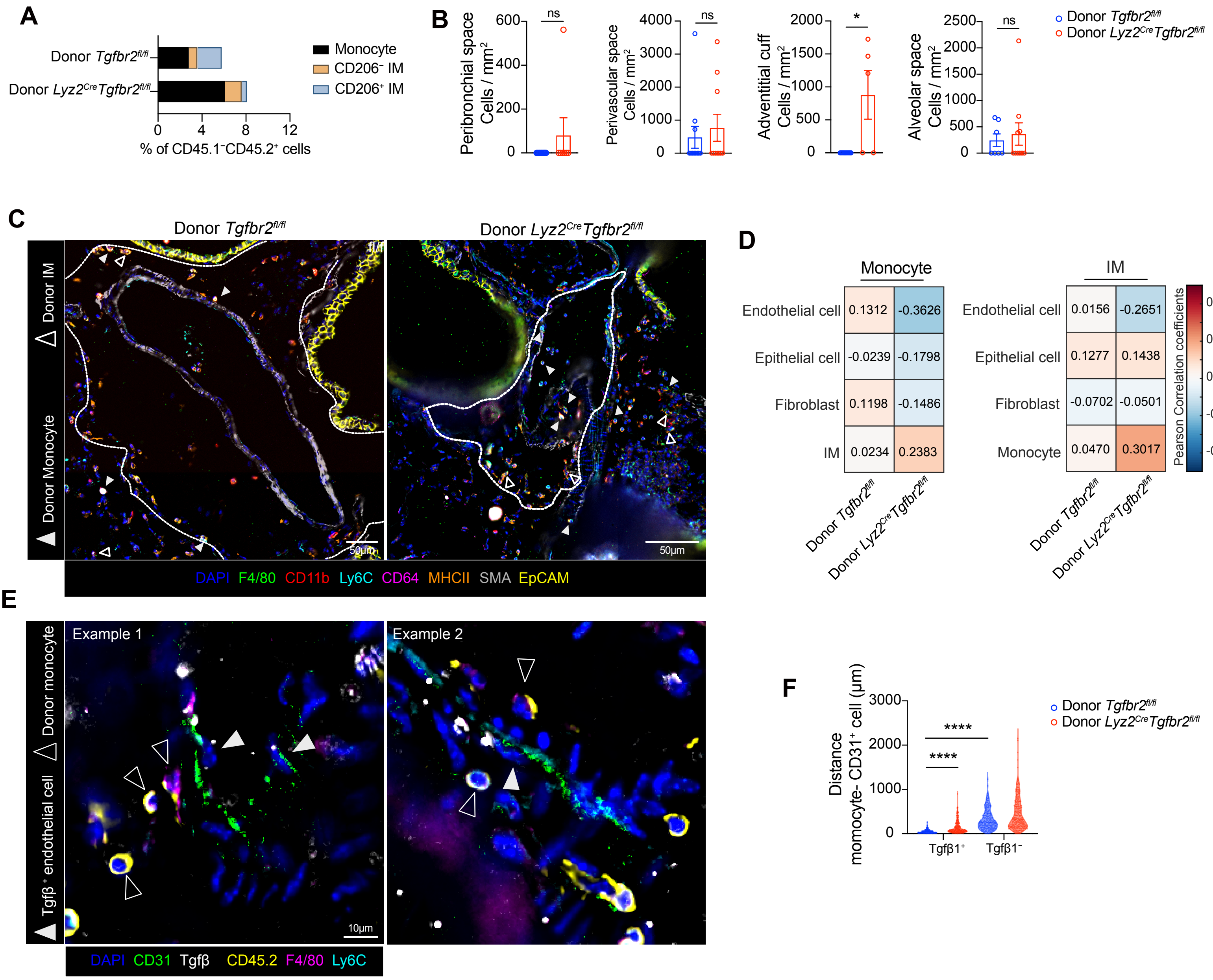
A
Donor Tgfbr2fl/fl
Donor Lyz2CreTgfbr2fl/fl
Monocyte
CD206⁻ IM
CD206⁺ IM
0
4
8
12
% of CD45.1⁻CD45.2⁺ cells
B
Peribronchial space Cells / mm²
600
400
200
0
ns
Perivascular space Cells / mm²
4000
3000
2000
1000
0
ns
Adventitial cuff Cells / mm²
2000
1500
1000
500
0
*
Alveolar space Cells / mm²
2500
2000
1500
1000
500
0
ns
Donor Tgfbr2fl/fl
Donor Lyz2CreTgfbr2fl/fl
C
Donor Tgfbr2fl/fl
Donor Lyz2CreTgfbr2fl/fl
Donor IM
Donor Monocyte
50µm
50µm
DAPI F4/80 CD11b Ly6C CD64 MHCII SMA EpCAM
D
Monocyte
Endothelial cell 0.1312 -0.3626
Epithelial cell -0.0239 -0.1798
Fibroblast 0.1198 -0.1486
IM 0.0234 0.2383
Donor Tgfbr2fl/fl
Donor Lyz2CreTgfbr2fl/fl
IM
Endothelial cell 0.0156 -0.2651
Epithelial cell 0.1277 0.1438
Fibroblast -0.0702 -0.0501
Monocyte 0.0470 0.3017
Donor Tgfbr2fl/fl
Donor Lyz2CreTgfbr2fl/fl
Pearson Correlation coefficients
0.8
0.4
0
-0.4
-0.8
E
Example 1
Example 2
Donor monocyte
Tgfβ⁺ endothelial cell
10µm
DAPI CD31 Tgfβ CD45.2 F4/80 Ly6C
F
Distance momocyte- CD31⁺ cell (µm)
3000
2000
1000
0
****
****
Tgfβ1⁺
Tgfβ1⁻
Donor Tgfbr2fl/fl
Donor Lyz2CreTgfbr2fl/fl

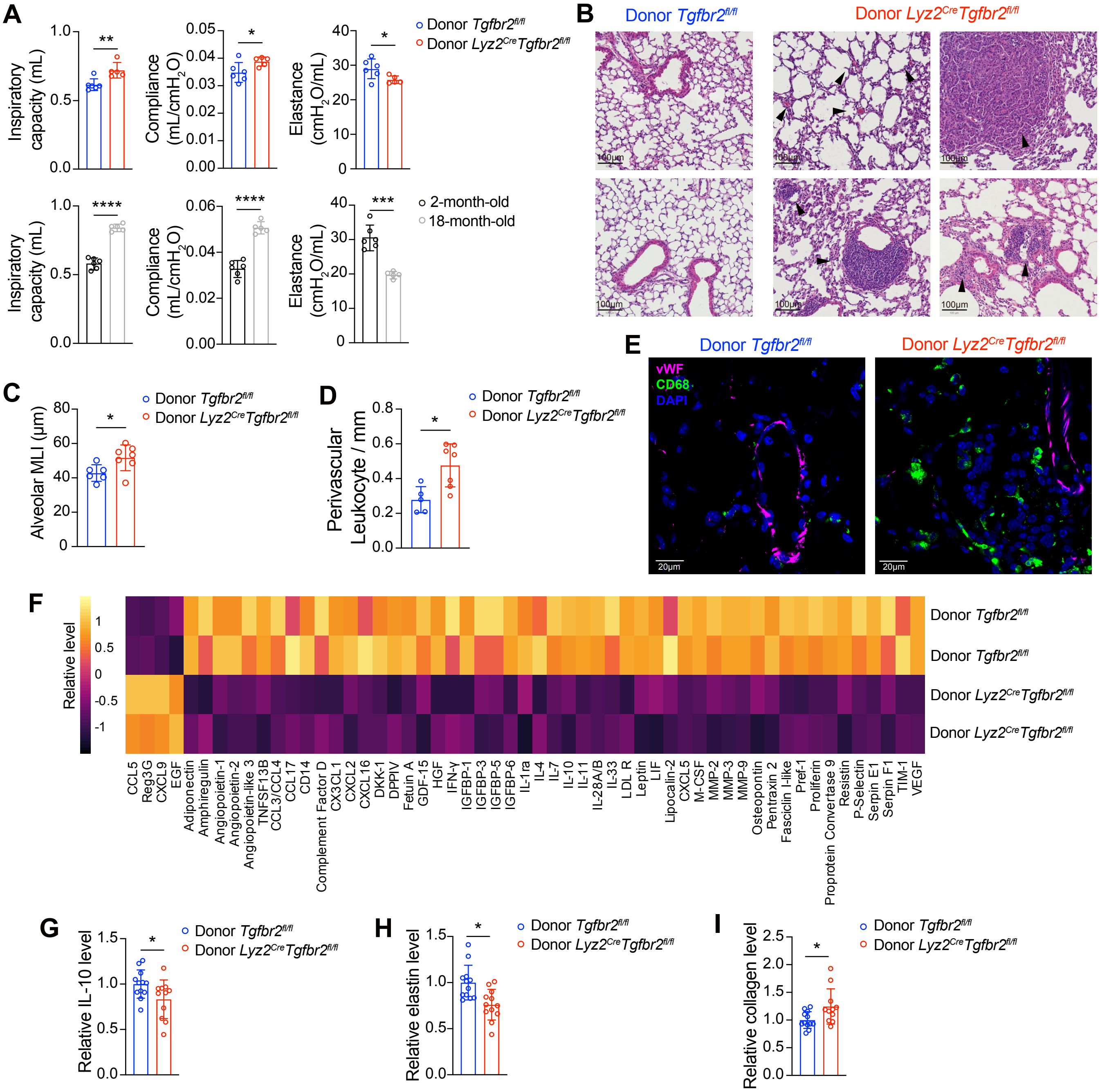
A
Inspiratory capacity (mL)
1.0
0.5
0.0
**
Compliance (mL/cmH2O)
0.05
0.04
0.03
0.02
0.01
0.00
*
Elastance (cmH2O/mL)
40
30
20
10
0
*
Donor Tgfbr2fl/fl
Donor Lyz2CreTgfbr2fl/fl
Inspiratory capacity (mL)
****
Compliance (mL/cmH2O)
0.06
0.04
0.02
0.00
****
Elastance (cmH2O/mL)
***
2-month-old
18-month-old
B
Donor Tgfbr2fl/fl
Donor Lyz2CreTgfbr2fl/fl
100μm
C
Alveolar MLI (μm)
80
60
40
20
0
*
Donor Tgfbr2fl/fl
Donor Lyz2CreTgfbr2fl/fl
D
Perivascular Leukocyte / mm
0.8
0.6
0.4
0.2
0.0
*
Donor Tgfbr2fl/fl
Donor Lyz2CreTgfbr2fl/fl
E
Donor Tgfbr2fl/fl
Donor Lyz2CreTgfbr2fl/fl
vWF
CD68
DAPI
20μm
F
Relative level
1
0.5
0
-0.5
-1
Donor Tgfbr2fl/fl
Donor Tgfbr2fl/fl
Donor Lyz2CreTgfbr2fl/fl
Donor Lyz2CreTgfbr2fl/fl
CCL5
Reg3G
CXCL9
EGF
Adiponectin
Amphiregulin
Angiopoietin-1
Angiopoietin-2
Angiopoietin-like 3
TNFSF13B
CCL3/CCL4
CCL17
CD14
Complement Factor D
CX3CL1
CXCL2
CXCL16
DKK-1
DPPIV
Fetuin A
GDF-15
HGF
IFN-γ
IGFBP-1
IGFBP-3
IGFBP-5
IGFBP-6
IL-1ra
IL-4
IL-7
IL-10
IL-11
IL-28A/B
IL-33
LDL R
Leptin
LIF
Lipocalin-2
CXCL5
M-CSF
MMP-2
MMP-3
MMP-9
Osteopontin
Pentraxin 2
Fasciclin I-like
Pref-1
Proliferin
Proprotein Convertase 9
Resistin
P-Selectin
Serpin E1
Serpin F1
TIM-1
VEGF
G
Relative IL-10 level
1.5
1.0
0.5
0.0
*
Donor Tgfbr2fl/fl
Donor Lyz2CreTgfbr2fl/fl
H
Relative elastin level
1.5
1.0
0.5
0.0
*
Donor Tgfbr2fl/fl
Donor Lyz2CreTgfbr2fl/fl
I
Relative collagen level
2.5
2.0
1.5
1.0
0.5
0.0
*
Donor Tgfbr2fl/fl
Donor Lyz2CreTgfbr2fl/fl

Supplementary Materials for

Endothelial-driven TGFβ signaling supports lung interstitial macrophage development from monocytes.

W. Peng[1,2], D. Vanneste[1,2], D. Bejarano[3], J. Abinet[1,2], M. Meunier[1,2], C. Radermecker[1,2], F. Perin[4], D. Cataldo[4], F. Bureau[2,5], A. Schlitzer[3], Q. Bai[1,6,*] & T. Marichal[1,2,7,*]

Corresponding authors: t.marichal@uliege.be; qiang.bai@inserm.fr

The PDF file includes:

Materials and methods

Bone marrow, blood and tissue single-cell suspension preparation

Blood was collected via retro-orbital plexus bleeding from terminally anesthetized mice. For BM cell collection, mice were sacrificed via cervical dislocation, femurs and tibias were dissected and cleaned of soft tissue. Distal and proximal ends were opened to flush out BM cells. After centrifugation, cell pellets were resuspended in ice-cold PBS (Thermo Fisher, 14190094) containing 10 mM EDTA (Merck Millipore, 1084181000), and single-cell suspension were filtered using a 70 µm cell strainer (Corning, 352350). To isolate lung leukocytes, lungs were finely minced with razor blades and digested for 1 h at 37 °C in digestion medium No.1, consisting of 5% vol/vol FBS (Thermo Fisher, 10270098), 1 mg/mL collagenase A (Sigma, 14190094) and 0.05 mg/mL DNase I (Sigma, 11284932001) in HBSS (Lonza, BE10-508F). After 45 min of digestion, the suspension was passed through an 18-gauge needle to dissociate cell aggregates. Ice-cold PBS (Thermo Fisher, 14190094) with 10 mM EDTA (Merck Millipore, 1084181000) was added to stop the digestion, and cell suspensions were filtered using a 70 µm cell strainer (Corning, 352350). Mononuclear leukocytes from lungs were enriched using a Percoll density gradient (GE Healthcare, 17089101), with cells collected from the 1.080:1.038 g/mL interface. For heart single-cell suspensions, the same digestion procedure was used as described for lung leukocytes, but without applying a Percoll gradient. Ear single-cell suspensions were prepared by harvesting the ears from the base, splitting them into dorsal and ventral layers, and placing them in HBSS containing 5 U/mL Dispase (Sigma, D4693) for 90 min at 37 °C. Ear tissues were cut into small pieces using razor blades and further digested for 1 h at 37°C in digestion medium No.1, following the same procedure as for lung leukocytes but without applying a Percoll gradient.

To isolate lung structural cells, mice were administrated i.t with 1 mL digestion medium No.2 (1 U/mL Dispase (Merck Millipore, D4693), 4 U/mL Elastase (Merck Millipore, E1250) and 0.05 mg/mL DNase 1 in HBSS) for 1 min. The entire lung with the trachea was harvested and digested for 30 min at 37 °C in 1 ml digestion medium No.2. Subsequently, the lungs were minced into small pieces using razor blades and further digested as described above with digestion medium No.1 (HBSS containing 5% vol/vol FBS, 1 mg/mL collagenase A, and 0.05 mg/mL DNase I) for 30 mins at 37°C to obtain a single-cell suspension.

Immunofluorescence

For lung immunofluorescence staining, lungs were perfused with 10 mL PBS via the left ventricle and collected. Lungs were fixed in 4% paraformaldehyde (Thermo Fisher, F/1501/PB15) at 4 °C for 24 h. Subsequently, the fixed lungs were cryoprotected in 30% sucrose (VWR, Avantor, 57-50-1) in PBS at 4 °C for 4 h. Following cryoprotection, the lungs were embedded in optimal cutting temperature compound (OCT; Tissue-Tek, 4583) and stored at -80 °C overnight. The lung OCT sections were cut into 7-µm-thick sections and blocked-in methanol 100% (Merck, 67-56-1) at -20 °C for 20 min. For staining, samples were incubated overnight at 4 °C in blocking buffer (PBS with 0.3% Triton X-100 (Merck, 648466) and 2% donkey serum (Sigma Aldrich, D9663)) containing rat anti-mouse antibodies CD68 (Bio-rad, MCA1957GA), mouse anti-mouse antibodies directed against Tgfβ1 (R&D Systems, MAB2402), rabbit anti-mouse antibodies directed against Erg (Abcams, ab92513) at a 1:100 dilution, FITC-conjugated anti-mouse antibodies against vWF (Santa Cruz, sc-365712) at a 1:75 dilution. After washing with PBS, the samples were incubated with secondary antibodies: anti-rat IgG antibodies conjugated with AF488 (ThermoFisher, A-11034), anti-mouse IgG antibodies conjugated with AF750 (ThermoFisher, A-

21037) and anti-rabbit IgG antibodies conjugated with AF647 (BioLegend, 405416) in blocking buffer at a 1:500 dilution in the dark at room temperature for 2 h. Finally, samples were washed with PBS, mounted with 10 µl ProLong Antifade reagent with DAPI (ThermoFisher, P36966) on glass slides, and stored at room temperature in the dark overnight. All samples were analyzed using spectral fluorescence microscopy. Images shown in Fig. 5F were acquired on an LSM 880 inverted confocal microscope using Plan-Apochromat 40x/1.3 Oil objectives. Fluorophores were excited simultaneously at 405/488/561/633 nm with detection wavelength at 350-499/380-548/573-627/659-735 with Airyscan in Zeiss SuperResolution mode and unidirectional acquisition. Images shown in Fig. 8E were acquired on an LSM 980 inverted confocal microscope using Plan-Apochromat 63x/1.4 Oil objectives. Fluorophores were excited simultaneously at 405/488/639 nm with detection wavelength at 350-499/380-548/659-735 with GaAsP-PMT in Zeiss FastAiryScanSheppardSum SR-4y:4.2 mode and bidirectional acquisition. Analysis was performed with Zeiss Blue software 3.6.

The cell distance analysis was performed by Imaris 9.5. The CD68$^+$ cells and Tgfβ1$^+$Erg$^+$ cells were identified by the intensity of fluorescence. The distance of Tgfβ1$^+$Erg$^+$- CD68$^+$ cells pairs was calculated the minimum surface distance from Tgfβ1$^+$Erg$^+$ cells to CD68$^+$ cells. All images in Imaris were performed in batch mode with the same algorithm.

Real-time quantitative PCR

Total RNA was extracted from the samples using TRIzol reagent (ThermoFisher, 10296010). cDNA was synthesized using with RevertAid H Minus First Strand cDNA Synthesis Kit (ThermoFisher, K1631), RT-qPCR was performed using SYBR green supermix (Bio-rad, 1725121). The cycle threshold (CT) values obtained from triplicate qPCR reactions were extracted from the QuantStudio 5 (ThemoFisher) and transferred onto spreadsheets for analysis using the relative quantification method $2^{-\Delta\Delta CT}$.The primers for the test genes are listed in Table S1.

CODEX staining

Five µm-thick slices of frozen lungs from chimeric IM^{DTR} mice (Fig. 6A) were prepared and used for CODEX staining, as described (*59*). Briefly, after drying the sections, they were fixed for 10 min in ice-cold acetone. After fixation, coverslips were transferred to hydration buffer and subsequently photobleached twice for 45 min each. Afterwards, sections were blocked and stained with a 28-plex CODEX antibody panel overnight at 4°C. Samples were washed twice with staining buffer, fixed in ice-cold methanol for 5 min, washed with 1x PBS, and fixed with BS3 fixative for 20 min (ThermoFisher, 21580). After washing off the fixative, the samples were stored at 4°C before imaging.

CODEX imaging, processing and analysis

Coverslips and reporter plate were equilibrated at room temperature for 30 min before imaging. A multicycle CODEX experiment was performed using a Zeiss Axio Observer widefield fluorescence microscope with a 20x objective (NA 0.85), and the 405, 488, 568, and 647 nm channels. A z-spacing of 1.5 µm was used for acquisition. Raw files were exported using the CODEX Instrument Manager (Akoya Biosciences) and processed with CODEX Processor v1.7 (Akoya Biosciences). Processing included background subtraction, stitching, shading, shading correction, and cell segmentation.

Images were inspected and analyzed using the CODEX MAV (Akoya Biosciences) plugin in Fiji. Regions out of focus were removed for the analysis. Cells were selected using the DAPI counterstain and subsequently classified using a similar strategy to the one used in flow cytometry. Mature IMs were defined as CD45.2^{+}CD45.1^{-}Lin^{-}CD11b^{+}SiglecF^{-}F4/80^{+}Ly6C^{-}MerTK^{+}MHCII^{+}CD206^{+}cells. Monocytes were defined as CD45.2^{+}CD45.1^{-}Lin^{-}CD11b^{+}SiglecF^{-}F4/80^{+}Ly6C$^{+/\mathrm{lo}}$CD64$^{+/\mathrm{lo}}$MerTK$^{\mathrm{lo}/-}$ cells. After cell classification, the generated .csv files were exported to CytoMAP (*60*) and cell interactions of monocytes and IMs with other immune and structural cells (Table S2) were calculated using pearson correlation.

To determine the distribution of monocytes and IMs interstitial macrophages in the major anatomical areas of the lung, images were exported to QuPath. The perivascular, peribronchial, interstitial spaces and the adventitial cuffs were manually annotated in the whole image. Afterwards cells were detected using the DAPI counterstain and multiple classifiers were established using the single stains and used to gate the same populations as above. To calculate the distances between Tgfβ^{+} or Tgfβ^{-} endothelial cells (CD45^{-}EpCAM^{-}PDGFRa^{-}CD31^{+}) and IMs and monocytes, the nearest distance between centroids was calculated.

ELISA, Collagen and Proteome Assays

Lungs of chimeric IM$^{\mathrm{DTR}}$ mice were perfused with 10 mL PBS through the right ventricle and isolated. The dissected lungs were snap frozen in liquid nitrogen and homogenized using a tissue homogenizer (IKA) in 360 µl ice-cold lysis buffer (40 mM Tris-HCl (pH 7.4), 150 mM NaCl, 10% glycerol and protease inhibitor cocktail (Sigma, 11697498001)). The samples were added 1% NP-40 (Sigma, 74385), then centrifuged for 20 min at 4 °C, and supernatants were collected after centrifugation. The protein concentration was determined by Pierce BCA Protein Assay Kit (Thermo Fisher), following to the manufacturer's instructions. The supernatants were stored at -80 °C. Tgfβ1, IL-10 and soluble collagen level were quantified in lung homogenates using Tgfβ1 Human/Mouse Uncoated ELISA Kit (Thermo Fisher, 88-8350-88), IL-10 Mouse uncoated ELISA Kit (Thermo Fisher, 88-7105-88), mouse Elastin ELISA Kit (Novusbio, NBP3-06918) and Sircol Soluble Collagen Assay Kit (Biocolor, S1000), respectively, according to the manufacturer's instructions.

For Proteome profiler assay, 200 ng total protein were tested for the presence of cytokines and chemokines using a proteome profiler mouse XL cytokine array (R&D Systems), according to manufacturer instructions. Results were visualized using an ImageQuant LAS 4000 (GE Healthcare) and analyzed using ImageJ software.

Lung function measurements

Mice were anesthetized i.p. with sodium pentobarbital (Nembutal) at a dose of 50 mg/kg. The trachea was surgically exposed via dissection of the neck region. An 18-gauge blunt metal cannula, known for its typical resistance of 0.18 cmH$_2$Os/mL, was inserted into trachea and secured using a nylon suture to ensure stability. Subsequently, the mice were connected to the flexiVent computer-controlled piston ventilator (SCIREQ) through the cannula. This connection was facilitated by the FX adaptor Y-tubing. The ventilator was set to standard parameters for murine ventilation: a positive end expiratory pressure (PEEP) at 3 cmH^{2}O, a tidal volume of 10 mL/kg, a respiratory rate of 150 breaths per minute, and a fraction of inspired oxygen of 0.21, which corresponds to room air. Respiratory mechanics were evaluated using the forced oscillation technique (FOT) and the latest version of the flexiVent operating software (flexiWare version 8.1.3).

Lung histology and histopathological measurements

Lungs were fixed in 5% formalin, paraffin-embedded, and cut into 5-µm sections that were then stained with hematoxylin and eosin (H&E) before analysis. Full lung sections images were acquired on an Axioscan 7 (Zeiss, 20×).

The size of alveoli was assessed with the method of mean linear intercept (MLI), as described (*61*, *62*). Briefly, lung tissues and alveolar walls were identified by thresholding (Huang thresholding) on hematoxylin and eosin (H&E)-stained lung images. Horizontal test lines were generated by overlaying line grids onto lung field images at 50% opacity, using image flattening to isolate measurement regions. Chord lengths were identified with color thresholding and measured with the "analyze particles" function in Fiji/ImageJ, and results were exported for statistical analyses. For each image, three zones of alveoli were randomly selected and only the cords within these regions were counted with "ROI tool".

The clusters of perivascular infiltrating leukocytes were identified in H&E-stained lung images as described (*63*, *64*). Briefly, only the leukocyte clusters larger than 50 µm in size and adjacent to the small arterioles or venules (i.e., less than 100 µm in diameter) were counted in each lung section. The count number were then normalized by the corresponding lung area, yielding normalized values expressed as foci per unit area.

Bulk RNA sequencing analyses

Lung CD45.1$^-$CD45.2$^+$Ly6G$^-$SiglecF$^-$CD11b$^+$SSC^{lo}CD64$^+$ cells (encompassing CD64$^+$ Mo and IMs) were FACS-sorted from chimeric IM^{DTR} mice (Fig. 6A) using the gating strategy shown in fig. S7A into TRIzol reagent (Thermo Fisher, 10296010). Total RNA was extracted with the standard TRIzol RNA extraction protocol. RNA quality and quantity were evaluated using a 2100 bioanalyzer (Agilent) and the Quant-iT RiboGreen RNA Assay Kit (Thermo Fisher, R11490). One hundred nanograms of RNA was used to generate the libraries using the TruSeq Stranded mRNA kit (Illumina, 20020594). These libraries were sequenced on an Illumina NovaSeq sequencer on an SP flow cell. Sequence alignment with the mouse genome (GRCm38), sequence counting and quality control were performed using the nf-core/rnaseq pipeline.

RNA-seq data were analyzed by R (version 4.3.3) using R Bioconductor (3.18) and DESeq2 package (version 1.42.1). To correct for potential batch effects, the ComBat function from the sva package (v3.50.0). Differential expression analysis was performed using the DESeq2 package (v1.42.1). Gene set enrichment analysis (GSEA) was conducted using the clusterProfiler package (v4.10.1). Molecular Signatures Database (MSigDB) gene sets were supplied by msigdbr package (v7.5.1).

Single cell RNA sequencing and analyses

Lung CD45.1$^-$CD45.2$^+$Ly6G$^-$SiglecF$^-$CD11b$^+$SSC^{lo}CD64$^+$ cells (encompassing CD64$^+$ Mo and IMs) were FACS-sorted from lung single-cell suspensions pooled from 5 chimeric IM^{DTR} mice, as for the bulk RNA-seq analysis. For each sample, an aliquot of Trypan blue-treated cells was examined under the microscope for counting, viability and aggregate assessment following FACS sorting. Viability was above 90% for all samples and no aggregates were observed. Cells from each group were then labelled with TotalSeq anti-mouse hashtags (BioLegend, TotalSeq-B0301 for donor *Tgfbr2$^{fl/fl}$* group and TotalSeq-B0303 for doner *Lyz2^{cre}Tgfbr2$^{fl/fl}$* group) before being pooled. Pooled cells were centrifuged, and pellet was resuspended in calcium- and magnesiumfree PBS containing 0.4 mg/ mL UltraPure BSA (Thermo Fisher Scientific). For library preparation, approximately 1 x 10^4 cells were loaded into the Chromium iX (10X Genomics), in which they were partitioned, their polyA RNAs captured and barcoded using Chromium Next GEM Single Cell 3′ Reagent Kits v3.1 (10X Genomics). The cDNAs were amplified and libraries compatible with Illumina sequencers were generated using Chromium Next GEM Single Cell 3′ Reagent Kits v3.1 with Feature Barcoding technology for Cell Surface Protein (10X Genomics). For Hash Tag Oligonucleotide (TotalSeq B anti-mouse Antibody, Biolegend) library, primers for cDNA amplification and index PCR are provided in Chromium Single Cell 3′ Feature Barcode Library Kit (10x Genomics). The libraries were sequenced on an Illumina NovaSeq 6000 on an S4 cell flow (read 1, 150 cy; read 2, 150 cy; index 1, 10 cy; index 2, 10 cy) at a depth of ~2,5 x 10^4 reads per cell.

The Cell Ranger (v8.0) application (10x Genomics) was then used to demultiplex the BCL files into FASTQ files (cellranger mkfastq), to perform alignment (to Cell Ranger human genome references 3.0.2 GRCm38/build 97), filtering, UMI counting and to produce gene-barcode matrices for each sample (cellranger multi).

Filtered matrix files were used for further scRNAseq analyses with R Bioconductor (3.18) and Seurat (5.1.0). Filtered matrices containing cell IDs and feature names in each sample were used to build a Seurat object. We performed a quality control by filtering out the cells with less than 200 detected genes, the genes detected in less than 3 cells and the cells exhibiting more than 10% of mitochondrial genes. Gene counts were normalized by default method "LogNormalize" with scale factor 10000 and log-transformation. Four clusters were obtained using FindClusters function (Seurat package) and characterized by expression of cell type-specific genes. For differential expression analysis, expression in each gene was compared using FindMarkers function (Seurat package) and the genes with adjusted P value < 0.05 and logFC > 0.5 were considered as significant up-regulated genes. Gene-ontology enrichment analysis and gene set enrichment analysis (GSEA) were performed using clusterProfiler package.

Analysis of published single-cell RNA sequencing data

NicheNet analysis (*21*) was applied to previously published single-cell RNA sequencing data (*10*). The cell types were defined by SingleR package. We used the ligand-receptor network included in nichenetr package to predict ligand activity. To perform the NicheNet analysis, receiver cell population were set as classical monocytes developing into IMs, whereas the sender cell population was set as endothelial cells. Only genes expressed with in at least 10% of cells in one cluster will be used to calculated ligand activity.

InAct molecular interaction database (inact-micluster) was used to construct mouse ligand-receptor network. Briefly, only *mus musculus* genes were filtered and annotated with Gene Ontology (GO). Only interaction pair with interactor.a (ligands) annotated by "extracellular region part" (GO: 0044421), plasma membrane (GO: 0005886), or "plasma membrane part" (GO:0044459), and interactor.b (receptors) annotated by "plasma membrane" (GO:0005886), "plasma membrane region" (GO:0098590) or "plasma membrane part" (GO:0044459) were considered as ligand-receptor interaction pairs. A final 2957 ligand-receptor pairs were generated.

Ligand-receptor activities between cell types were calculated using our previously published single-cell RNA sequencing data (*10*). The relative activity of each ligand-receptor pair was calculated by multiplying the average expression of ligand gene and receptor gene. ChordDiagram was made with package circlize package.

The pseudotime trajectory of monocyte-to-IM development was previously reported (*11*) and analyzed using monocle3 package (1.0.0). Briefly, cells were clustered using the cluster_cells function with UMAP coordinates. The pseudotime trajectories were constructed with the learn_graph and order_cells functions. The starting cells (root cells) were selected to ensure correct trajectory inference. Gene expression across the pseudotime and differential expression was estimated by tradeSeq package (v1.4.0). To infer the contribution of Csf1 and Tgfβ1 during monocyte-to-IM development, target genes regulated by Csf1 and Tgfβ1 were derived from a previously established ligand-target interaction matrix (NicheNetr package). Specifically, the top 100 target genes for each ligand, ranked by interaction score, were selected. A ligand-specific gene signature was then defined by identifying genes that were both among the top 100 targets of the ligand and differentially expressed along the monocyte-to-macrophage trajectory. These ligand-specific signatures were evaluated in the scRNA-seq dataset by using the AddModuleScore function (Seurat). Both signatures were evaluated along pseudotime on the global monocyte-to-IM trajectory. The Tgfβ1 target gene signature was then measured separately for each lineage of CD206^{+} and CD206^{-} IMs.

Supplementary Figures

A

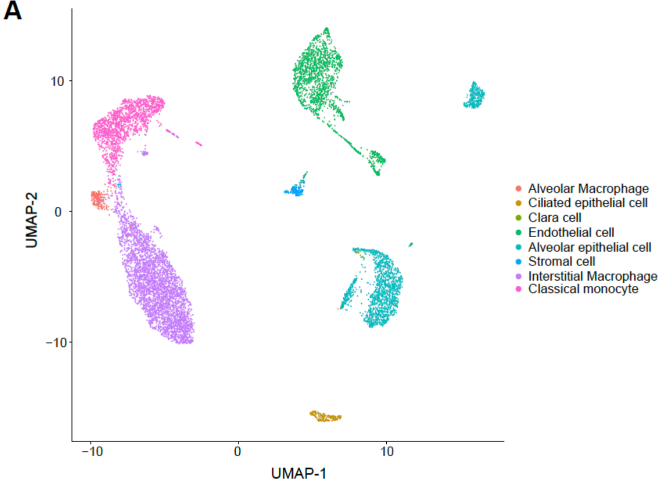

B

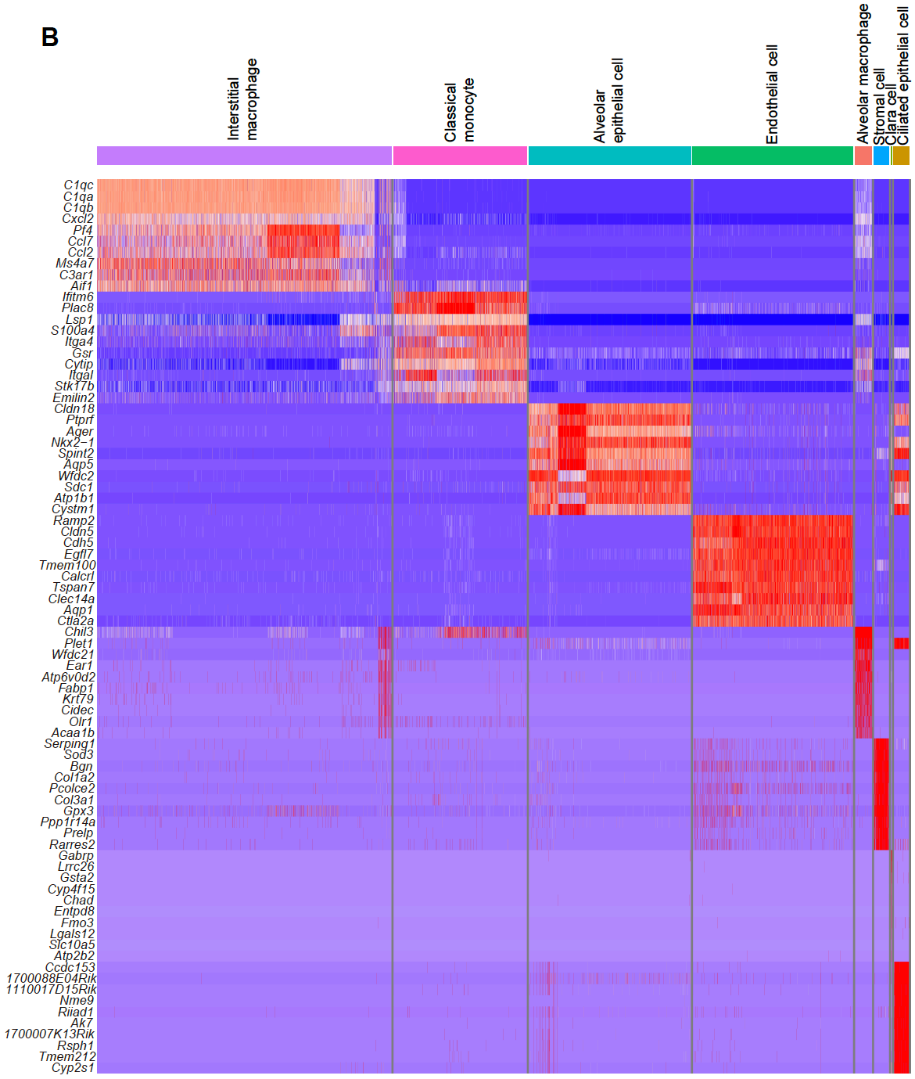

Fig. S1. Transcriptional identity of lung structural and myeloid cells analyzed by NicheNet analyses. (**A**) UMAP plot depicting the transcriptional identity of lung structural cells and myeloid cells from steady-state C57BL/6 WT mice (*10*), as analyzed by scRNA-seq and used for NicheNet analyses shown in Fig. 1, A and B. (**B**) Heatmap depicting the top 10 upregulated genes in each cluster, as in (A).

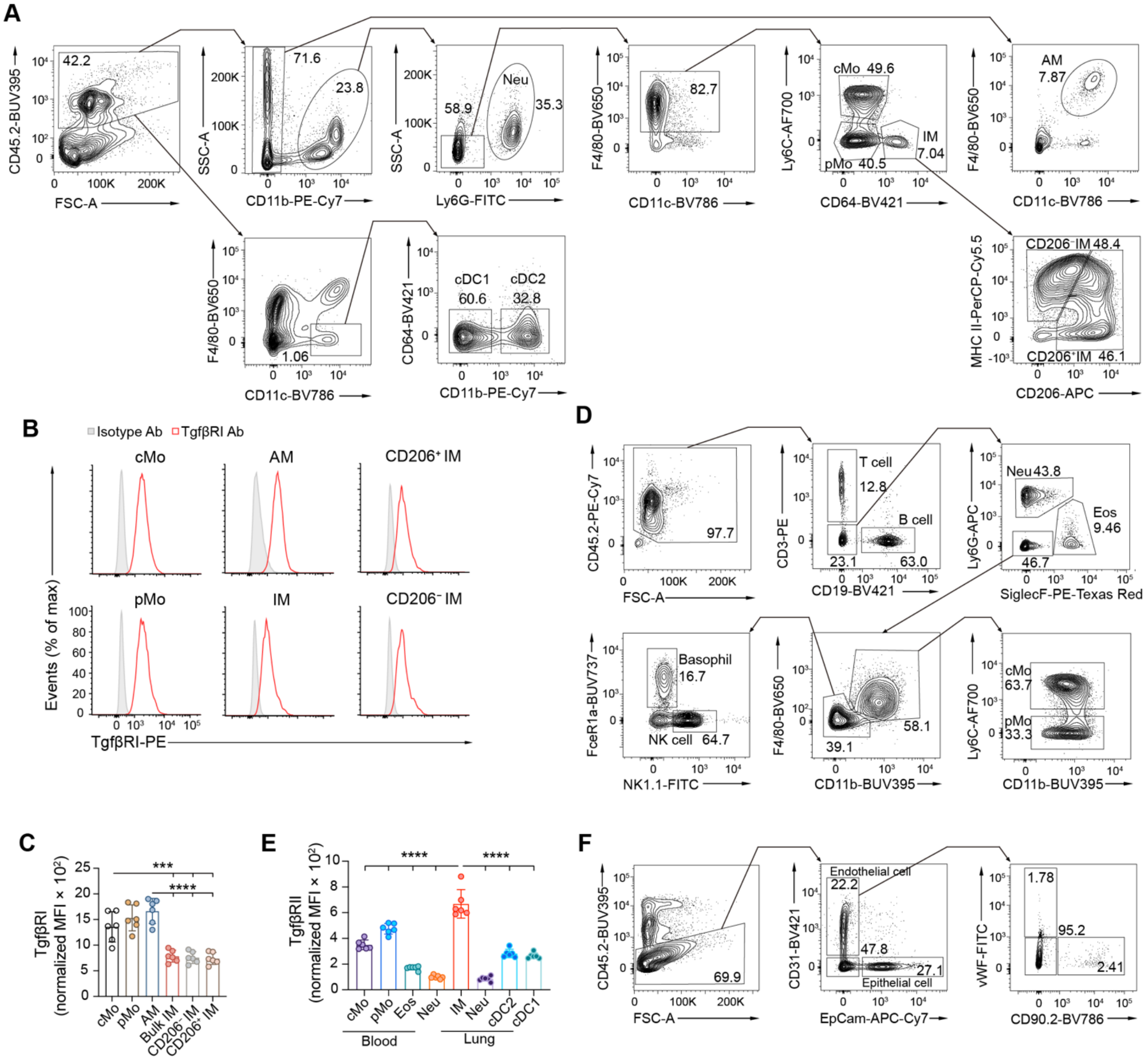

Fig. S2. Flow cytometry gating strategies and expression of Tgfβ receptors by blood and lung myeloid cells. (**A**) Representative flow cytometry gating strategy to delineate lung myeloid cells in lungs of naïve C57BL/6 WT mice. (**B**) Representative histograms and (**C**) bar graph showing normalized MFI of TgfβRI expression in lung cMo, pMo, AMs and IMs, as in (A). (**D**) Representative flow cytometry gating strategy to delineate blood leukocyte populations in naïve C57BL/6 WT mice. (**E**) Bar graph showing normalized MFI of TgfβRII expression in the indicated cell populations from naïve C57BL/6 WT mice. (**F**) Representative flow cytometry gating strategy showing live CD45$^-$EpCam$^+$CD31$^-$ epithelial cells, CD45$^-$EpCam$^-$CD31$^-$ stromal cells and CD45$^-$EpCam$^-$CD31$^+$ endothelial cells, further divided into vWF$^+$CD90.2$^-$ blood vessel, vWF$^-$CD90.2$^+$ lymphatic and vWF$^-$CD90.2$^-$ capillary endothelial cells. (C,E) Data show mean +/- SEM and are representative of 2 independent experiments (n=5-6 mice). *P* values were calculated using (C) a one-way ANOVA with Tukey's post hoc tests or (E) a one-way ANOVA with Dunnett's post hoc tests. ***, *P*<0.001; ****, *P*<0.0001. cDC1, type 1 conventional dendritic cell; cDC2, type 2 conventional dendritic cell; Eos, eosinophil; MFI, mean fluorescence intensity; Neu, neutrophil.

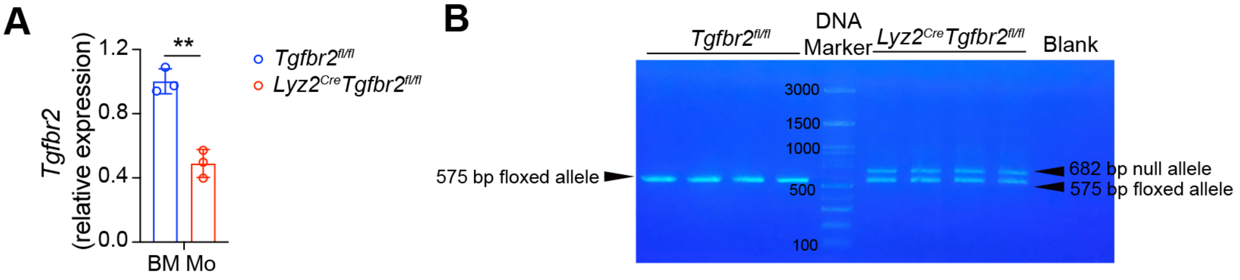

Fig. S3. Efficiency of *Tgfbr2* deletion in BM Mo from *Lyz2*^{Cre} *Tgfbr2*$^{fl/fl}$ mice. (**A**) mRNA expression of *Tgfbr2* in BM Mo from *Lyz2*^{Cre} *Tgfbr2*$^{fl/fl}$ mice and *Tgfbr2*$^{fl/fl}$ littermate controls. (**B**) PCR blot of genomic DNA extracted from BM Mo from *Lyz2*^{Cre} *Tgfbr2*$^{fl/fl}$ mice and *Tgfbr2*$^{fl/fl}$ littermate controls. (A) Data show mean +/- SEM and individual values, each representing one independent experiment. *P* values were calculated using an unpaired two-tailed Student's *t* test. **, $P<0.01$.

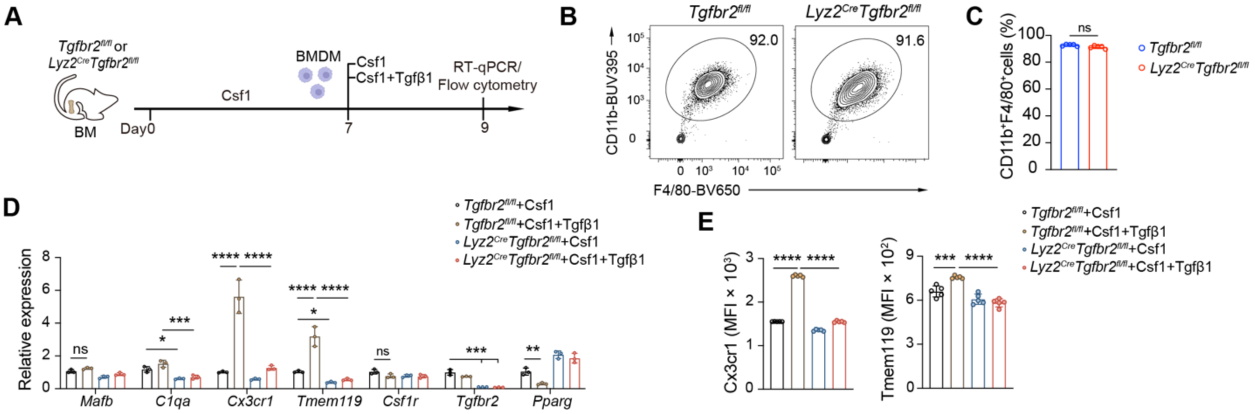

Fig. S4. Stimulation of Csf1-grown BM-derived Macs (BMDMs) with Tgfβ1 triggers a core IM identity. (**A**) Experimental outline for (B-D). BM cells from *Tgfbr2*$^{fl/fl}$ or *Lyz2*^{Cre} *Tgfbr2*$^{fl/fl}$ mice were derived into BMDMs with Csf1 for 7 days, were stimulated with Csf1 or Csf1 + Tgfβ1 for 48 hours and were analyzed by RT-qPCR and flow cytometry. (**B**) Representative CD11b and F4/80 flow cytometry histograms and (**C**) quantification of the % of CD11b^{+}F4/80^{+} Macs in BMDMs, assessed at day 7, as in (A). (**D**) Relative mRNA expression of the indicated genes in BMDMs, as in (A). (**E**) Bar graph showing MFI of Cx3cr1 and Tmem119 expression in BMDMs, as in (A). (C,D,E) Data shown mean +/- SEM and are pooled from (A) 5 different *ex vivo* cultures, (D) 3 independent replicates or (E) 5 mice. *P* values were calculated using (C) an unpaired two-tailed Student's *t* test or (D) a one-way ANOVA with Tukey's post hoc tests or (E) a two-way ANOVA with Dunnett's post hoc tests. *, $P<0.05$; **, $P<0.01$; ***, $P<0.001$; ****, $P<0.0001$. MFI, mean fluorescence intensity; ns, not significant.

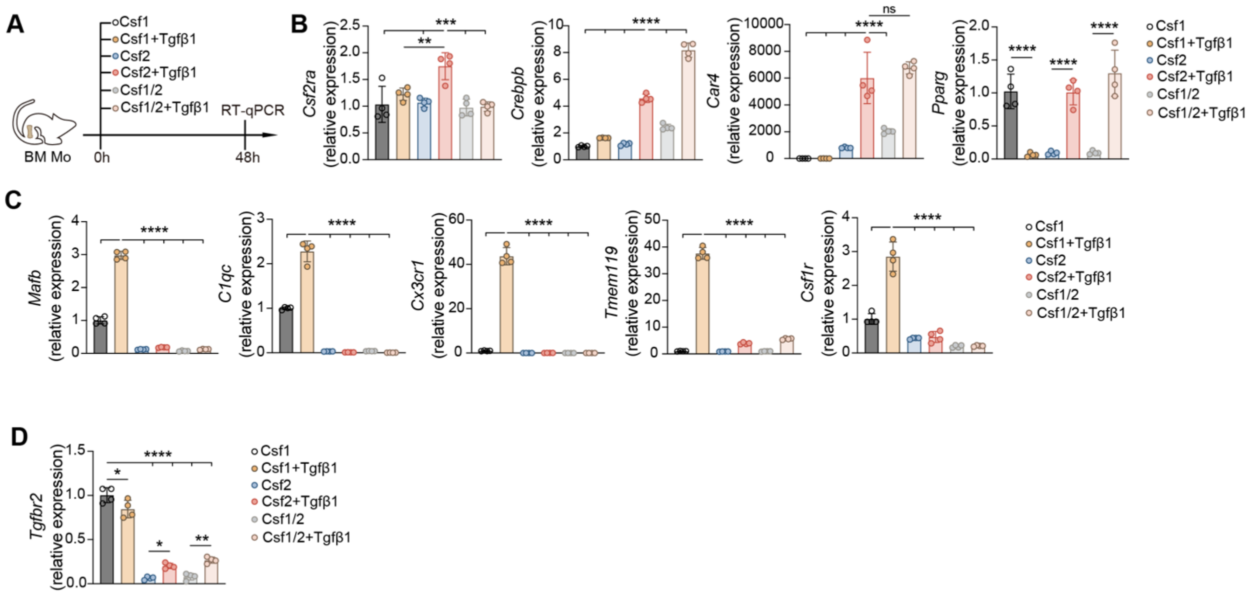

Fig. S5. Csf2 and Tgfβ1 drive AM-associated gene expression while suppressing IM-specific signature in BM Mo. (**A**) Experimental outline for (B-D). BM Mo from C57BL/6 WT mice were stimulated with Csf1, Csf1 + Tgfβ1, Csf2, Csf2 + Tgfβ1, Csf1/Csf2 or Csf1/Csf2 + Tgfβ1 for 48 hours and were analyzed by RT-qPCR. (**B**) Relative mRNA expression of the indicated AM-associated genes in BM Mo, as in (A). (**C**) Relative mRNA expression of the indicated IM-associated genes in BM Mo, as in (A). (**D**) Relative mRNA expression of *Tgfbr2* in BM Mo, as in (A). (B-D) Data show mean +/- SEM and independent replicates are representative from 2 independent culture experiments (n=4 mice). *P* values were calculated using (B, C) a one-way ANOVA with Dunnett's post hoc tests or (D) a one-way ANOVA with Tukey's post hoc tests. *, *P*<0.05; **, *P*<0.01; ***, *P*<0.001; ****, *P*<0.0001. ns, not significant.

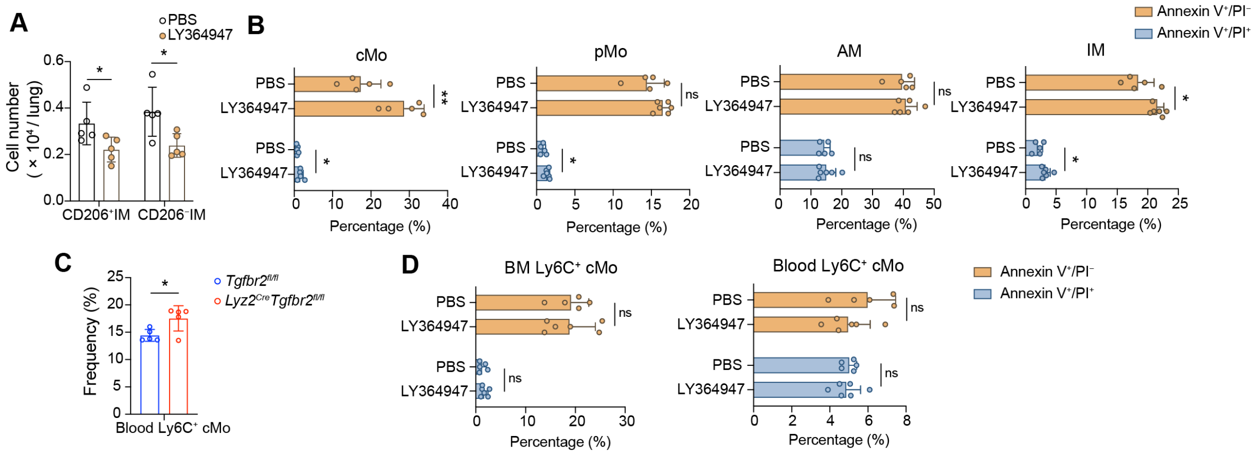

Fig. S6. Numbers of IM subsets and viability of Ly6C$^+$ cMo, Ly6C$^-$ pMo, AMs and IMs in LY363947-treated IM-depleted IM^{DTR} mice at day 7 post-DT. (**A**) Absolute numbers of CD206$^+$ IMs and CD206$^-$ IMs in LY363947-treated and vehicle-treated IM-depleted IM^{DTR} mice at day 7 post-DT. (**B**) Bar graphs showing the percentages of annexin V$^+$/PI$^-$ (early apoptotic) and annexin V$^+$/PI$^+$ (late apoptotic) cells within lung cMo, pMo, AMs and IMs in LY363947-treated and vehicle-treated IM-depleted IM^{DTR} mice at day 7 post-DT. (**C**) Bar graph showing percentages of blood CD45$^+$CD11b$^+$Ly6C$^+$ cMo, as in (B). (**D**) Bar graphs showing the frequency of annexin V$^+$/PI$^-$ (early apoptotic) and annexin V$^+$/PI$^+$ (late apoptotic) within BM and blood cMo, as in (B). (A,B,C,D) Data show mean +/- SEM and independent replicates are representative 2 independent experiments (n=5-6 mice). *P* values were calculated using (A,B,C,D) an unpaired two-tailed Student's *t* test. *, $P<0.05$; **, $P<0.01$ ns, not significant.

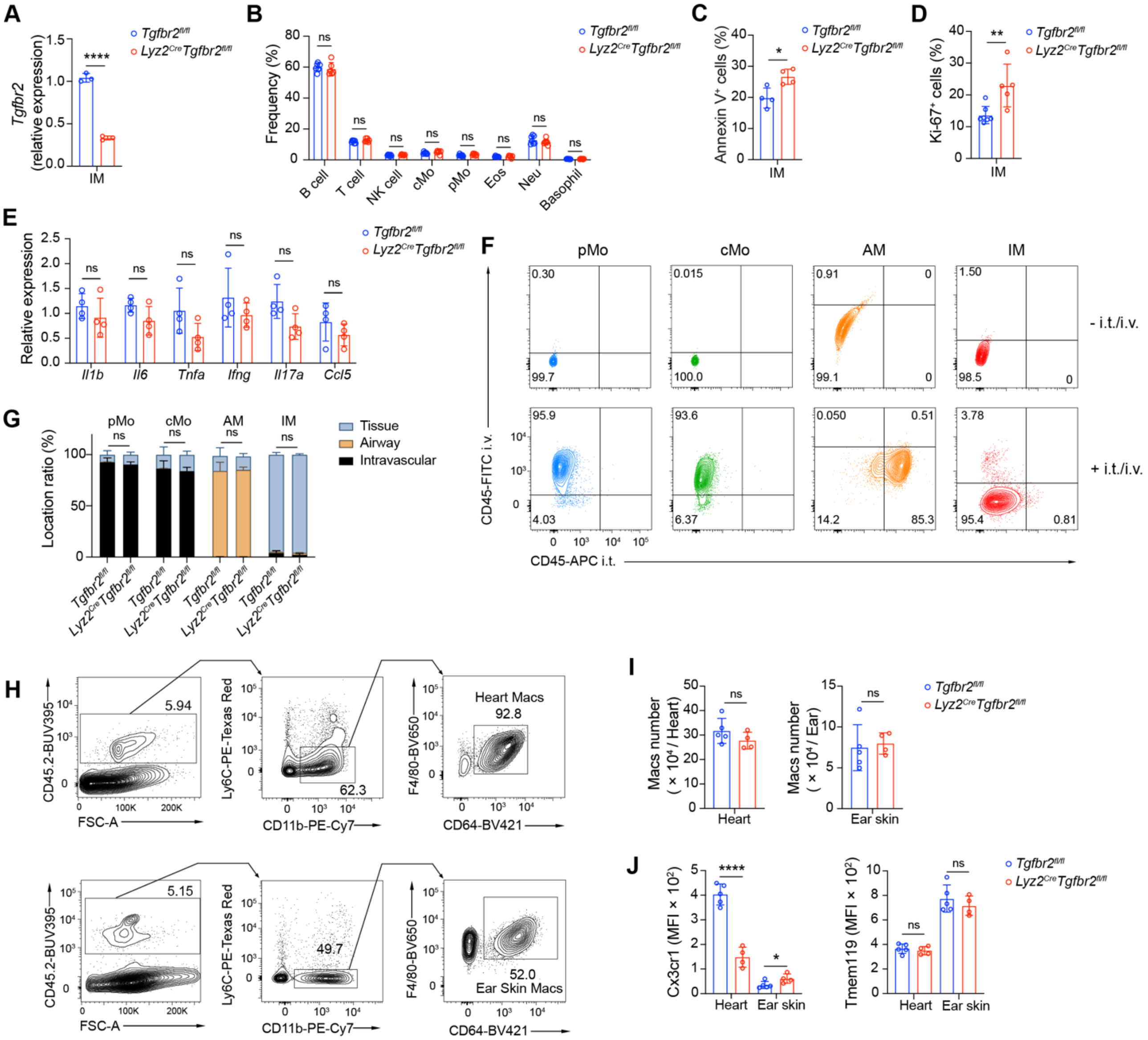
A
Tgfbr2 (relative expression)
1.5
1.0
0.5
0.0
****
IM
Tgfbr2fl/fl
Lyz2CreTgfbr2fl/fl
B
Frequency (%)
80
60
40
20
0
ns
B cell
T cell
NK cell
cMo
pMo
Eos
Neu
Basophil
C
Annexin V+ cells (%)
*
D
Ki-67+ cells (%)
**
E
Relative expression
Il1b
Il6
Tnfa
Ifng
Il17a
Ccl5
F
pMo
cMo
AM
IM
- i.t./i.v.
+ i.t./i.v.
CD45-FITC i.v.
CD45-APC i.t.
0.30
99.7
0.015
100.0
0.91
0
99.1
0
1.50
98.5
0
95.9
4.03
93.6
6.37
0.050
0.51
14.2
85.3
3.78
95.4
0.81
G
Location ratio (%)
Tissue
Airway
Intravascular
H
CD45.2-BUV395
FSC-A
5.94
Ly6C-PE-Texas Red
CD11b-PE-Cy7
62.3
F4/80-BV650
CD64-BV421
Heart Macs
92.8
5.15
49.7
52.0
Ear Skin Macs
I
Macs number (× 10⁴ / Heart)
Macs number (× 10⁴ / Ear)
Heart
Ear skin
J
Cx3cr1 (MFI × 10²)
Tmem119 (MFI × 10²)
****
*
ns

Fig. S7. Analysis of 2-month-old myeloid-restricted *Tgfbr2*-deficient mice. (**A**) mRNA expression of *Tgfbr2* in lung IMs from *Lyz2*^{Cre} *Tgfbr2*$^{fl/fl}$ mice and *Tgfbr2*$^{fl/fl}$ littermate controls, assessed by RT-qPCR. (**B**) Bar graph showing percentages of the indicated blood leukocyte populations in *Lyz2*^{Cre} *Tgfbr2*$^{fl/fl}$ mice and *Tgfbr2*$^{fl/fl}$ littermate controls, assessed by flow cytometry and using the gating strategy shown in fig. S2D. (**C**) Percentage of Annexin V^{+} cells and (**D**) percentage of Ki67^{+} cells in IMs from *Lyz2*^{Cre} *Tgfbr2*$^{fl/fl}$ mice and *Tgfbr2*$^{fl/fl}$ littermate controls. (**E**) mRNA expression of the indicated genes in lungs from *Lyz2*^{Cre} *Tgfbr2*$^{fl/fl}$ mice and *Tgfbr2*$^{fl/fl}$ littermate controls, assessed by RT-qPCR. (**F**) Representative CD45-i.v. and CD45-i.t. plots of lung cMo, pMo, AMs and IMs from *Lyz2*^{Cre} *Tgfbr2*$^{fl/fl}$ mice and *Tgfbr2*$^{fl/fl}$ littermate controls injected with anti-CD45-FITC and anti-CD45-APC Ab i.v. and i.t. before sacrifice, respectively. (**G**) Percentages of tissue (CD45-i.v.$^{-}$/CD45-i.t.$^{-}$), airway (CD45-i.v.$^{-}$/CD45-i.t.$^{+}$) and intravascular (CD45-i.v.$^{+}$/CD45-i.t.$^{-}$) cMo, pMo, AMs and IMs, as in (F). (**H**) Representative flow cytometry gating strategy to delineate heart and ear skin macrophages (Macs) of *Lyz2*^{Cre} *Tgfbr2*$^{fl/fl}$ mice and *Tgfbr2*$^{fl/fl}$ littermate controls. (**I**) Absolute numbers, (**J**) Cx3cr1 and Tmem119 expression levels of heart and ear skin Macs, as in (H). (A,B,C,D,E,G,I,J) Data show mean +/- SEM (A,B,C, E, I, J) are representative of 2 independent experiments (n=4-5 mice) and (D,G) are pooled from 2 independent experiments (n=4-7 mice/group). *P* values were calculated using (A,B,C,D,E,I,J) an unpaired two-tailed Student's *t* test or (G) a two-way ANOVA with Sidak's post-hoc tests. *, *P*<0.05; **, *P*<0.01; ****, *P*<0.0001. ns, not significant.

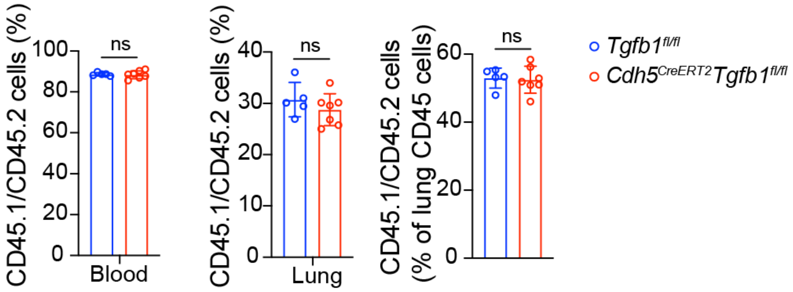

Fig. S8. Donor CD45.1/CD45.2 chimerism in the blood and lung of chimeric *Cdh5*$^{\textit{CreERT2}}$ *Tgfb1*$^{\textit{fl/fl}}$ mice. *Cdh5*$^{\textit{CreERT2}}$ *Tgfb1*$^{\textit{fl/fl}}$ and *Tgfb1*$^{\textit{fl/fl}}$ littermate controls were fed tamoxifen for 28 days, followed by a normal diet. At day 35, mice were lethally irradiated and reconstituted with donor CD45.1/CD45.2 BM cells and the chimerism was evaluated in the blood and in the lung 14 days after. Data shown mean +/- SEM and are pooled from 2 independent experiments (n=7 mice/group). P values were calculated using an unpaired two-tailed Student's t test. ns, not significant.

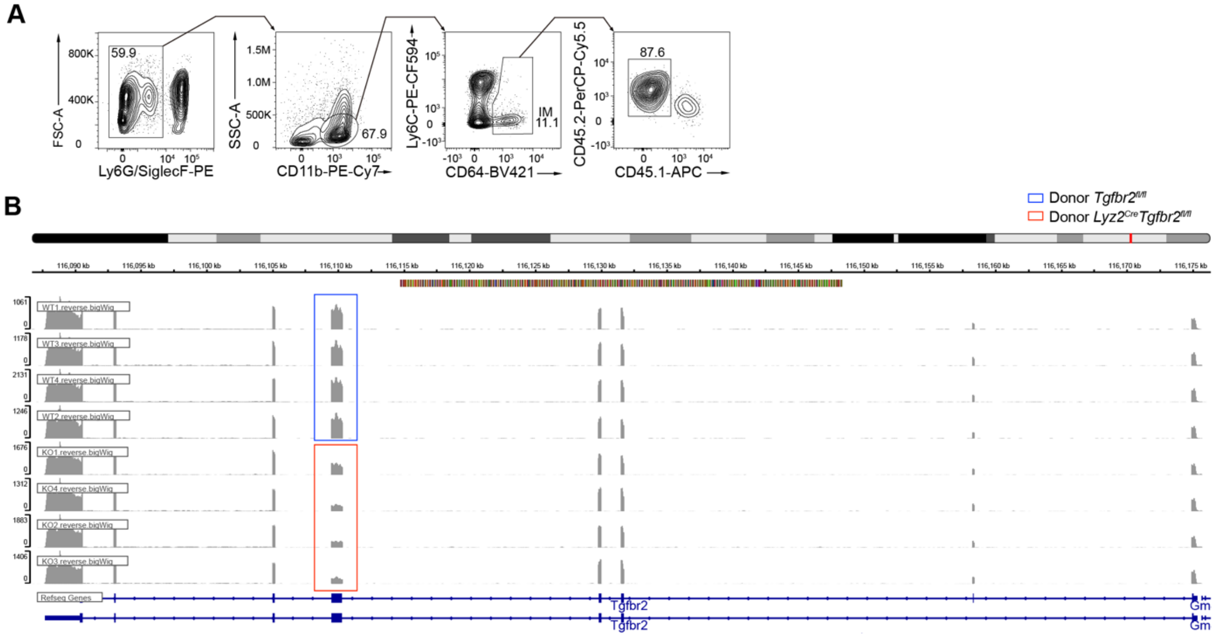

Fig. S9. ***Tgfbr2*** **depletion in donor IMs from donor** ***Tgfbr2*** $^{fl/fl}$ **or donor** ***Lyz2*** ^{Cre} ***Tgfbr2*** $^{fl/fl}$ **chimeric IM** ^{DTR} **mice.** (**A**) Flow cytometry sorting strategy to isolate donor IMs for bulk and scRNA-seq analyses. (**B**) *Tgfbr2* gene sequencing results in IMs from donor *Tgfbr2* $^{fl/fl}$ or donor *Lyz2* ^{Cre} *Tgfbr2* $^{fl/fl}$ chimeric IM ^{DTR} mice.

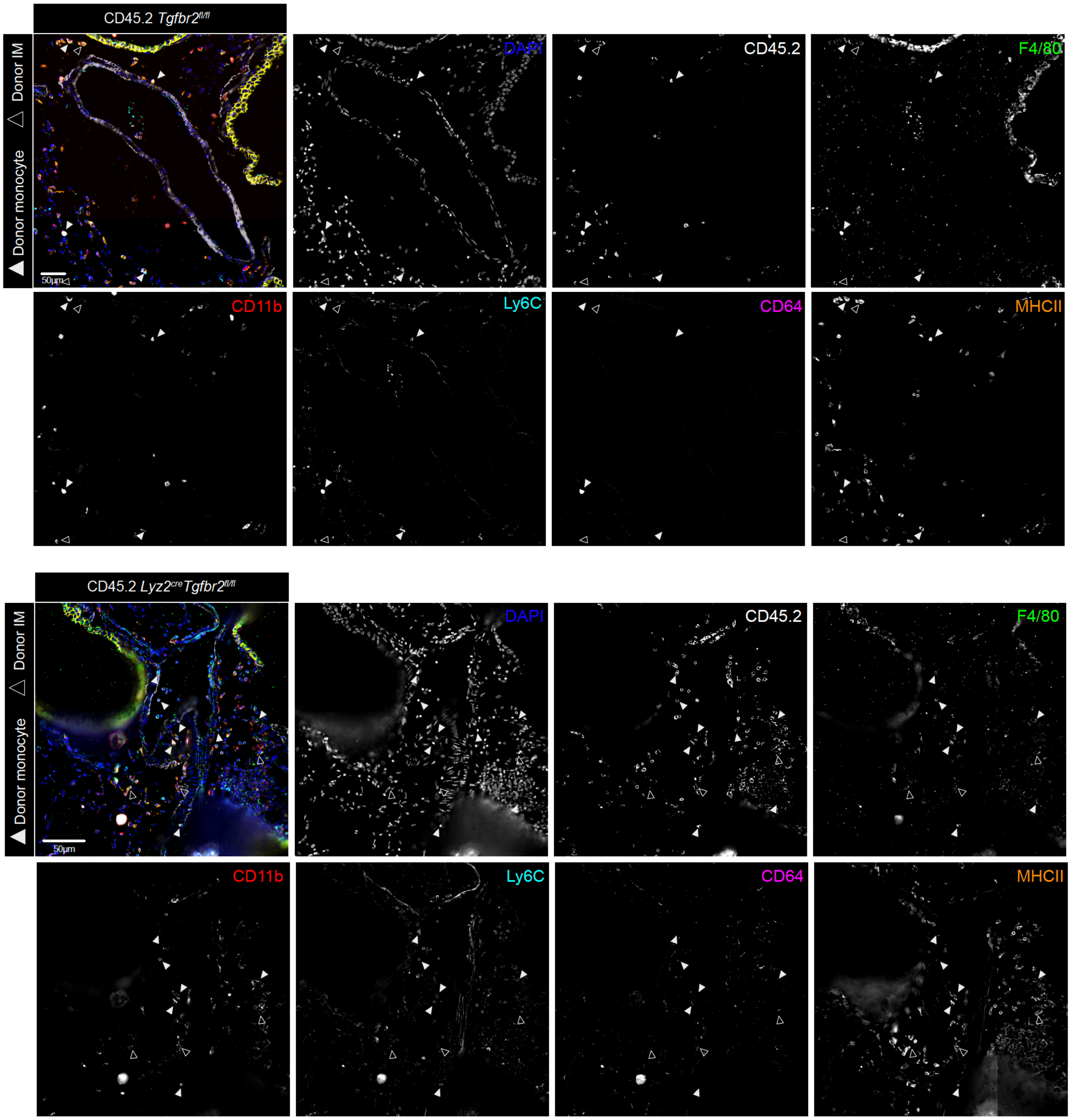

Fig. S10. Identification of donor CD45.1^{-}CD45.2^{+} monocytes and IMs in lungs of donor *Tgfbr2$^{fl/fl}$* and donor *Lyz2^{Cre} Tgfbr2$^{fl/fl}$* chimeric IM^{DTR} mice. Representative pictures showing individual labeling of markers used to define donor CD45.1^{-}CD45.2^{+} monocytes and IMs in lungs of donor *Tgfbr2$^{fl/fl}$* and donor *Lyz2^{Cre} Tgfbr2$^{fl/fl}$* chimeric IM^{DTR} mice. The images are similar as the ones shown in Fig. 7C. Scale bars: 50 µm.

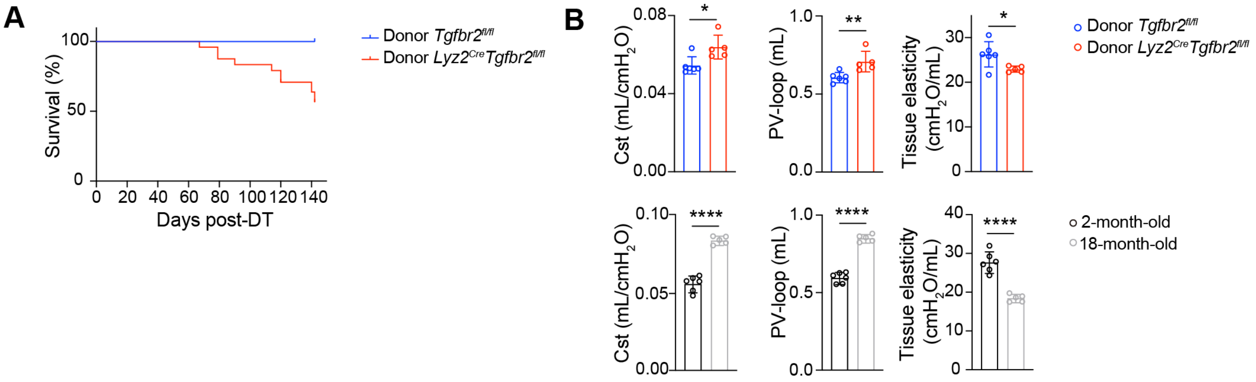

Fig. S11. Survival and lung function of donor *Tgfbr2*$^{fl/fl}$ or donor *Lyz2*^{Cre} *Tgfbr2*$^{fl/fl}$ chimeric IM^{DTR} mice. (**A**) Survival curve of donor *Tgfbr2*$^{fl/fl}$ or donor *Lyz2*^{Cre} *Tgfbr2*$^{fl/fl}$ chimeric IM^{DTR} mice. (**B**) Invasive measurements of quasi-static compliance (Cst), pressure-volume loops (PV-loop) and tissue elasticity in chimeric IM^{DTR} mice 3 months after DT, as in Fig. 6A), and in 2-month-old or 18-month-old C57BL/6 WT mice. (B) Data show mean +/- SEM and are pooled from 2 independent experiments (n= 5-12 mice/group). *P* values were calculated using an unpaired two-tailed Student's *t* test. *, *P*<0.05; **, *P*<0.01; ****, *P*<0.0001.

Table S1. List of reagents, antibodies, commercial assays, primers and softwares used in this study.

Antibodies

Name	Source	Cat. Number	Concentration
Anti-mouse C1qA Monoclonal Antibody (Mouse, clone JL-1), biotin conjugated	Bio-techne	NBP1-51140B	1:50
Anti-mouse CD3 Monoclonal Antibody (Hamster, clone 2H5), PE conjugated	BD Biosciences	553064	1:100
Anti-mouse CD19 Monoclonal Antibody (Rat, clone 6D5), BV421 conjugated	BD Biosciences	115537	1:100
Anti-mouse CD11b Monoclonal Antibody (Rat, clone M1/70), BUV395 conjugated	BD Biosciences	563553	1:100
Anti-mouse CD11b Monoclonal Antibody (Rat, clone M1/70), PE-Cy7 conjugated	BD Biosciences	552850	1:100
Anti-mouse CD11c Monoclonal Antibody (Hamster, clone HL3), BV786 conjugated	BD Biosciences	563735	1:100
Anti-mouse CD16/32 (Mouse BD Fc Block™) Monoclonal Antibody (Rat, clone 2.4G2), unconjugated	BD Biosciences	553142	1:25
Anti-mouse CD31 Monoclonal Antibody (Rat, clone 390), BV421 conjugated	BD Biosciences	563356	1:100
Anti-mouse CD31 Monoclonal Antibody (Rat, clone 390), AF647 conjugated	BioLegend	102416	1:100
Anti-mouse CD45.1 Monoclonal Antibody (Mouse, clone A20), BUV395 conjugated	BD Biosciences	565212	1:100
Anti-mouse CD45.2 Monoclonal Antibody (Mouse, clone 104), BUV395 conjugated	BD Biosciences	564616	1:100
Anti-mouse CD45.2 Monoclonal Antibody (Mouse, clone 104), FITC conjugated	BD Biosciences	561874	1 µg/mouse
Anti-mouse CD45.2 Monoclonal Antibody (Mouse, clone 104), PE-Cy7 conjugated	BD Biosciences	560696	1:100

Anti-mouse CD45.2 Monoclonal Antibody (Mouse, clone 104), PerCP-Cy5.5 conjugated	BD Biosciences	552950	1:100
Anti-mouse CD45.2 Monoclonal Antibody (Mouse, clone 104), APC conjugated	BD Biosciences	558702	1 µg/mouse
Anti-mouse CD64 Monoclonal Antibody (Mouse, clone X54-5/7.1), BV421 conjugated	BioLegend	139309	1:100
Anti-mouse CD68 Recombinant Monoclonal Antibody (Rat, clone FA-11), unconjugated	Bio-rad	MCA1957GA	1:100
Anti-mouse CD90.2 Monoclonal Antibody (Rat, clone 30H12), AF700 conjugated	BioLegend	105320	1:100
Anti-mouse CD90.2 Monoclonal Antibody (Rat, clone 53-21), BV786 conjugated	BD Biosciences	564365	1:100
Anti-mouse CD115 (CSF1R) Monoclonal Antibody (Rat, clone AFS98), PerCP-Cy5.5 conjugated	BioLegend	135526	1:100
Anti-mouse CD170 (SiglecF) Monoclonal Antibody (Rat, clone E50-2440), PE-CF594 conjugated	BD Biosciences	562757	1:100
Anti-mouse CD206 (MMR) Monoclonal Antibody (Rat, clone C068C2), AF488 conjugated	BioLegend	141710	1:100
Anti-mouse CD206 (MMR) Monoclonal Antibody (Rat, clone C068C2), AF647 conjugated	BioLegend	141712	1:100
Anti-mouse CD206 (MMR) Monoclonal Antibody (Rat, clone C068C2), BV785 conjugated	Sony Biotechnology	1308645	1:100
Anti-mouse CD206 (MMR) Monoclonal Antibody (Rat, clone C068C2), PE-Cy7 conjugated	BioLegend	141720	1:100
Anti-mouse CD326 (Epcam) Monoclonal Antibody (Rat, clone G8.8), APC-Cy7 conjugated	BioLegend	118217	1:100

Anti-mouse CD326 (Epcam) Monoclonal Antibody (Rat, clone G8.8), BV510 conjugated	BD Biosciences	747748	1:100
Anti-mouse Cx3cr1 Polyclonal Antibody (Goat), AF488 conjugated	R&D systems	FAB5825G	1:50
Anti-mouse Erg Recombinant Monoclonal Antibody (Rabbit), unconjugated	Abcam	ab92513	1:100
Anti-mouse F4/80 Monoclonal Antibody (Rat, clone BM8), PE conjugated	Sony Biotechnology	1215550	1:100
Anti-mouse F4/80 Monoclonal Antibody (Rat, clone BM8), BV650 conjugated	BioLegend	123149	1:100
Anti-mouse FceR1a Monoclonal Antibody (Hamster, clone MAR-1), BUV737 conjugated	BD Biosciences	751766	1:100
Anti-mouse I-A/I-E (MHC-II) Monoclonal Antibody (Rat, clone M5/114.15.2), AF700 conjugated	ThermoFisher	56-5321-80	1:100
Anti-mouse I-A/I-E (MHC-II) Monoclonal Antibody (Rat, clone M5/114.15.2), PerCP-Cy5.5 conjugated	Sony Biotechnology	1138125	1:100
Anti-mouse Ki-67 Monoclonal Antibody (Mouse), FITC conjugated	BD Biosciences	51-36524X	1:50
Anti-mouse LAP(TGF-β1) Monoclonal Antibody (Mouse, clone HK1.4), PE conjugated	BioLegend	141403	1:50
Anti-mouse Ly6C Monoclonal Antibody (Rat, clone HK1.4), AF700 conjugated	BioLegend	128024	1:100
Anti-mouse Ly6C Monoclonal Antibody (Rat, clone AL-21), PE-CF594 conjugated	BD Biosciences	562728	1:100
Anti-mouse Ly6G Monoclonal Antibody (Rat, clone 1A8), AF488 conjugated	BioLegend	127625	1:100
Anti-mouse Ly6G Monoclonal Antibody (Rat, clone 1A8), APC conjugated	BD Biosciences	560599	1:100
Anti-mouse MafB Recombinant Monoclonal Antibody (Rabbit, clone BLR046F), unconjugated	Bethyl Laboratories Inc.	A700-046	1:50

Anti-mouse NK1.1 Monoclonal Antibody (Mouse, clone PK136), FITC conjugated	BD Biosciences	553164	1:100
Anti-mouse TGF-beta 1 Monoclonal Antibody (Mouse, clone 9016EC), unconjugated	R&D Systems	MAB2402	1:75
Anti-mouse TGF-beta RI/ALK-5 Monoclonal Antibody (Rat, clone 141231), PE conjugated	R&D Systems	FAB5871P	1:50
Anti-mouse TGF-beta RII Polyclonal Antibody (Goat), PE conjugated	R&D Systems	FAB532P	1:50
Anti-mouse Tmem119 Monoclonal Antibody (Mouse, clone V3RT1GOsz), PE conjugated	ThermoFisher	12-6119-82	1:50
Anti-mouse von Willebrand Factor/vWF Monoclonal Antibody (Mouse, clone C-12), FITC conjugated	Santa Cruz Biotechnology	sc-365712 FITC	1:50
Anti-rabbit IgG (H+L) Cross-Adsorbed Secondary Polyclonal Antibody (Donkey), AF568 conjugated	ThermoFisher	A10042	1:500
Anti-rat IgG (H+L) Cross-Adsorbed Secondary Polyclonal Antibody (Donkey), AF488 conjugated	ThermoFisher	A21208	1:500
Anti-rat IgG (H+L) Cross-Adsorbed Secondary Polyclonal Antibody (Goat), AF647 conjugated	BioLegend	405416	1:500
Anti-mouse IgG (H+L) Cross-Adsorbed Secondary Polyclonal Antibody (Donkey), AF647 conjugated	ThermoFisher	A31571	1:500
Anti-mouse IgG1, κ Isotype Control (Mouse), PE conjugated	BD Biosciences	555749	1:100
Anti-mouse IgG1, κ Isotype Control (Mouse), FITC conjugated	BD Biosciences	51-35404X	1:100
Anti-mouse IgG1, κ Isotype Control (Goat), PE conjugated	R&D Systems	IC108P	1:100

Antibodies for CODEX panel

Name	**Source**	**Cat. Number**
Anti-mouse CD64 (Rat, clone X54-5/7.1)	BioLegend	139302
Anti-mouse CD31 (Rat, clone MEC13.3)	BioLegend	102502
Anti-mouse SMA (Mouse, clone 1A4)	BioLegend	904601
Anti-mouse CD90.2 (Rat, clone Thy-1.2)	BioLegend	140302
Anti-mouse F4/80 (Rat, clone BM8)	ThermoFisher	14-4801-95
Anti-mouse Ly6C (Rat, clone HK1.4)	BioLegend	128002
Anti-mouse EpCAM (Rat, clone G8.8)	BioLegend	118202
Anti-mouse CD8a (Rat, clone 53-6.7)	BioLegend	100702
Anti-mouse PDGFRa (Rat, clone APA5)	ThermoFisher	14-1401-82
Anti-mouse CD11c (Rat, clone N418)	BioLegend	117302
Anti-mouse TCRß (Rat, clone H57-597)	BioLegend	109202
Anti-mouse Ly6G (Rat, clone 1A8)	BioLegend	127602
Anti-mouse CD206 (Rat, clone MR5D3)	Bio-rad	MCA2235GA
Anti-mouse CD169 (Rat, clone 3D6.112)	BioLegend	142402
Anti-I-A/I-E (Rat, clone M5/114.15.2)	BioLegend	107602
Anti-mouse NK1.1 (Mouse, clone PK136)	BioLegend	108702
Anti-mouse CD11b (Rat, clone M1/70)	BioLegend	101202
Anti-mouse CD301b (Rat, clone URA1)	BioLegend	146802
Anti-human/mouse/rat TGFβ (Mouse, clone 1D11.16.8)	Novus Biologicals	NBP3-07718
Anti-mouse MerTK (Rat, clone DS5MMER)	ThermoFisher	14-5751-82
Anti-mouse CD4 (Rat, clone RM4-5)	BioLegend	100506
Anti-mouse CD19 (Rat, clone 6D5)	BioLegend	115502
Anti-mouse Xcr1 (Rat, clone ZET)	BioLegend	148202
Anti-mouse CD26 (Rat, clone H194-112)	BioLegend	137802
Anti-mouse SiglecF (Rat, clone 1RNM44N)	ThermoFisher	14-1702-82
Anti-mouse PDGFRβ (Rat, clone APB5)	BioLegend	136002
Anti-mouse CD45.1 (Mouse, clone A20)	BioLegend	110702

Anti-mouse CD45.2 (Rat, clone 104)	BioLegend	109802

Reagents

Name	**Source**	**Cat. Number**
Annexin V, conjugated FITC	BD Bioscience	560931
Annexin V, conjugated APC	ThermoFisher	A35110
Annexin V Binding Buffer, 10X	BD Bioscience	556454
ArC™ Amine Reactive Compensation Bead Kit	ThermoFisher	A10628
Baytrill (enrofloxacine)	Bayer	616300
Bovine Serum Albumin (BSA)	Sigma	A7906
Brilliant Stain Buffer	BD Bioscience	563794
Collagenase A, from Clostridium histolyticum	Sigma	11088793001
cOmplete™ Protease Inhibitor Cocktail	Sigma	11697498001
Diphtheria Toxin (DT), from *Corynebacterium diphtheriae*	List Biological Labs	150
DNase I	Sigma	11284932001
dNTP	ThermoFisher	N8080260
Donkey serum	Sigma	D9663
Dispase II	Merck Millipore	D4693
DPBS	ThermoFisher	14190094
EDTA	Merck Millipore	1084181000
Elastase from porcine pancreas	Merck Millipore	E1250
FastGene 100 bp DNA Marker	NIPPON Genetics	MWD100
Fetal Bovine Serum (FBS)	ThermoFisher	10270098
Glycerol	ThermoFisher	158920025
GoTaq G2 Hot Start Taq Polymerase	Promega	M7401
HBSS with Phenol Red	Lonza	BE10-508F

IsoFlo (Isoflurane)	Zoetis	B506
KAPA Express Extract	Merck	KK7100
LY-364947	Selleckchem	S2805
MEM NEAA	ThemoFisher	11140-035
Methanol	Merck	67-56-1
Nimatek (Ketamine)	Dechra	804132
Nonidet P 40 Substitute	Sigma	74385
O.C.T. Compound	Tissue-Tek	4583
OneComp eBeads	ThermoFisher	01-1111-41
Paraformaldehyde	ThermoFisher	F/1501/PB15
Percoll	GE Healthcare	17089101
Penicillin-Streptomycin	ThemoFisher	15070-063
ProLong Antifade Mountant with DAPI	ThermoFisher	P36966
Rompun (Xylazine)	Bayer	0076901
Sodium pyruvate	ThemoFisher	11360-070
Sucrose	Merck	57-50-1
Streptavidin, PE-CF594 conjugated	BD Biosciences	BD Biosciences
Recombinant Mouse TGF-beta 1 Protein	R&D Systems	7666-MB-005
0.25g/kg Tamoxifen mouse food	SAFE	E8404A01R 00008
Tris(hydroxymethyl)aminomethane	Merck Millipore	108382
TRIzol Reagent	ThermoFisher	10296010
Triton X-100	Merck	648466
Tween-20	ThermoFisher	233360010
Recombinant Murine M-CSF	ThermoFisher	315-02
RPMI 1640 Medium	ThermoFisher	21875-034
2-Mercaptoethanol	ThemoFisher	31350-010

CD11b MicroBeads, human and mouse	Miltenyi Biotec	130-049-601
CD31 MicroBeads, mouse	Miltenyi Biotec	130-097-418
Mouse Elastin ELISA Kit (Colorimetric)	Novusbio	NBP3-06918
IL-10 Mouse Uncoated ELISA Kit	ThermoFisher	88-7105-88
iTaq Universal SYBR Green Supermix	Bio-rad	1725121
LIVE/DEAD™ Fixable Near-IR Dead Cell Stain Kit, for 633 or 635 nm excitation	BD Biosciences	L34976
Foxp3 / Transcription Factor Staining Buffer Set	ThermoFisher	00-5523-00
Monocyte Isolation Kit (BM), mouse	Miltenyi Biotec	130-100-629
Pierce™ BCA Protein Assay Kit	ThermoFisher	23225
Quick-DNA™ Microprep Kit	ZYMO RESEARCH	D3020
TGF beta-1 Human/Mouse Uncoated ELISA Kit	ThermoFisher	88-8350-88
RevertAid H Minus First Strand cDNA Synthesis Kit	ThermoFisher	K1631
RNA Clean & Concentrator™-5	ZYMO RESEARCH	R1013
Sircol Soluble Collagen Assay Kit	Biocolor	S1000
VascuLife® EnGS-Mv Microvascular Endothelial Kit	CellSystems	LL-0004

Reagents for CODEX staining

Name	**Source**	**Cat. Number**
CODEX staining kit	Akoya Biosciences	7000008
CODEX conjugation kit	Akoya Biosciences	7000009
CODEX Buffer	Akoya Biosciences	7000001
Nuclear staining	Akoya Biosciences	7000003
BS3 fixative	ThermoFisher	21580
Acetone	Sigma	650501-1L
Methanol Free Formaldehyde	Sigma	28908

Methanol for HPLC >99.9%	Sigma	34860-1L-R

Barcodes and reporters for CODEX

Name	**Source**	**Cat. Number**
BX005 – RX005	Akoya Biosciences	5450024
BX006 – RX006	Akoya Biosciences	5450027
BX007 – RX007	Akoya Biosciences	5450015
BX010 – RX010	Akoya Biosciences	5450016
BX013 – RX013	Akoya Biosciences	5450017
BX014 – RX014	Akoya Biosciences	5450025
BX015 – RX015	Akoya Biosciences	5350001
BX016 – RX016	Akoya Biosciences	5150001
BX017 – RX017	Akoya Biosciences	5250001
BX019 – RX019	Akoya Biosciences	5450002
BX021 – RX021	Akoya Biosciences	5350002
BX022 – RX022	Akoya Biosciences	5150003
BX023 – RX023	Akoya Biosciences	5250003
BX024 – RX024	Akoya Biosciences	5350003
BX026 – RX026	Akoya Biosciences	5250004
BX027 – RX027	Akoya Biosciences	5350004
BX028 – RX028	Akoya Biosciences	5450005
BX030 – RX030	Akoya Biosciences	5350005
BX031 – RX031	Akoya Biosciences	5150006
BX033 – RX033	Akoya Biosciences	5350006
BX034 – RX034	Akoya Biosciences	5150007
BX037 – RX037	Akoya Biosciences	5150008
BX040 – RX040	Akoya Biosciences	5450009
BX041 – RX041	Akoya Biosciences	5250008
BX042 – RX042	Akoya Biosciences	5350008
BX043 – RX043	Akoya Biosciences	5150010

BX047 – RX047	Akoya Biosciences	5250009
BX049 – RX049	Akoya Biosciences	5450012

Primers

Gene name		5’ → 3’
Actb	F	AATCGTGCGTGACATCAAAG
	R	GGATTCCATACCCAAGAAGG
Csf1r	F	TGGATGCCTGTGAATGGCTCTG
	R	GTGGGTGTCATTCCAAACCTGC
Tmem119	F	ACTACCCATCCTCGTTCCCTGA
	R	TAGCAGCCAGAATGTCAGCCTG
Tgfbr1	F	CATTCACCACCGTGTGCCAAATGA
	R	ACCTGATCCAGACCCTGATGTTGT
Tgfbr2	F	CGACTTGACCTGTTGCCTGT
	R	CGTCTGCTTGAACGACTCCA
Tgfb1	F	TGACGTCACTGGAGTTGTACGG
	R	GGTTCATGTCATGGATGGTGC
C1qc	F	AAGGACGGGCATGATGGACTCC
	R	TTTCCCACGGTGGCCAGGCAT
Mafb	F	AGACAGGCTTTGCGTCCTAA
	R	TGCCAATGTGTGGGTTTCTA
Cx3cr1	F	GTGAGACTGGGTGAGTGACTGG
	R	CGAGGACCACCAACAGATTT
Pparg	F	GTGATGGAAGACCACTCGCATT
	R	CCATGAGGGAGTTAGAAGGTTC
Csf2ra	F	CAGTTTGAGGTCCAGTGGCAGA
	R	CCAGTGCTTCATCCTCGTGTCG
Car4	F	ACTGCCCAGTATCTCCAAACCC
	R	CAGTTTGGTGTGGTTAGTGAGCC
Crebpb	F	CAACCTGGAGACGCAGCACAAG

	R	GCTTGAACAAGTTCCGCAGGGT
Il17a	F	CAGACTACCTCAACCGTTCCAC
	R	TCCAGCTTTCCCTCCGCATTGA
Il1b	F	TGGACCTTCCAGGATGAGGACA
	R	GTTCATCTCGGAGCCTGTAGTG
Ccl5	F	TGCAGAGGACTCTGAGACAGC
	R	GAGTGGTGTCCGAGCCATA
Tnfa	F	CCACGTCGTAGCAAACCAC
	R	TTTGAGATCCATGCCGTTG
Il6	F	TACCACTTCACAAGTCGGAGGC
	R	CTGCAAGTGCATCATCGTTGTTC
Ifng	F	CAGCAACAGCAAGGCGAAAAAGG
	R	TTTCCGCTTCCTGAGGCTGGAT
Mafb$^{fl/fl}$ *genotyping*	F	TCCATCCATCTTGGGAAAAG
	R	TCAGGACTGGGCTGCTAGTT
Tgfbr2$^{fl/fl}$ *genotyping*		TATGGACTGGCTGCTTTTGTATTC
		TGGGGATAGAGGTAGAAAGACATA
		TATTGGGTGTGGTTGTGGACTTTA
Cr3cr1-LSL-DTR genotyping		TCCAATTGTTCACCCTTTCA
		ACCAACAGATTTCCCACCAG
		CTCCAGACTGCCTTGGGAAAA
LyzM^{cre} *genotyping*		CCCAGAAATGCCAGATTACG
		CTTGGGCTGCCAGAATTTCTC
		TTACAGTCGGCCAGGCTGAC
Chd5^{creERT2} *genotyping*		GCCTGCATTACCGGTCGATGCAACGA
		GTGGCAGATGGCGCGGCAACACCATT
		GAGACTCTGGCTACTCATCC
		CCTTCAGCAAGAGCTGGGGAC
Tgfb1$^{fl/fl}$ *genotyping*		TGC ACA GTA CCT CAT GCA CA
		GGG GTG GAG ACA GAC TGG AA

Softwares

Software	**Producer**	**Reference**
Flowjo v10.8.1	BD	https://www.flowjo.com/
Prism 10	GraphPad Software	https://www.graphpad.com/scientific-software/prism/
Adobe Illustrator 2021	Adobe	
R	The R Foundation	https://www.r-project.org/
ImageJ 1.54	National Institutes of Health	http://imagej.org/
Imaris 9.5	Oxford Instruments	https://imaris.oxinst.com/
Qupath 0.5.0		https://qupath.github.io/
CODEX instrument manager	Akoya Biosciences	
CODEX Processor	Akoya Biosciences	
CODEX MAV	Akoya Biosciences	
CytoMAP		(*60*)

Table S2. CODEX phenotypes

Cell type	**Markers**
Monocyte	$CD45.2^+$ $CD45.1^-$ Lin^- $CD11b^+$ $SiglecF^-$ $F4/80^+$ $Ly6C^{+/lo}$ $CD64^{+/lo}$ $MerTK^{lo/-}$
IM	$CD45.2^+$ $CD45.1^-$ Lin^- $CD11b^+$ $SiglecF^-$ $F4/80^+$ $Ly6C^-$ $MerTK^+$ $MHCII^+$
$CD206^-$ IM	$CD45.2^+$ $CD45.1^-$ Lin^- $CD11b^+$ $SiglecF^-$ $F4/80^+$ $Ly6C^-$ $MerTK^+$ $MHCII^+CD206^-$
$CD206^+$ IM	$CD45.2^+$ $CD45.1^-$ Lin^- $CD11b^+$ $SiglecF^-$ $F4/80^+$ $Ly6C^-$ $MerTK^+$ $MHCII^+$ $CD206^+$
AM	$CD45^+$ Lin^- $F4/80^+$ $CD64^+$ $CD11c^+$ $SiglecF^+$
DC1	$CD45^+$ Lin^- $F4/80^-$ $CD26^+$ $MHCII^+$ $CD11c^+$ $Xcr1^+$
DC2	$CD45^+$ Lin^- $F4/80^-$ $CD26^+$ $MHCII^+$ $CD11c^+$ $CD11b^+$
Eosinophil	$CD45^+$ Lin^- $CD64^-$ $CD11c^-$ $SiglecF^+$
Neutrophil	$CD45^+$ Lin^- $F4/80^-$ $Ly6G^+$ $CD11b^+$

B cell	CD45^{+} TCRβ^{-} CD19^{+}
T cell	CD45^{+} CD19^{-} TCRβ^{+}
ILC	CD45^{+} TCRβ^{-} CD19^{-} CD127^{+}
Endothelial cell	CD45^{-} CD31^{+} EpCAM^{-} PDGFRa^{-}
Fibroblast	CD45^{-} CD31^{-} EpCAM^{-} PDGFRa^{+}
Epithelial cell	CD45^{-} CD31^{-} EpCAM^{+} PDGFRa^{-}